

Leyre Hernández López

# Electronic and magnetic properties of 2D metal- organic networks

Director/es

Lobo Checa, Jorge  
Bartolomé Usieto, José Fernando

<http://zaguan.unizar.es/collection/Tesis>





**Universidad**  
Zaragoza

Tesis Doctoral

**ELECTRONIC AND MAGNETIC PROPERTIES OF  
2D METAL-ORGANIC NETWORKS**

Autor

**Leyre Hernández López**

Director/es

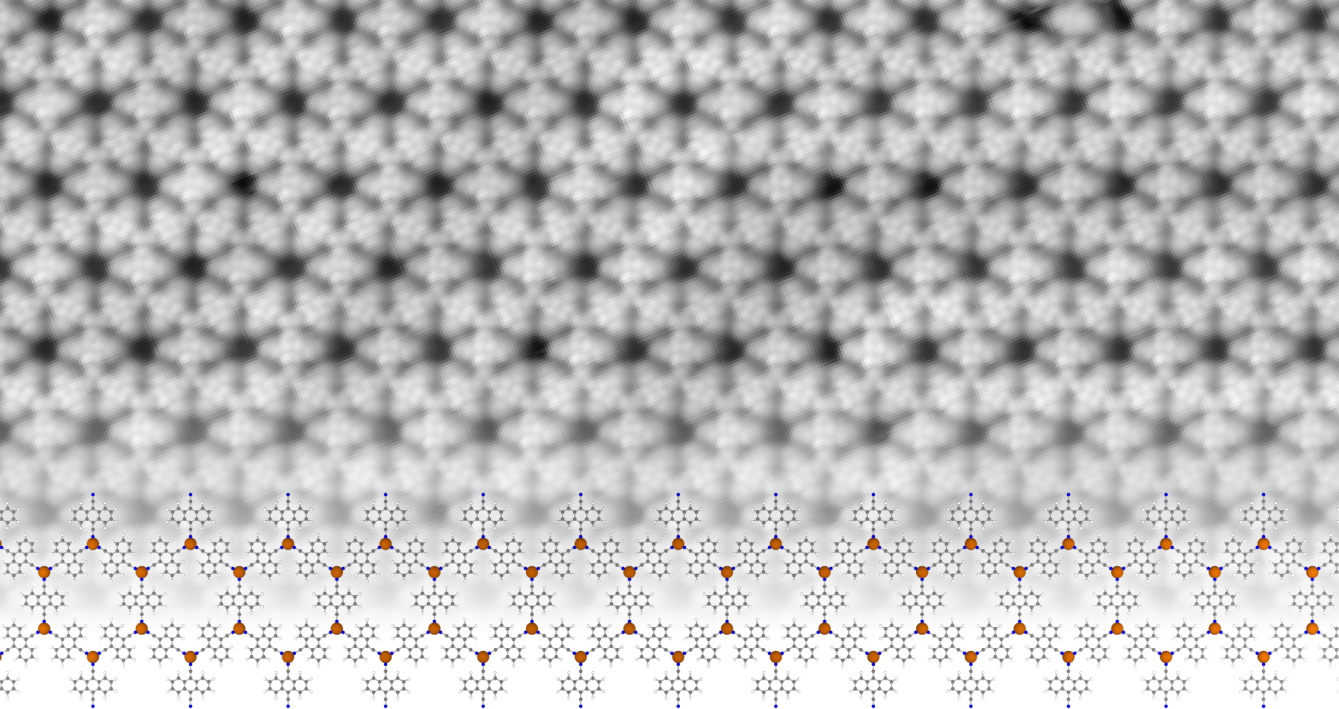
Lobo Checa, Jorge  
Bartolomé Usieto, José Fernando

**UNIVERSIDAD DE ZARAGOZA**  
**Escuela de Doctorado**

2021







Doctoral Thesis

---

# Electronic and magnetic properties of 2D metal-organic networks

---

Leyre Hernández López



---

# Electronic and magnetic properties of 2D metal-organic networks

---

Doctoral Thesis

Leyre Hernández López

Supervisors:

Dr. Jorge Lobo Checa  
Dr. Fernando Bartolomé Usieto

October 2021



**CSIC**  
CONSEJO SUPERIOR DE INVESTIGACIONES CIENTÍFICAS



1542

**Universidad**  
Zaragoza

**INMA**  
INSTITUTO DE NANOCIENCIA  
Y MATERIALES DE ARAGÓN



**LMA**  
LABORATORIO  
DE MICROSCOPIAS  
AVANZADAS



A mis padres,  
Pilar y Ángel



# *Abstract*

The invention of the Scanning Tunneling Microscopy and the development of supramolecular protocols on solid surfaces have promoted the research in the field of two-dimensional systems. Both are key to discover and study organic nanostructures resulting in flexible nanodevices due to their tunable morphologies. Among them, metal-organic assemblies stand out as they are able to form strong but reversible bonds. This intermediate strength intensity allows the growth of almost defect-free long-range ordered structures. Moreover, the choice of their building blocks and the underlying substrate can guide the growth of networks into preferential geometries featuring different functionalities.

Metal-organic networks displaying mixed honeycomb-kagome sublattices have been theoretically predicted to be organic topological insulators. This implies hosting topologically protected edge states, however, such states have never been experimentally observed. Here, we present 8 different networks that consist of mixed honeycomb-kagome sublattices with identical topography by varying their coordination atoms and underlying substrate. A detailed study of their electronic properties is presented in Chapters 3 and 4. We reveal the first experimental demonstration of an electronic band in a two-dimensional metal-organic network that is significantly conditioned by the underlying substrate. The edge states were in all cases absent even in those substrates with minimal interaction with the network. We assign this absence to slight structural distortions that break mirror and inversion symmetries, thereby hindering the OTI realization.

When magnetic atoms are incorporated into the 2D networks, interesting phenomena arise due to the low coordination environment and their collective electronic condition. In Chapter 5, the networks magnetism is studied by means of synchrotron based X-ray techniques. Interestingly, one of them, Fe+DCA/Au(111), is experimentally found to be the first metal-organic 2D ferromagnet with the behavior of an Ising model system.

Finally, the capability of one of these networks as template for the growth of  $3d$  and  $4f$  metals nanostructures is probed in Chapter 6. We find that the periodicity and size of these structures are affected and tuned to a certain degree by a proper choice of the preparation parameters.





# *Acknowledgements*

La razón principal por la cual estos cuatro años van a ser inolvidables son las personas de las que he estado rodeada, que, sin duda, son lo mejor que me llevo.

En primer lugar quiero agradecer a Jorge y Fernando, mis directores de tesis, por brindarme esta oportunidad y por haberme enseñado tantas cosas dentro y fuera de lo académico. Gracias por tener tanta paciencia y por haberme dado ánimos en los momentos duros. Así ha sido todo mucho más fácil y por ello estaré eternamente agradecida.

Gracias a todo el grupo DWARFS, por vuestra calurosa acogida. En especial quiero darle las gracias a Julia, que me acompañó en mis primeros pasos en la ciencia y en la divulgación y a Marisa, por preocuparse tanto siempre por que los más jóvenes estemos bien. A Lola y Cristina, que tantas veces me han facilitado la vida en cuanto a temas burocráticos.

A Carlos, que hace que todo en el laboratorio funcione a la perfección, por perder el tiempo necesario en enseñarme, por todas las conversaciones relacionadas con el laboratorio y con la vida en general y por sus grandes consejos... ¡muchas gracias! Trabajar en otros laboratorios no será lo mismo sin ti. A David Serrate, que me enseñó por primera vez lo que era un STM (algo haría bien) y por ayudarme cuando había cualquier tipo de problema en el laboratorio.

Un pilar muy importante durante estos años han sido mis compañeros, los doctorandos y los que ya son doctores. A todos ellos les agradezco los buenos ratos que hemos pasado dentro y fuera de la Universidad. Tengo que hacer una especial mención a Amelia, mi compañera de laboratorio, por todas las horas compartidas allí, donde hemos sufrido agobios, alegrías, dudas y algún que otro desastre STMero. Por ser la mejor compañera de viajes y congresos y compartir conmigo desayunos eternos en los hoteles. Qué suerte que la vida nos volviese a cruzar. A Rubén, el responsable de la mayor parte de las risas que me he echado en el trabajo; a Barri, por ser el vivo ejemplo de lo que puede cundir la vida; a Pablo, por su inestimable ayuda con cualquier problema tecnológico y por tratar de hacer siempre que estemos todos bien; a Rafa, por hacer desde que llegaste que no haya silencios ni conversaciones serias; a Alba, por su alegría contagiosa y ¡por traernos rosquitos!; a Adán, por ayudarme a mantener el gusanillo por correr; a Pilar, Javi y Mario, por acogernos y cuidarnos tan bien desde el primer día; a Simon, por endulzarnos los cafés y por las carreras compartidas; a Adriana, por los ratos que hemos pasado

dentro pero sobre todo fuera de la facultad, por escucharme tan atentamente ante cualquier problema y por las lecciones de vida aprendidas juntas; a Adrián, por enseñarme que los agobios no llevan a ningún lado; a David, por todos los cafés compartidos desde el principio; a Francho, por prestarme su desinteresada ayuda tantas veces desde que empezamos la carrera; a Daniel, Jorge y Álex, mis compañeros de despacho durante unos meses, por los buenos ratos que allí pasamos; a Iñaki, por amenizarme tanto los beamtimes con sus *hamaiketakoak* y por estar siempre dispuesto a echar una mano.

Durante las primeras semanas en la Facultad de Ciencias, hace ya nueve años, me encontré con María, Marina y Andrea. A ellas tengo que agradecerles los días estudiando y las noches saliendo que pasamos, tantos agobios y tantas alegrías juntas. Sin ellas, el camino hasta aquí habría sido más difícil, pero sobre todo mucho más aburrido.

Fuera de las paredes de la facultad también hay personas que han sido un gran apoyo a las cuales quiero dar las gracias. A mis amigas del instituto les agradezco especialmente esos ratos de desconexión tan reconfortantes, por todos esos vermús, tapiñas y tardebuenas (el mejor plan del año).

Mi familia ha sido un pilar fundamental durante estos años. A mi abuela, a mi hermano, a mis tíos y primos les agradezco tanto apoyo e interés y especialmente a mis padres, por su apoyo incondicional, por enseñarme su manera de ver el mundo y por ser mi ejemplo. Por todo ello, os dedico esta tesis.

Por último, quiero darle las gracias a Pablo. Su confianza ciega en mí, su paciencia y su serenidad han hecho sin duda que estos años hayan sido mucho más fáciles. Pero sobre todo le agradezco su incansable sonrisa y su habilidad para hacerme disfrutar de las cosas buenas, por pequeñas que sean.

# Contents

<b>Abstract</b>	<b>vii</b>
<b>Acknowledgements</b>	<b>ix</b>
<b>Contents</b>	<b>xi</b>
<b>List of Figures</b>	<b>xii</b>
<b>List of Tables</b>	<b>xv</b>
<b>Acronyms</b>	<b>xix</b>
<b>1 Introduction</b>	<b>1</b>
<b>2 Experimental techniques</b>	<b>9</b>
2.1 Ultra-High Vacuum Chambers . . . . .	10
2.2 Sample preparation . . . . .	11
2.3 Low Energy Electron Diffraction . . . . .	13
2.4 Scanning Tunneling Microscopy . . . . .	15
2.4.1 STM working principles . . . . .	15
2.4.2 CO tip functionalization . . . . .	18
2.4.3 Scanning Tunneling Spectroscopy . . . . .	19
2.5 X-ray Absorption Spectroscopy and Magnetic Circular Dichroism	20
2.5.1 Data analysis and the sum rules . . . . .	22
2.6 Angle-Resolved Photoemission Spectroscopy . . . . .	23
2.7 Synchrotron facilities . . . . .	25
<b>3 Searching for organic topological insulators</b>	<b>27</b>
3.1 Results and discussion . . . . .	28
3.1.1 Network formation and morphology . . . . .	28
3.1.2 Electronic characterization by ARPES . . . . .	28

3.1.3	Electronic characterization by STS . . . . .	34
3.1.4	Edge state at the kagome multi-band . . . . .	36
3.1.5	Assessment of possible causes for the edge state absence	36
3.1.6	Emergence of symmetry breaking in the 2D-MOF using functionalized tips . . . . .	38
3.2	Conclusions . . . . .	42
3.3	Supplementary material for Chapter 3 . . . . .	44
<b>4</b>	<b>Role of the coordination atom and substrate in DCA-based networks</b>	<b>49</b>
4.1	Results . . . . .	50
4.1.1	DCA assembly on Ag(111) and Au(111) substrates with- out metal coordination . . . . .	50
4.1.2	MHK lattices on Ag(111) . . . . .	53
4.1.3	MHK lattices on Au(111) . . . . .	59
4.1.4	MHK lattices on topological insulators . . . . .	64
4.2	Discussion . . . . .	64
4.3	Conclusions . . . . .	72
4.4	Supplementary material for Chapter 4 . . . . .	73
<b>5</b>	<b>Magnetic properties of DCA-based 2D-MOFs</b>	<b>79</b>
5.1	Results and discussion . . . . .	80
5.1.1	Ferromagnetism in 2D-MOFs: Fe+DCA/Au(111) . . . . .	81
5.1.2	The role of the substrate: Fe+DCA/Ag(111) . . . . .	89
5.1.3	Coordination atom dependence: Co+DCA networks . . . . .	91
5.2	Conclusions . . . . .	95
5.3	Supplementary material for Chapter 5 . . . . .	96
<b>6</b>	<b>2D-MOFs as templates to the growth of metals</b>	<b>97</b>
6.1	Nanostructuring Sm atom arrays on 2D-MOFs . . . . .	98
6.2	Creating Fe nanoclusters from 2D-MOFs . . . . .	106
6.3	Conclusions . . . . .	113
6.4	Supplementary material for Chapter 6 . . . . .	114
<b>7</b>	<b>Conclusions and Outlook</b>	<b>119</b>
<b>A</b>	<b>Resumen y conclusiones</b>	<b>123</b>

# List of Figures

1.1	Main milestones in the initial stages of STM . . . . .	2
1.2	Structure of 2D metal-organic networks . . . . .	4
1.3	MHK lattices and their band structure . . . . .	6
2.1	Lab setup . . . . .	10
2.2	Substrates and molecules used in this work . . . . .	11
2.3	Molecular evaporator . . . . .	12
2.4	LEED setup and working principles . . . . .	14
2.5	Tunnel effect in 1D . . . . .	15
2.6	Schematic representation of a STM . . . . .	16
2.7	STM working modes . . . . .	17
2.8	CO tip functionalization . . . . .	18
2.9	STS operation scheme with the lock-in technique . . . . .	19
2.10	XMCD technique . . . . .	22
2.11	Sum rules calculation . . . . .	23
2.12	ARPES technique . . . . .	24
2.13	Synchrotron scheme . . . . .	25
3.1	Cu+DCA/Cu(111) network probed by STM and LEED . . . . .	29
3.2	ARPES characterization before and after network formation . . . . .	30
3.3	ARPES measurements as a function of the molecular coverage and of the incident photon energy . . . . .	32
3.4	Electronic structure of Cu+DCA/Cu(111) studied by ARPES . . . . .	33
3.5	Structural and STS characterization of Cu+DCA/Cu(111) net- work . . . . .	35
3.6	dI/dV map at the network island border . . . . .	37
3.7	Constant-height current maps of Cu+DCA/Cu(111) network . . . . .	39
3.8	OTI tight binding theory . . . . .	41
3.9	Direct ARPES signal cuts . . . . .	44
3.10	Second derivative of ARPES signal cuts . . . . .	45

3.11 Direct and second derivative of ARPES signal integrated along two directions . . . . .	45
3.12 ARPES signal in a large range . . . . .	46
3.13 Supplementary plot of dI/dV grids on network island edges . .	47
3.14 Supplementary plot of tight binding calculations . . . . .	48
4.1 Topography and electronic characterization of DCA/Ag(111) and DCA/Au(111) . . . . .	52
4.2 Structural and electronic characterization of Cu+DCA/Ag(111)	54
4.3 Structural and electronic characterization of Fe+DCA/Ag(111)	56
4.4 Structural and electronic characterization of Co+DCA/Ag(111)	58
4.5 Structural and electronic characterization of Cu+DCA/Au(111)	60
4.6 Structural and electronic characterization of Fe+DCA/Au(111)	62
4.7 Structural and electronic characterization of Co+DCA/Au(111)	63
4.8 Structural and electronic characterization of Co+DCA/Bi <sub>2</sub> Te <sub>3</sub> .	65
4.9 Collection of the STS spectra presented in the MHK lattices . .	67
4.10 Evolution of the pore state at the MHK lattices . . . . .	69
4.11 Network conjugated multi-band state at the MHK lattices . . .	70
4.12 DCA compact assemblies on Au(111) and Ag(111) formed by hydrogen bonds . . . . .	73
4.13 Hydrogen bonds in Cu+DCA/Au(111) networks . . . . .	73
4.14 LEED characterization of MHK networks on Ag(111) . . . . .	74
4.15 LEED characterization of MHK networks on Au(111) . . . . .	75
4.16 Multi-band state ubiquity . . . . .	76
5.1 XAS and XMCD characterization of Fe in Fe+DCA/Au(111) and Fe/Au(111) . . . . .	82
5.2 Orbital and spin effective moments of Fe+DCA/Au(111) and Fe/Au(111) . . . . .	84
5.3 Fe+DCA/Au(111) hysteresis . . . . .	85
5.4 T <sub>C</sub> calculation of Fe+DCA/Au(111) . . . . .	88
5.5 XAS and XMCD characterization of Fe in Fe+DCA/Ag(111) .	90
5.6 Orbital and spin effective moments of Fe in Fe+DCA/Ag(111) .	90
5.7 XAS and XMCD characterization of Co in Co+DCA/Au(111) .	92
5.8 XAS and XMCD characterization of Co in Co+DCA/Ag(111) .	93
5.9 Orbital and spin effective moments of Co in Co+DCA and Co/Ag(111)	94
5.10 Fe XMCD obtained by multiplet calculations . . . . .	96
6.1 Sm deposited on Cu+DCA/Cu(111) . . . . .	98
6.2 Sm hexagonal superlattice structure and topography . . . . .	100

6.3	Sm hexagonal superlattice electronic properties . . . . .	102
6.4	Compact and porous phases of DCA networks . . . . .	103
6.5	Sm superlattices on Cu+DCA networks . . . . .	104
6.6	XAS at the $M_{4,5}$ edges of Sm at superlattices . . . . .	105
6.7	Fe nanodots formed on Cu+DCA networks . . . . .	107
6.8	Fe nanodots size analysis . . . . .	108
6.9	Fe nanodots magnetic properties . . . . .	111
6.10	Sm superlattices acquired <i>in-situ</i> before XAS experiments . . .	114
6.11	Simulated Sm XAS obtained by multiplet calculations . . . . .	115
6.12	Low coverage Fe nanodots . . . . .	115
6.13	Fe nanodots size distribution . . . . .	116
6.14	Fit of the magnetic moments obtained from application of the sum rules to the experimental XMCD data: orbital magnetic moments (orange) and effective spin (blue). The lines are fits to Eqs. 5.1 and 5.2. . . . .	117





# List of Tables

1.1	Samples studied along this thesis . . . . .	8
4.1	Summary of the electronic states of all systems . . . . .	77
5.1	Orbital and spin magnetic moments of Fe+DCA/Au(111) . . . .	84
5.2	Orbital and spin magnetic moments of Fe in Fe+DCA/Ag(111)	90
5.3	Orbital and spin magnetic moments of Co . . . . .	94
6.1	Average area of Fe nanodots . . . . .	109
6.2	Magnetic orbital and effective spin moments of Fe nanodots . .	110
6.3	Magnetic moments of Fe/DCA and Fe/Cu . . . . .	118



# Acronyms

<b>1D</b>	One-dimensional
<b>2D</b>	Two-dimensional
<b>3D</b>	Three-dimensional
<b>AFM</b>	Atomic Force Microscopy
<b>ARPES</b>	Angle-Resolved Photoemission Spectroscopy
<b>DCA</b>	9,10-dicyanoanthracene
<b>DFT</b>	Density Functional Theory
<b>HOMO</b>	Highest occupied molecular orbital
<b>LDOS</b>	Local density of states
<b>LEED</b>	Low Energy Electron Diffraction
<b>LT</b>	Low temperature
<b>LUMO</b>	Lowest unoccupied molecular orbital
<b>MFM</b>	Magnetic Force Microscopy
<b>MHK</b>	Mixed Honeycomb Kagome
<b>ML</b>	Monolayer
<b>MOF</b>	Metal-Organic Framework
<b>OTI</b>	Organic Topological Insulator
<b>QL</b>	Quintuple layer
<b>QMB</b>	Quartz micro-balance
<b>RT</b>	Room temperature
<b>SOC</b>	Spin-orbit coupling
<b>SS</b>	Surface states
<b>STM</b>	Scanning Tunneling Microscopy/Microscope
<b>STS</b>	Scanning Tunneling Spectroscopy
<b>TEY</b>	Total electron yield
<b>UHV</b>	Ultra high vacuum
<b>XAS</b>	X-ray Absorption Spectroscopy
<b>XMCD</b>	X-ray Magnetic Circular Dichroism



# Chapter 1

## Introduction

The human interest in using materials to fabricate new tools dates back to our ancestors. Indeed, Prehistory periods bear the names of the materials as the society of the time learnt to work and manage them. In the Stone Age ( $\sim 2.5$  millions of years ago), cutting tools or weapons were fabricated with stone for the first time. Later on, in the Metal Age, some of the properties of these instruments were improved by its fabrication with copper, bronze or iron. In the recent decades, the necessity of developing new materials with tailored functionalities or the continuous aim of device miniaturization has promoted the research of matter in the nanoscale. Nanoscience and Nanotechnology field comprises the growth, manipulation, observation and analysis of materials with at least one of their dimensions in the range of  $100-0.1$  nm. Such challenge became possible by the construction and development of specific instrumentation that allows manipulating and observing matter in the nanoscale. A big step through this objective occurred with the invention of the Scanning Tunneling Microscopy (STM).

The Scanning Tunneling Microscopy was realized in 1981 in IBM Zürich by Gerd Binnig and Heinrich Rohrer, which made them winners of the Nobel Prize [1, 2]. The development of this sophisticated tool allowed the visualization and analysis of surface structures down to the atomic level. In 1983, Binnig *et al.* resolved the structure of Si(111)  $7 \times 7$  reconstruction, showing its capability to image metallic surfaces with atomic resolution [3] (Fig. 1.1a). For the first time, an organic single molecule, copper phthalocyanine, was imaged with a STM by Gimzewski *et al.* in 1987 [4] (Fig. 1.1b). Two years later, higher resolution images of those molecules that revealed intramolecular details were obtained [5], opening a wide range of possibilities in the field

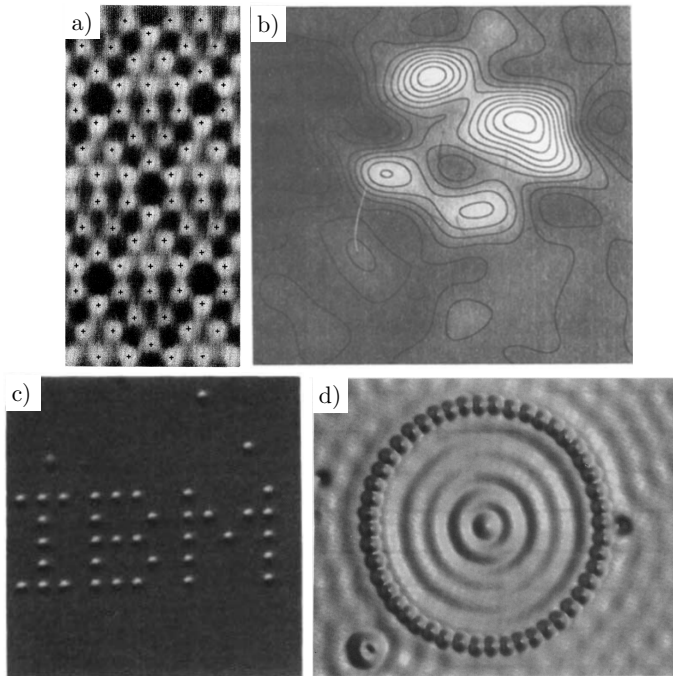


Figure 1.1: Main milestones in the initial stages of STM. a) Determination of the Si(111)  $7 \times 7$  structure [3]. b) First copper phthalocyanine imaged with a STM [4]. c) First evidence of atomic manipulation: Xe atoms precisely positioned on a Ni substrate forming IBM initials [6]. d) Quantum corral formed with 48 Fe atoms on a Cu(111) substrate. The electronic standing wave patterns due to the confinement can be observed [7].

of supramolecular chemistry. Far from being only a powerful imaging instrument, STM has been used to manipulate single atoms on metallic surfaces. In 1990, Eigler *et al.* precisely positioned single Xe atoms on a Ni surface at low temperature (LT) [6] (Fig. 1.1c). It was three years later that Crommie *et al.* constructed a quantum corral formed by 48 Fe atoms on a Cu(111) surface and imaged the confinement of the surface electrons into this corral [7] (Fig. 1.1d). Furthermore, in the years following the STM invention, several STM-related methods were developed, such as the Atomic Force Microscopy (AFM) [8], that allowed studying insulating samples (for example viruses), or Magnetic Force Microscopy (MFM) [9].

In addition to these instruments, methods for the growth of extended nanostructures were developed in order to ease its transition to industrial technological devices. These methods can be classified in two different approaches: top-down or bottom-up. Top-down fabrication is a subtraction method that in-

---

cludes lithography, printing or stamping. To reach precision in the nanometer scale, high energy electron-beams or X-rays are required, which raises the costs of these techniques and the time required to obtain extended structured areas. Instead, bottom-up fabrication methods start from molecules or atoms that interact to each other and self-assemble into larger structures [10]. In surface science, those are typically deposited on a flat metallic surface where thermal diffusion is activated. The resulting structures can be classified depending on the strength of the interactions taking place between building blocks.

In covalent assemblies, molecules form stable and irreversible bonds that do not allow error correction [11]. In spite of this, on-surface synthesis is nowadays widely used for the synthesis and characterization of covalent organic frameworks [12], graphene nanoribbons [13] and related nanostructures [14]. At the other extreme there are non-covalent, purely molecular assemblies. These are usually formed by electrostatic interactions (hydrogen bonds or similar) between organic molecules. The weakness of these bonds allows error correction, which at times results in the formation of well-ordered structures [15–17]. Finally, metal-organic interactions are of intermediate strength and are produced typically between metallic atoms and functional groups of organic molecules. They form strong but reversible bonds, which can result in extended, well-ordered structures. These networks are particularly interesting since the presence of metallic atoms can add some functionalities to the nanostructure due to their physical properties, such as high spin-orbit coupling (SOC) or magnetic moment, among others.

The self-assembly of organic molecules and coordination atoms upon subsequent or co-evaporation on a surface can result in the growth of two-dimensional metal-organic frameworks (2D-MOFs). The finite temperature in the substrate provides kinetic energy to the molecules and coordination atoms, allowing for error correction in the arrays. In some particular cases this allows the growth of almost defect-free, long-range ordered structures [18–20]. The molecules used for this purpose are mostly planar and contain backbones with aromatic rings, which guarantees their adsorption on the surface in a flat configuration, remaining confined in 2D (see Fig. 1.2a). In this way, their functional groups undergo lateral interactions with other molecules or coordination atoms. Coordination atoms are metal elements that usually change their oxidation state due to charge transfer with the surface and molecules, which promotes the bond with the molecular functional groups. The coordination motifs are conditioned by the type of coordination metal:  $3d$  metals usually display 2-, 3- or 4-fold bonds [21–23] while  $4f$  usually display a higher coordination number [24–26]. Moreover, the symmetry and electronic properties of the underlying

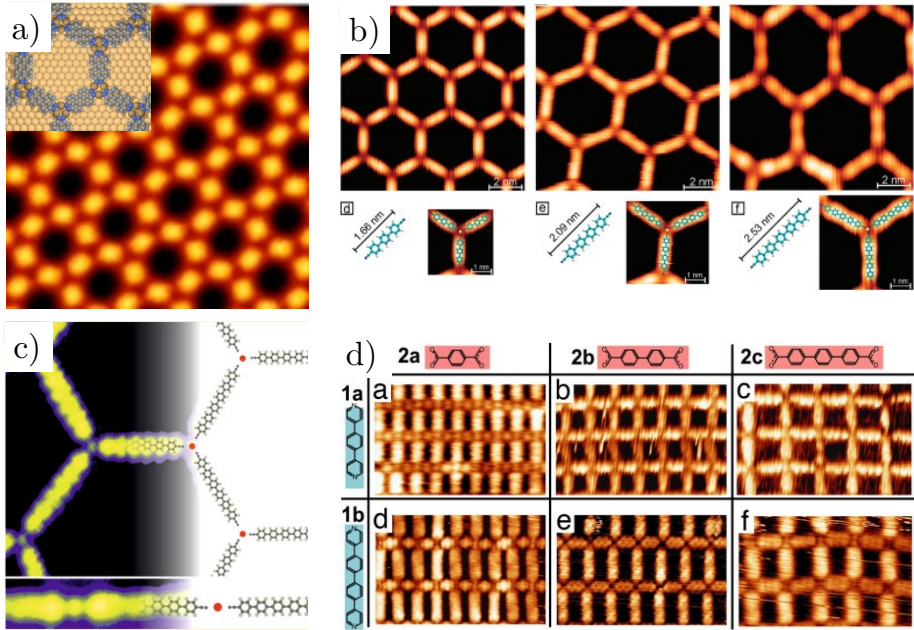


Figure 1.2: Structures of self-assembled 2D metal-organic networks formed on noble metal surfaces. a) Porous honeycomb network with its schematic model. Figure adapted from Ref. [34]. b) Honeycomb lattices with tunable cavity size through molecular length selection [32]. c) One- or two-dimensional metal-organic assemblies guided by their relative stoichiometry [30]. d) Rectangular lattices with tunable cavity size [33].

substrate can guide the growth of 2D-MOFs [27–29].

The mixing of these constituents opens a range of possibilities in the generation of 2D-MOFs with different architectures, potentially interesting for their functionalities (see Fig. 1.2). For example, we can modify the building blocks ratio (atoms vs. molecules) deposited on the surface with the purpose of growing tailored structures with different coordination and forming, for example 2D or 1D arrays [30, 31] (see Fig. 1.2c). Likewise, the periodicity of a structure can also be modified by the deposition of molecules with larger or shorter backbones, generating nanocavities with tunable cavity size [32, 33] (see Fig. 1.2b, d).

These geometrical differences influence the fundamental electronic or magnetic properties of the metal-organic networks. Particularly, the magnetic properties of 2D-MOFs containing magnetic atoms have provoked interest due to the possibility of easily forming extended ordered arrays of unclustered sin-



---

gle atoms. Moreover, their particular ligand environment and decoupling from the substrate can promote enhanced orbital magnetic moments and higher anisotropies. The presence of magnetic moments in a 2D-MOF with Fe as coordination atom was first predicted by Density Functional Theory (DFT) by Seitsonen *et. al.* [35]. Later on, Gambardella *et. al.* detected by X-ray Absorption Spectroscopy (XAS) and X-ray Magnetic Circular Dichroism (XMCD) measurements the presence of such magnetic moments in Fe atoms embedded in a 2D-MOF for the first time [36]. Since then, a wide variety of magnetic phenomena has been reported. The magnetic properties of 2D-MOFs can be tuned by modifying the coordination atom, the underlying substrate or molecular ligands and can induce changes in the magnetic anisotropy [37] but mainly in the type and intensity of magnetic coupling [38–41].

Metal-organic networks have also been employed as templates for the growth of more complex structures. Particularly, porous networks are potentially interesting to host molecules on their pores. This occurs whenever the pore guests bind weakly to the network, but stronger to the exposed substrate in the nanocavity. Molecules such as C<sub>60</sub> [42], sexiphenyl-dicarbonitrile [43] or Co-(1,3,5-tris(pyridyl)benzene) [44] have been confined in the nanocavities of 2D-MOFs. Furthermore, 2D-MOFs have also been used as template to the growth of nanostructured metals. Small quantities of atoms can be accommodated on or below network components (molecules or coordination atoms) [45, 46], but also within pores [47, 48].

One of the most studied aspects of 2D-MOFs, both experimentally and theoretically, are their electronic properties, that are modulated through different structural modifications. Frontier molecular orbitals, highest occupied (HOMO) and lowest unoccupied molecular orbitals (LUMO), undergo electronic changes upon their bond with metallic coordination atoms [30, 49–51]. Wang *et al.* reported an accumulative downshift of unoccupied molecular states in 1,3,5-tris(pyridyl)benzene upon an increasing number of coordination bonds with Cu adatoms [52]. Moreover, the molecule-substrate interactions can also strongly modify the network electronic structure [34, 52].

In the last years, the topological properties of 2D-MOFs are being studied because of their fundamental interest [53–57]. Topological insulators constitute a recently discovered class of materials with potential applications in relevant fields of condensed matter and material science, such as quantum computation and optoelectronics [58–64]. They differ from regular insulators in their conducting edge or surface states (SS) located within bulk band gaps. Their non-trivial band topology generates such spin-textured low dimensional states.

The topological protection of such states stems from the conservation of the system's time reversal symmetry that preserves them from defects or structural perturbations. The non-trivial topology of these edge/surface states originates in the SOC that exists in these materials. These states connect two energy separated “bulk” bands thereby providing spin polarized currents with selective directional transport.

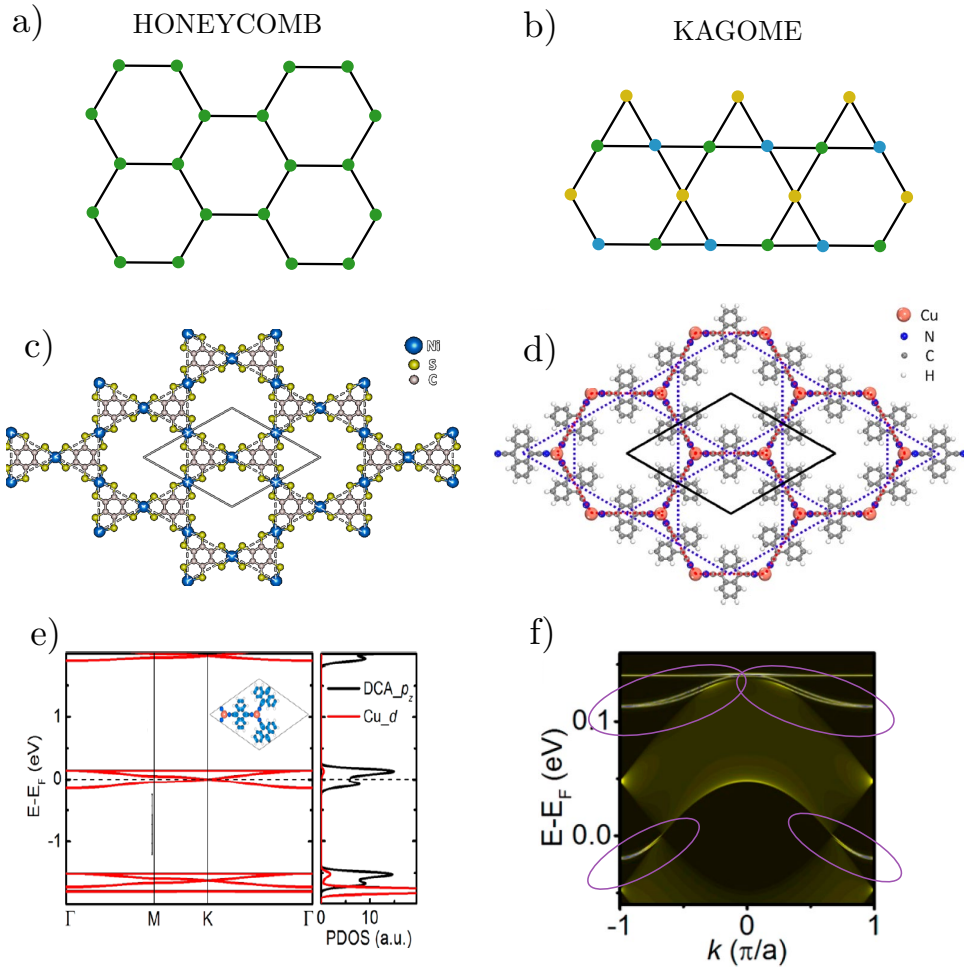


Figure 1.3: Examples of mixed honeycomb-kagome lattices theoretically proposed as OTIs. Schematic a) honeycomb and b) kagome lattices. In c) the coordination atoms form a kagome sublattice and the organic molecules, a honeycomb sublattice, while in d) it is the other way round. Adapted from references: c) [53], d) [55]. e) Theoretical band structure calculated by DFT for the free-standing network presented in d). The Dirac point coincides with the Fermi level resulting in an intrinsic OTI. f) Edge states (marked with purple) within the SOC gaps. Adapted from Ref. [55].

---

Inspired by such compelling quantum properties and physical effects, the 2D organic-based material counterparts to topological insulators are being keenly sought. As a result, several 2D-MOFs have been theoretically proposed and coined as organic topological insulators (OTIs) (see Fig. 1.3) [53–57]. These theoretical constructions are periodic, free standing 2D-MOFs, displaying a combination of kagome and honeycomb structures (see Fig. 1.3a, b). These arrays can be generally named as mixed honeycomb-kagome (MHK) lattices even when they do not present protected topological properties. The metal centers should be responsible for providing the necessary SOC to the system to generate the topologically non-trivial edge states. Their electronic band structure is characterized by a multi-band manifold made up of two dispersive bands meeting at a (gapped) Dirac point and a flat band (see Fig. 1.3e). A different dispersion (with its own energy-momentum dependence) is expected for the edge states that connects these gapped “bulk” states within the multi-bands (see Fig. 1.3f).

Several examples of MHK lattices have been experimentally grown on different substrates [65–69] and their electronic properties studied locally by scanning tunneling spectroscopy (STS). Similar to 2D inorganic topological insulators, their protected states should appear as one-dimensional (1D) conducting edge states visible at the border of the 2D domains [70, 71]. Despite employing different strategies, such as the use of decoupling layers [65] or coordination atoms with significant SOC [66], the edge states are to date elusive and await experimental validation in all proposed OTIs. This absence has been assigned to substrate induced Rashba effect closing the gap [67], but such an explanation drops its generality for networks formed atop decoupling layers [65].

This thesis focuses on the growth and characterization of MHK networks using 9,10-dicyanoanthracene (DCA) as the only molecular precursor. Its topological, electronic and magnetic properties are explored in depth as well as its capability to be used as template for the growth of nanostructured metals. After this Introduction, Chapter 2 presents the main experimental techniques used along this work. Chapter 3 reports the study by angle-resolved photoemission spectroscopy (ARPES), STM and STS of the electronic and topological properties of a MHK lattice composed of DCA and Cu adatoms that is theoretically predicted to be an OTI. In Chapter 4, by changing the substrate and coordination atom, we disentangle the electronic properties of such networks and their interaction with the different substrates, looking again into their OTI character. The magnetic properties of selected 2D-MOFs coordinated with magnetic atoms are presented in Chapter 5. Chapter 6 shows the capabilities of these MHK lattices to nanostructure magnetic  $3d$  and  $4f$  met-

Table 1.1: Summary of the samples studied along this thesis by chapters. Columns classify by substrates and rows by coordination atom or nanostructured metal.

	Cu(111)	Ag(111)	Au(111)	Bi <sub>2</sub> Te <sub>3</sub>
Cu+DCA	chapter 3	chapter 4	chapter 4	
Co+DCA		chapters 4/5	chapters 4/5	chapter 4
Fe+DCA		chapters 4/5	chapters 4/5	
Sm/(Cu+DCA)	chapter 6			
Fe/(Cu+DCA)	chapter 6			

als when used as templates, providing also interesting magnetic properties. Finally, the main conclusions are presented in Chapter 7 and a summary in Spanish in Appendix A.

Table 1.1 summarizes all the studied samples classified by chapters. Since all the structures are formed with DCA molecules, each row corresponds to different coordination atoms, while the columns refer to the substrates. Finally, the two bottom rows indicate the templating effect of Cu+DCA/Cu(111) network upon metal evaporation.

## Chapter 2

# Experimental techniques

In this chapter we introduce the main experimental techniques used in this thesis. The first part gives an introduction on ultra-high vacuum (UHV) systems and the laboratory setup where most of the STM and low energy electron diffraction (LEED) experiments have been performed *in-situ*. Sample preparation is also detailed. The second part describes the main techniques used for morphological characterization, both in the long range scale (LEED) and locally (STM). In the third part, the spectroscopic techniques are introduced: STS, which is an extension of STM and studies the local density of states (LDOS), as well as XAS/XMCD and ARPES, spectroscopic techniques performed at synchrotron facilities. They provide spatially averaging information on the magnetic and electronic structure of the studied systems.

## 2.1 Ultra-High Vacuum Chambers

Atomically precise fabrication of 2D nanostructures and working with ultra-pure surfaces requires maximum cleanliness conditions. Sample contamination or adsorbates have to be avoided during the experiments. To this end, UHV conditions are required, which means pressures of the order of  $10^{-10}$  mbar. UHV multichamber systems are used to keep sample cleanliness during its preparation and characterization. To get such an environment, different vacuum pumps are used: roughing pumps (to get  $10^{-1}$  mbar) and turbo-molecular pumps (to lower the pressure down to  $10^{-11}$  mbar). Then, ionic and titanium sublimation pumps help to maintain these pressures.

Most of the experiments carried out during this thesis were performed at our home lab, which is located at the Advanced Microscopies Laboratory, within the Institute of Nanoscience and Materials of Aragon (University of Zaragoza-Spanish Research Council). It consists of an Omicron Nanotechnology equipment, that is mainly composed of a preparation chamber and a STM chamber (see Fig. 2.1). In the preparation chamber, sample cleaning, molecule and metal evaporation and a preliminary characterization with LEED can be

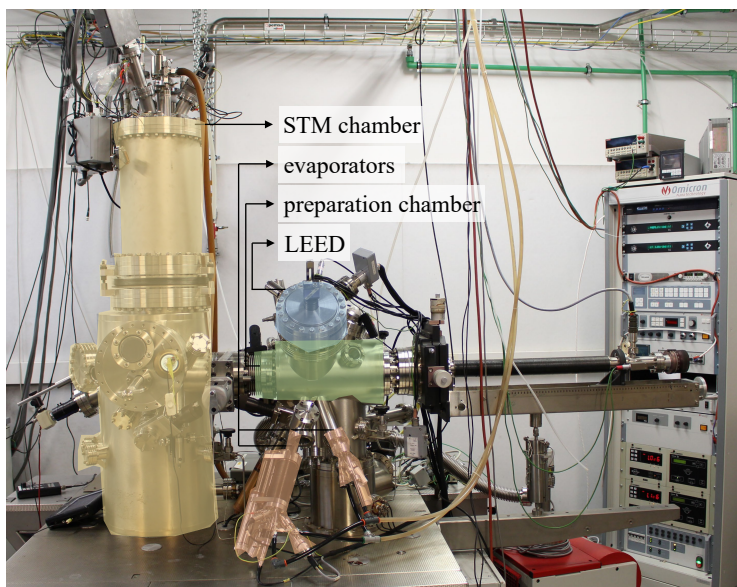


Figure 2.1: Lab setup composed of two main chambers. The STM chamber contains the STM itself and cryostats for liquid  $N_2$  and He. The preparation chamber contains the tools necessary for sample cleaning, LEED characterization and different evaporators. A load-lock chamber for fast substrate exchange completes the setup.

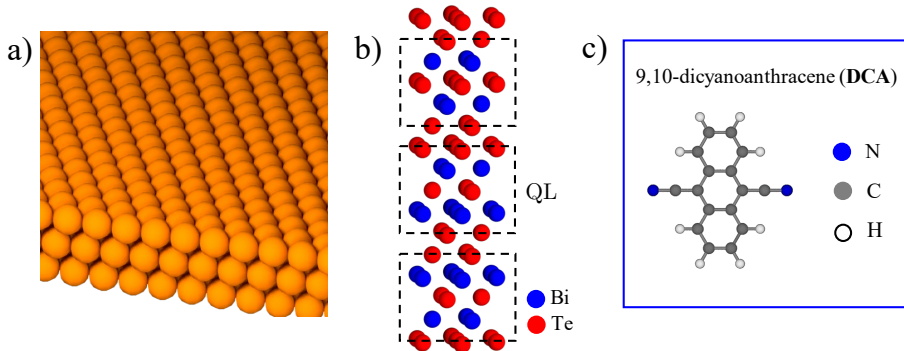


Figure 2.2: a) Ideal atomic structure of metallic fcc (111)-terminated substrates, b) Layered structure of Bi<sub>2</sub>Te<sub>3</sub> substrate, c) 9,10-dicyanoanthracene (DCA) molecule stick-ball model.

performed. The STM chamber contains the STM itself connected to an inner cryostat (generally filled with liquid He in order to keep samples at 4.2 K) that is thermally shielded by an outer one (filled with liquid N<sub>2</sub>). A load lock chamber to insert or remove substrates from the UHV chambers completes the system.

## 2.2 Sample preparation

Surface science experiments demand clean and atomically flat monocrystals as substrates for good quality sample preparation. To get rid of defects and contamination, metallic substrates (see Fig. 2.2a) are cleaned through subsequent cycles of ion sputtering and annealing. During the sputtering process, an atmosphere of  $10^{-6}$  mbar of Ar gas is introduced to the vacuum chamber. It is ionized and directed to the sample with a sputter gun at 1–2 kV and with an incident angle of  $55^\circ$  with respect to the crystal surface normal. During this process, the outermost atomic layers of the substrate are removed and a very rough surface is produced. A subsequent annealing provides thermal energy to reorder and recover atomically flat terraces of the surface. The temperature needed for this process varies for the noble metals we used during this thesis: it was required 820 K for Au(111) and Cu(111) and 620 K for Ag(111).

In Chapter 4, topological insulators, such as Bi<sub>2</sub>Te<sub>3</sub>, are also used as substrates (see Fig. 2.2b). Since they are layered materials, their surface preparation is different from the metallic substrates one. It consists of an exfoliation with adhesive tape performed under ultra-high vacuum conditions, in our case

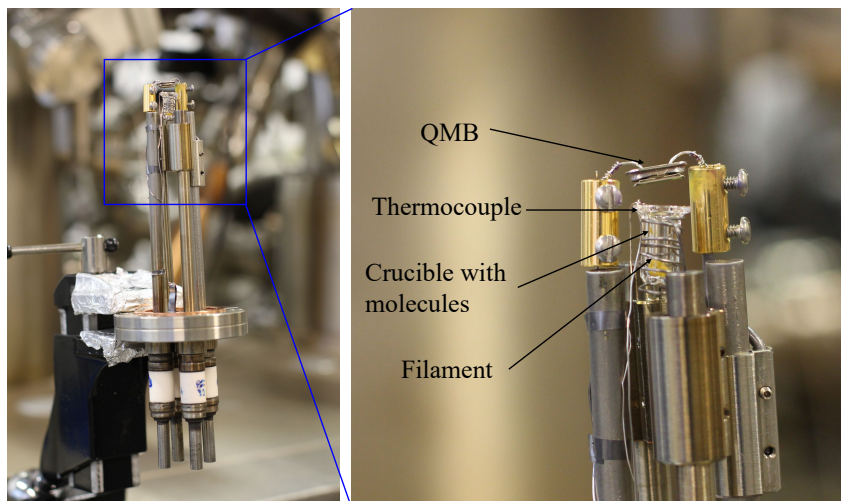


Figure 2.3: Homemade molecular evaporator consisting of a quartz crucible with a filament and thermocouple. A quartz micro-balance (QMB) located next to the crucible provides a control on the evaporation rate.

at the load lock chamber. The optically visible removal of many quintuple layers (QL) provides atomically fresh terraces on the surface.

The molecule used throughout this work to form the studied 2D-MOF is DCA (Figure 2.2c). DCA consists of an anthracene backbone and two cyano groups whose electric dipoles promote their bond with the coordination metal atoms. Molecular evaporation is carried out with a homemade evaporator made up of a Knudsen cell, shown in Figure 2.3. A quartz crucible is held in place by several filament windings to provide homogeneous heating inside it. The crucible also contains a thermocouple to measure the temperature as close to the DCA powder as possible. Close to the crucible, a quartz microbalance (QMB) allows us to control the molecular evaporation rate very precisely. When molecules reach  $\sim 80^{\circ}\text{C}$  they are sublimated into the chamber and stick on the substrate that is facing the crucible. The rate we use to prepare these 2D-MOFs ranges between  $\sim 0.025$  ML/min to  $\sim 0.075$  ML/min. Due to the molecules low vapor pressure, the evaporator is kept behind a valve and pumped by an external pump, and it is only opened to the preparation chamber during evaporation onto the substrate of interest.

Metal evaporation is performed with commercial *e*-beam evaporators from a rod in the case of Fe and Co or from a crucible in the case of Cu and Sm.



## 2.3 Low Energy Electron Diffraction

LEED is a diffraction technique used to determine surface structures, since their reciprocal lattice pattern can be directly imaged. It yields information on the periodicity and symmetry of surface structures with respect to the substrate unit cell [72]. This technique is based on the diffraction of monochromatic electrons. According to the particle-wave duality, the de Broglie wavelength of an electron can be calculated as  $\lambda = h/p$ ; where  $h$  is the Plank's constant and  $p$  the electron linear momentum. For non-relativistic velocities,  $p = m_e v$ , where  $m_e$  is the electron mass and  $v$  its velocity. Then:

$$\lambda = \frac{h}{m_e v} = \frac{h}{\sqrt{2E_{kin}m_e}}, \quad (2.1)$$

where  $E_{kin}$  is the kinetic energy of electrons. Therefore, the wavelength in nm units of a monochromatic beam of electrons can be calculated from their kinetic energy as:

$$\lambda[\text{nm}] \approx \sqrt{\frac{1.5}{E[\text{eV}]}}. \quad (2.2)$$

In this scenario, low energy electrons (20 – 200 eV) have wavelengths of the order of interatomic distances, allowing the study of surface structures. The diffraction momentum conservation conditions are determined by the Laue equations:

$$(\vec{k}_i - \vec{k}_f) \cdot \vec{a}_i = 2\pi k, \quad (2.3)$$

where  $\vec{k}_i$  and  $\vec{k}_f$  are the wavevectors of incident and scattered beams, respectively,  $\vec{a}_i$  is a real space lattice parameter and  $k$  is an integer number. When we are just interested in the overall surface morphology, only the elastically scattered electrons are analyzed. Then, energy conservation is required:

$$|\vec{k}_i| = |\vec{k}_f| \quad (2.4)$$

Both conditions (2.3 and 2.4) are represented by the Ewald construction, shown in Figure 2.4b. The reciprocal lattice of a 2D lattice is formed by rods (instead of spots in the case of a 3D lattice). The Ewald sphere is constructed by drawing  $\vec{k}_i$  in the direction of the incoming beam and ending in the (0,0) spot and then making a sphere of radius  $|\vec{k}_i|$  centered at the vector origin.

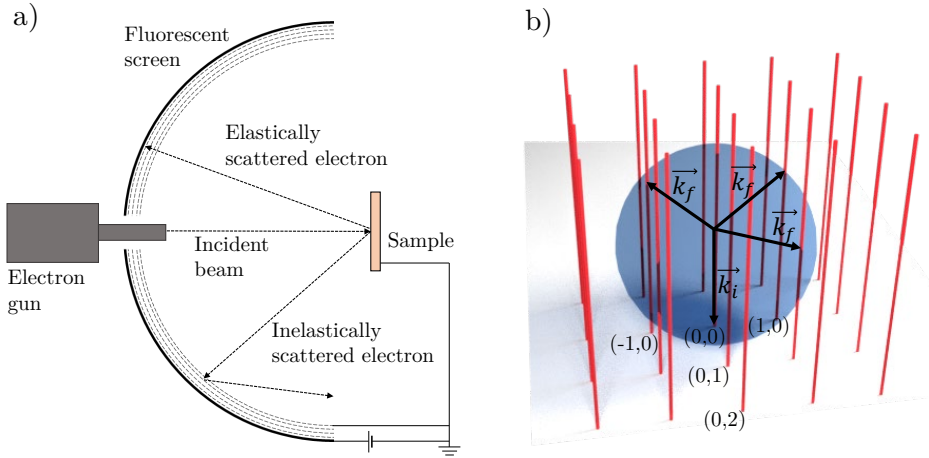


Figure 2.4: Low Energy Electron Diffraction technique. a) LEED setup scheme. Electrons produced at an electron gun are directed to the sample, where they are diffracted. Only elastically scattered electrons at the sample get to the fluorescent screen. b) Ewald sphere construction. Rods represent the reciprocal lattice of a square 2D lattice. The sphere radius depends on the energy of incident electrons. The intersection between the sphere surface and the rods, creates the elastic LEED pattern observable at this energy.

All the rods that intersect with the sphere satisfy the conditions stated in Equations 2.3 and 2.4 and therefore will be observed in the LEED pattern. They represent a direct measurement of the reciprocal lattice. As we increase the energy of the incoming electrons, the Ewald sphere expands and intersects with further rods and consequently, more spots will become visible at the LEED pattern. The spots that appear at higher energies correspond in real space to a smaller unit cell periodicities, according to Equation 2.2.

A LEED setup is schematically depicted in Figure 2.4a. Experimentally, the electron gun emits a collimated and monochromatic beam of electrons that are directed to the sample. Scattered electrons pass through energy filters where the inelastically scattered electrons are removed, and only the elastically scattered ones get to a fluorescent screen, where the pattern is formed. LEED is a surface sensitive technique because the elastic mean free path of low energy electrons is rather short. Thus, these electrons become easily inelastically scattered thereby being filtered before reaching the LEED fluorescent screen. The incident beam size is approximately of  $0.5 \text{ mm}^2$ , therefore LEED is an averaging technique. Then, surface structures must extend laterally at least along this area to observe a clear pattern.

## 2.4 Scanning Tunneling Microscopy

### 2.4.1 STM working principles

STM is a versatile microscopy technique consisting of a metallic and atomically sharp tip that is brought into close proximity to a conducting sample. A voltage applied between them produces a current that provides information on both, the topography and the density of states of the sample [1]. The quantum tunnel effect is the working principle of STM. According to classical mechanics, a particle with an energy lower than a potential barrier cannot go through it. However, in a quantum mechanical context, there is a non-zero probability for this to happen if the particle mass is small and the barrier is finite and narrow. Figure 2.5 represents a 1D-model of the tunnel effect. The solution of the Schrödinger equation at the potential barrier ( $0 \leq z \leq d$ ) is given by:

$$\psi(z) = \psi(0)e^{-kz}$$

where

$$k = \sqrt{2m(V_0 - E)/\hbar},$$

$m$  is the mass of the particle tunneling and  $E$  its energy,  $V_0$  is the barrier height, and  $\hbar$  is the Plank's constant divided by  $2\pi$ .

The probability of a particle to get across a barrier of width  $z = d$  is

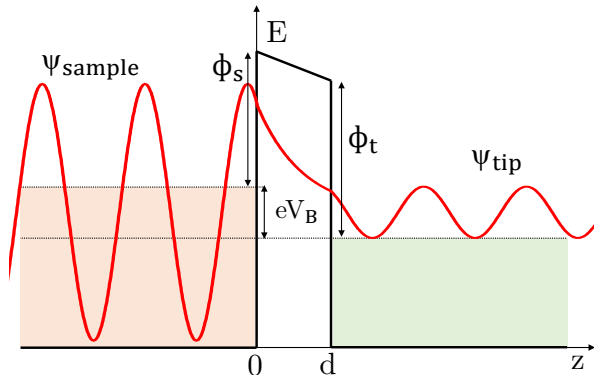


Figure 2.5: 1D model for electron tunneling from sample to tip separated by a distance  $d$  and with a negative  $V_B$  applied to the sample.  $\phi_s$  and  $\phi_t$  are the workfunctions of sample and tip, respectively. Electron tunneling probability from sample to tip decays exponentially with  $d$ .

calculated as:

$$P = |\psi(z = d)|^2 = |\psi(0)|^2 e^{-2kd}.$$

That is, the probability of tunneling a potential barrier decays exponentially with the barrier width. In the case of the STM, the particles tunneling are electrons with mass  $m_e$  and  $d$  is the distance between tip and sample, which is of the order of 1 nm. The tunneling current that flows between tip and sample decays exponentially with this distance, making STM a very sensitive probe to detect height changes, which is very useful to get insight on 2D nanostructures.

A more realistic model of tunneling junctions was proposed by Bardeen [73], who considered a metal-insulator-metal system where the sample and tip are the initial and final states, respectively, of the tunneling current. Then, the tunneling current can be expressed as:

$$I_t = \frac{4\pi e}{\hbar} \int_{-\infty}^{\infty} \rho_s(\epsilon - eV_B) \rho_t(\epsilon) [f_t(\epsilon) - f_s(\epsilon - eV_B)] |M(\epsilon, \epsilon - eV_B)|^2 d\epsilon,$$

where  $\rho_s$  and  $\rho_t$  are the density of states of sample and tip, respectively.  $f$  is the Fermi-Dirac distribution, that for liquid helium temperatures approaches to a step function and  $|M|$  is the tunneling matrix element, which, for values of  $V_B$  small compared to the workfunctions of tip and sample, can be considered

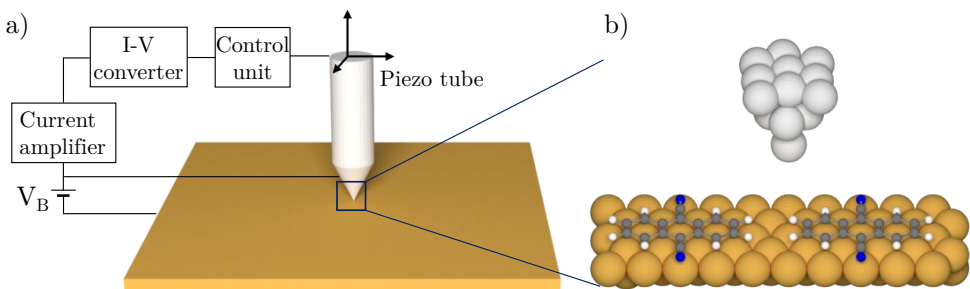


Figure 2.6: Schematic representation of a STM. a) Macroscopic view of a STM operating with feedback loop to control the tip position with respect to the surface. A bias voltage is applied between tip and sample.  $I_t$  is detected and amplified. Then, it is compared with the setpoint  $I_t$  and converted into a voltage that is applied to the piezo tube to correct x, y or z position. b) Atomic resolution of the tip apex. The tip is approached typically at 2 – 3 atomic heights of the sample to reach tunneling conditions.

## 2.4. Scanning Tunneling Microscopy

a constant [74–76]. Under these assumptions, the tunneling current expression is simplified to:

$$I_t \propto \int_0^{eV_B} \rho_s(\epsilon - eV_B)\rho_t(\epsilon)d\epsilon. \quad (2.5)$$

In essence, electron tunneling between tip and sample is a strongly sensitive probe for 2D samples; and the tunneling current, under some assumptions, depends mainly on the density of states of tip and sample.

Experimentally, the STM tip is approached to a distance of less than 1 nm to the sample and when a  $V_B$  is applied between them, typically tunneling currents of several hundreds of pA are measured. During this work, W tips fabricated by electrochemical etching were mainly used. The hardness of this material allows performing small tip indentations on Ag, Au or Cu metallic substrates to reorder the tip apex atoms or change its density of states. Figure 2.6 depicts a schematics of a STM. In order to get a topography image of the sample, the tip scans the desired area with a selected density of points. This scanning requires very precise tip movements, that are carried out with a piezo tube that directs movements in the three directions.

There are two different STM working modes: constant current mode and constant height mode, depicted in Figure 2.7. In the constant current mode,

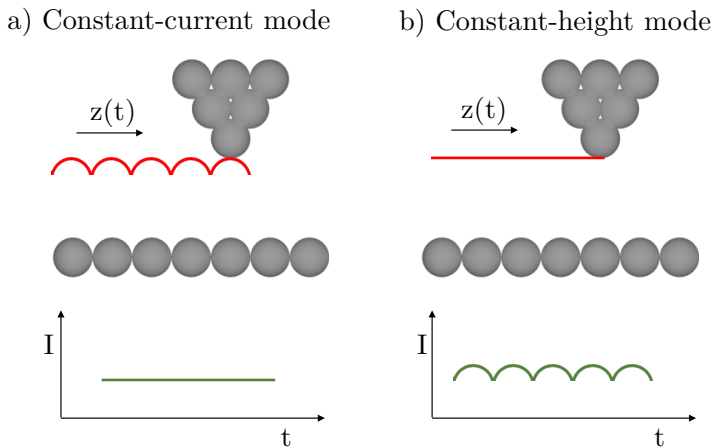


Figure 2.7: STM working modes. a) Constant-current mode works with a feedback loop that regulates  $z$  in order to keep a constant  $I_t$ . In this case the changes in height,  $\Delta z(x, y)$  form the topography image. b) In constant-height mode, the tip scans the sample with a fixed  $z$  and  $I_t(x, y)$  is recorded.

we preset a setpoint  $I_t$ . At each point of the sample, a feedback loop regulates the tip  $z$  position in order to detect such  $I_t$ . The topography image is formed by the change in  $z$  occurring at each point to maintain constant the setpoint  $I_t$ ; that is  $\Delta z(x, y)$ . In the constant height mode, the feedback loop is off. Here, the sample is scanned with the tip with a fixed  $z$  position and the measured  $I_t$  is recorded and the image is formed by  $I_t(x, y)$ . Constant current mode is most frequently used to avoid undesired tip crashes when scanning a sample, while constant height mode is often used for  $dI/dV$  spectroscopy maps or high-resolution images with CO-functionalized tips.

## 2.4.2 CO tip functionalization

Despite STM being an imaging technique capable of providing atomic resolution, in organic samples the extended and conjugated character of their molecular orbitals makes difficult to gain insight on their internal chemical structure. However, STM imaging with the tip functionalized with a CO molecule can provide bond-resolved imaging at zero bias. This happens when a CO molecule located at the tip apex and the organic sample are in close proximity, due to an interplay between van der Waals attractive and Pauli repulsive forces [77, 78].

The tip functionalization starts by having a quantity of CO molecules on the substrate enough to easily find them close to the area we are scanning. In our case, a pressure of  $10^{-8}$  mbar of CO is injected to the chamber and the STM shields are open for typically 2 – 3 minutes with the sample at cryogenic temperatures. In order to functionalize the tip, a CO molecule is picked by vertical manipulation: the tip is placed on top of a CO molecule at the substrate

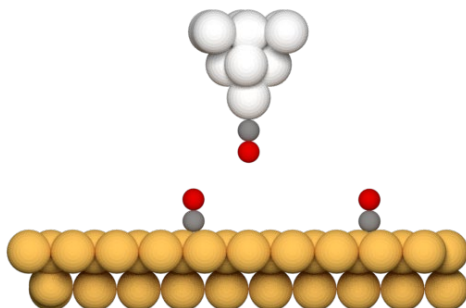


Figure 2.8: CO tip functionalization. CO molecules are adsorbed on the surface through their C atom, and they are attached to the tip also bonding through its C.

and, with the feedback loop off, is approached slowly until the molecule jumps to the tip apex (see Figure 2.8). The sample is scanned in constant-height mode approximately zero bias, in order to remove orbital contribution from the signal, and consequently, C-C bonds in organic structures are resolved. A commonly used data treatment consists in differentiating the image with respect to both spatial image directions (Laplacian filter) to visualize more clearly the bond-resolved chemical structure.

### 2.4.3 Scanning Tunneling Spectroscopy

Scanning Tunneling Spectroscopy is a STM-related technique to probe the electronic structure at a particular spatial position on surfaces. It mainly consists of recording differential conductance ( $dI/dV$ ) as a function of the bias voltage. Differentiating Equation 2.5 with respect to  $V_B$  and assuming as a constant the tip density of states, the expression becomes:

$$\frac{\partial I_t}{\partial V_B} \propto \rho_t \rho_s(\vec{r}, eV_B). \quad (2.6)$$

Which means that, under all the assumptions done,  $dI_t/dV_B$  provides a direct measurement of the density of states of the sample (and tip) at that particular position of the surface with high spatial resolution. To obtain a  $dI/dV$  spectrum, the tip is located at a specific point with the feedback loop open and

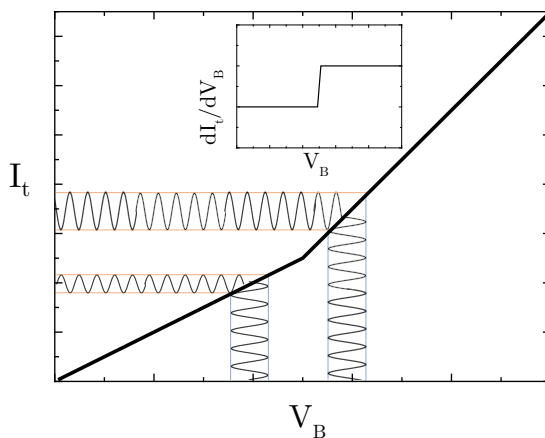


Figure 2.9: STS operation scheme with the lock-in technique. Since the excitation amplitude of the  $V_B$  signal is constant, the resulting amplitude of the  $I_t$  oscillation signal is a direct measurement of the  $I - V$  curve slope. In the inset graph,  $dI_t/dV_B$  spectrum obtained following the slope of the curve at each voltage.

then  $V_B$  is ramped while changes in  $I_t$  are recorded. The obtained  $I - V$  curve can be differentiated to calculate differential conductance. However, with this method several spectra must be measured to reduce the noise appearing when differentiated. Another option is to use the phase sensitive detection technique, which makes use of a lock-in amplifier. Its working principle is represented in Figure 2.9. With this method, the continuous signal of  $V_B$  is excited with a sinusoidal signal with a small amplitude  $V_{mod}$ :

$$V_{STS} = V_B + V_{mod} \sin(\omega_V t + \varphi_V) \quad (2.7)$$

As a consequence, since the feedback is loop off, the current provides also an oscillating response:

$$I_{STS} = I_t + I_{mod} \sin(\omega_I t + \varphi_I) \quad (2.8)$$

As represented in Figure 2.9, the oscillating current amplitude,  $I_{mod}$ , is a direct measurement of the slope of the curve, which is equal to the differential conductance. It can be obtained with a very high signal-to-noise ratio by the phase sensitive detection method, carried out with a lock-in amplifier. In practice, the tip is located at a point of the sample with the feedback loop off. Then, the  $V_{STS}$  constant component is ramped, and from the output lock-in signal, a  $dI_t/dV_B$  ( $V_B$ ) spectrum is obtained, which corresponds to the local density of states at this spatial point.

## 2.5 X-ray Absorption Spectroscopy and Magnetic Circular Dichroism

XAS is a versatile tool to explore the electronic structure and oxidation state of elements [79]. An absorption edge is an abrupt rise of an element X-ray absorption coefficient that occurs when the X-ray energy is high enough to excite a core electron to an empty level due to the photoelectric effect. These edges are named as K, L, M, etc., according to the atomic core shell where the electron leaves a vacancy (n=1, 2, 3 respectively), and their energies are characteristic for each element. Then, in an absorption event, a photon of a specific energy is absorbed by a core electron that is excited to the valence band. An absorption event is essentially an electric process in which the electron spin remains unchanged. This process will only take place when this specific X-ray energy matches with the difference between core and valence levels on a specific element. This makes XAS, and all related techniques, element and



band specific, which is one of its main advantages. X-rays in the range of 100 – 2000 eV belong to the soft X-rays region and comprise the absorption on  $3d$  band in transition metals and  $4f$  in lanthanides, useful for the study of their magnetic properties.

If the experiment requires so, the sample can be located under UHV conditions and/or cryogenic temperatures. A XAS spectrum is obtained by recording the absorption measured for each incident X-ray beam energy, which is scanned along the desired energy range. The X-ray absorption detection can be carried out by different methods. The one used along the experiments presented in this thesis is the total electron yield (TEY) method. When the excited electrons are relaxed back to their core states, Auger electrons are emitted. By inelastic scattering, they generate secondary electrons. Due to their short mean free path, the number of secondary electrons escaping the sample is an accurate measurement of the sample absorption. This signal is then normalized by the beam intensity in order to remove contribution from beam variations. Since XAS technique is used for the study of magnetic elements, these endstations are equipped with a superconductive magnet of typically 6 – 9 T applied parallel to the beam. Moreover, samples can be rotated with respect to the beam direction in order to get information on their anisotropic properties (such as magnetic anisotropy). The synchrotron spotlight is of the order of  $0.5 \text{ mm}^2$ , then studied structures have to be uniform at least in this area in order to obtain coherent data.

X-ray Magnetic Circular Dichroism is a XAS technique providing information on the magnetization and orbital and spin magnetic moments of systems in an element-specific manner [80, 81]. It is calculated as the difference between two XAS spectra acquired with left- and right- circularly polarized photons (see Fig. 2.10b). This process can be explained using the two-step model, which is depicted in Figure 2.10a for the specific case of  $3d$  band absorption. In the first step, a core electron is excited by a circularly polarized photon. Then, due to angular momentum conservation, the photon transfers its angular momentum to the excited electron. At the  $2p$  core state, spin-orbit coupling produces a splitting in two levels (see Fig. 2.10a):  $2p_{3/2}$  (that will produce the  $L_3$  edge), where  $J=L+S$  and  $2p_{1/2}$  (corresponding to  $L_2$  transitions), where  $J=L-S$ . Positive (negative) helicity photons will excite at the  $2p_{3/2}$  level 62.5% (37.5%) of spin-up electrons and 37.5% (62.5%) of spin-down. At the  $2p_{1/2}$  level, positive (negative) photons will excite 25%(75%) spin-up electrons and 75%(25%) spin-down electrons. If the sample has a net magnetization, then an imbalance between absorption at both polarizations will be detected, meaning a difference between spin-up and spin-down electrons in the spin-split valence

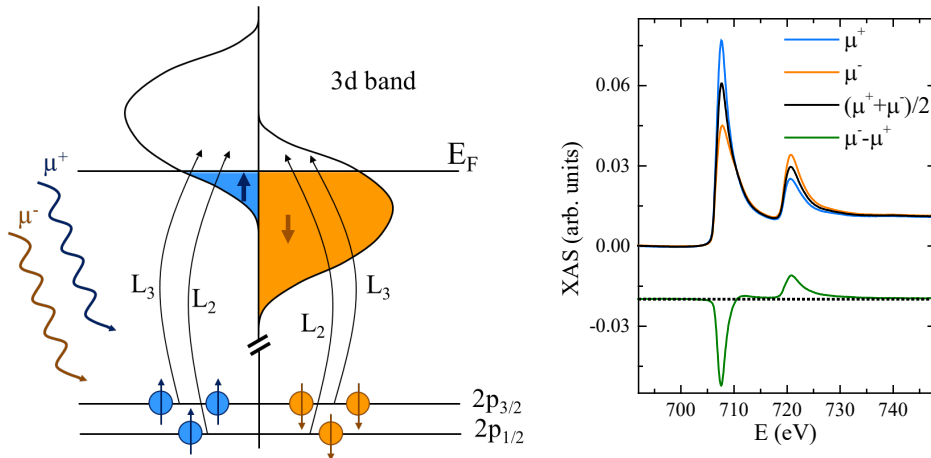


Figure 2.10: a) Absorption process at the  $L_{2,3}$  edges of a  $3d$  metal for left ( $\mu^-$ ) and right ( $\mu^+$ ) circularly polarized light. b) Fe XAS absorption with both polarities and their average. In green, XMCD spectrum obtained as  $\mu^- - \mu^+$ .

band.

XMCD experiments involve recording XAS spectra with right- and left-circularly polarized light in the same conditions. They are typically acquired at maximum magnetic field (which can be 6–9 T depending on the beamline). In order to get information on the magnetic anisotropy, the sample can be rotated at different angles with respect to the beam and magnetic field. Also, single-element magnetization curves can be performed by measuring XMCD maximum as a function of magnetic field.

### 2.5.1 Data analysis and the sum rules

As shown in Figure 2.10b, a XMCD spectrum is calculated as the difference between spectra with both polarities, while a XAS spectrum is their average. Typically, several measurements of each polarity are acquired in order to get better signal-to-noise ratio. Then, a background signal is usually removed from them, especially in samples with low concentrations of magnetic elements.

This technique is very useful because it allows to obtain an estimation of the orbital and spin contributions to the total magnetic moments in an element-specific manner. To do so, we make use of the sum rules, derived by P. Carra,

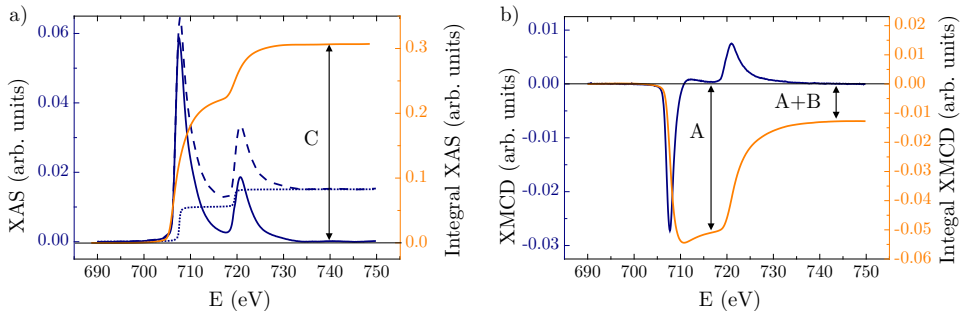


Figure 2.11: Parameters for sum rules calculations. a) A double-step function is subtracted to XAS spectra to remove transitions to continuum. Then, it is integrated to obtain the contribution of  $L_{2,3}$  edges, C. b) XMCD spectrum and its integral for the extraction of parameters A and B.

B.T. Thole and G. van der Laan in the 90's [82, 83]. They can be expressed as:

$$\mu_L = -\frac{2}{3} \frac{A+B}{C} n_h \quad (2.9)$$

$$\mu_S^{\text{eff}} = \frac{2B-A}{C} n_h \quad (2.10)$$

where  $n_h$  is the number of holes in the final electron states band (in the case described in Figure 2.10a, the  $3d$  band),  $A$  and  $B$  are the area enclosed in the  $L_3$  and  $L_2$  edges of the XMCD spectrum, respectively, and  $C$  is the area enclosed in both edges of the XAS spectrum. These values are calculated through the XAS and XMCD signals integration, as presented in Figure 2.11. In order to remove contribution from transitions to the continuum, a double-step function is subtracted from the XAS spectrum before its integration.

The obtained parameter in equation 2.10 is  $\mu_S^{\text{eff}} = \mu_S - \frac{7}{2} \mu_T$ , where  $\mu_S$  is the spin moment and  $\mu_T$  the spin-quadrupole.

## 2.6 Angle-Resolved Photoemission Spectroscopy

ARPES is a spectroscopic technique based on the photoelectric effect. It provides information on the valence band electronic structure through the analysis of the kinetic energy and direction of emitted electrons. In an ARPES experiment, the sample is illuminated with a monochromatic beam of photons that are absorbed by the sample electrons. If the photon energy is high enough,

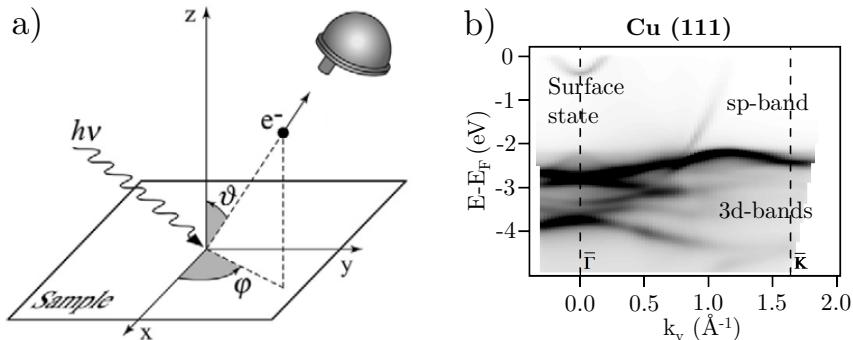


Figure 2.12: a) ARPES experimental scheme. The sample is exposed to monochromatic light. Photoelectrons emitted from the sample are then analyzed as a function of their kinetic energy and direction to get information on their band structure. Image taken from reference [84]. b) Band structure of a Cu(111) substrate using photons of  $h\nu = 21.22$  eV (He  $I_{\alpha}$ ). The surface state, a volume highly dispersive  $sp$ -band and 5 fully occupied  $3d$ -bands can be distinguished.

photoelectrons will be emitted from the sample with a kinetic energy ( $E_{kin}$ ), and a direction defined by the angles  $\vartheta$  and  $\varphi$  (see Figure 2.12a). The numbers of those electrons are collected by an electron energy analyzer defining the kinetic energy for each direction point. From  $E_{kin}$  we can obtain the binding energy and from  $E_{kin}$  and the direction, the momentum of the electrons inside the solid. In other words, the sample valence band-structure can be determined (see Figure 2.12b). ARPES can only access occupied states, when using normal discharge lamps or synchrotron beams. Electrons in ARPES have typically  $E_{kin} < 100$  eV, so they have a minimal mean free path, according to the Universal curve. Therefore, electrons detected in the energy analyzer come only from the outermost surface layers, making ARPES a surface sensitive technique. The light used in these experiments is generally provided by gas discharge lamps or by synchrotron light sources. Also, as well as LEED or XMCD, it is an averaging technique, due to the size of spot of  $\approx 0.5$  mm<sup>2</sup>.

All the ARPES measurements presented here were performed at Elettra synchrotron in Trieste as well as in our collaborators home lab in the Materials Physics Center (CFM) in San Sebastian.

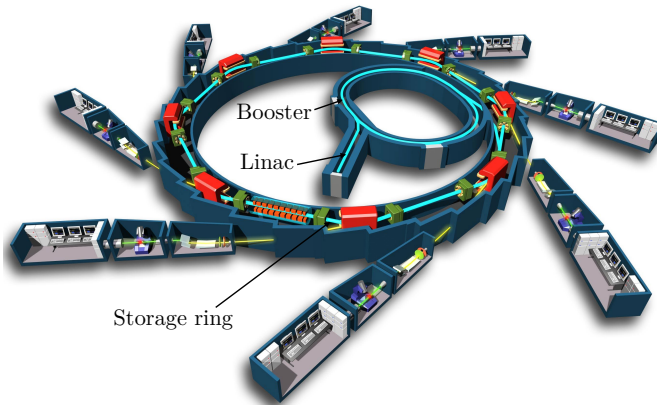


Figure 2.13: Synchrotron facility schematics. Its main parts can be identified: the linear accelerator, the booster and the storage ring, as well as the different beam lines that use synchrotron radiation.

## 2.7 Synchrotron facilities

XAS, XMCD and ARPES measurements are carried out in synchrotron facilities because they provide highly brilliant X-rays whose energy and polarization can be precisely tuned. Synchrotron facilities are particle accelerators used to obtain synchrotron electromagnetic radiation. Their working principle is based on the radiation emitted by accelerated electrons. When a charged particle follows a curved trajectory emits electromagnetic radiation tangentially to its trajectory due to its centripetal acceleration. Synchrotron facilities make use of this phenomenon to produce very brilliant and collimated light. Modern synchrotron sources are constituted by three main blocks (see Figure 2.13):

- **Linac:** is the linear accelerator. At the first part of the process, electrons are produced by a thermoionic gun and accelerated linearly by a strong electric field.
- **Booster:** is composed of linear and curved tracks with radiofrequency cavities. Here, electrons are accelerated up to their nominal energy and packed in bunches.
- **Storage ring:** where electrons circulate at their nominal energy, very close to the speed of light, and produce synchrotron radiation which is directed to the different beam lines. It is formed by curved and straight sections. Undulators are used to bend the electrons trajectory and produce synchrotron light with the desired polarisation (linear, circular...)

in a specific energy range which is optimized for each beam line. Radiofrequency cavities are also installed in order to recover the energy lost by the radiation emission.

Once the radiation has been emitted, a monochromator formed by a system of diffracting grids (or crystals in higher energy ranges) is placed before the end station in order to get a monochromatic beam with the possibility of a very precise tuning of its energy. They are connected to the undulators to optimize the beam flux.

All the XAS/XMCD measurements presented in this work were performed at BOREAS beamline in ALBA Synchrotron in Barcelona, and ID32 beamline in ESRF, Grenoble. The ARPES experiments in Chapter 3 were done in the APE beamline at Elettra synchrotron, Trieste. These beamlines were equipped with preparation chambers similar to those described in section 2.2 and samples were prepared following the same protocols.

## Chapter 3

# Searching for organic topological insulators

In this chapter we unravel the electronic structure from a MHK lattice theoretically predicted to be an OTI [55]. Given that mainly local techniques have been used to investigate the electronic structure of MHK lattices [53–57], the existence of extended network states has not been demonstrated. To date, no experimental bands have been reported for 2D-MOFs, so the electronic conjugation in MHK lattices is still awaiting confirmation. The expected multi-band should be similar to 2D covalent organic frameworks (2D-COFs) [85, 86], which are truly 2D conjugated polymers and organic analogues of graphene [12, 14, 87–94], but lack topologically protected edge states because of the absence of metal centers that provide the necessary SOC to become OTIs. Also, we look for an explanation to the generalized absence of edge states found in this and other MHK lattices that were expected to be OTIs [65–68].

To do so, we grow a 2D-MOF consisting of DCA molecules and Cu adatoms, that is predicted to be an OTI, on Cu(111) [55]. It is a MHK lattice of exceptional quality that is extended, single-domain and practically defect-free. These optimal growth conditions allow us to study its electronic structure both locally, using STM/STS, and mesoscopically, using ARPES. We find an extended kagome network multi-band without edge states at the island borders. The unexpected structural asymmetries that we detect by means of bond-resolved constant height measurements using CO-functionalized tips can qualitatively explain this absence based on systematic tight-binding model calculations. Such a collection of results allows us to pinpoint mechanisms that make our MHK lattice a topologically trivial system that quenches the edge

states. These results were published in *Nanoscale* [95].

## 3.1 Results and discussion

### 3.1.1 Network formation and morphology

The Cu+DCA/Cu(111) 2D-MOF is generated at room temperature (RT) by the evaporation of DCA molecules on a Cu(111) substrate (see Fig. 3.1a-c). The latter provides Cu adatoms for coordination that self-assemble with DCA molecules through their cyano groups, forming a unit cell with 3 DCA molecules and 2 Cu adatoms (see Fig. 3.1c) [96, 97]. In this array the Cu adatoms form a honeycomb lattice that is interwoven with a kagome structure resulting from connecting the molecular centers. 2D networks require the existence of these two lattices, as well as enhancing of the SOC, to become OTIs [55–57]. The increase of SOC with respect to the organic molecules is here provided by the Cu adatoms that form the honeycomb lattice. As presented in Figure 3.1c, this structure leaves small cavities, forming a porous network. The network structure is regular, single-domain and it exhibits long-range order with a very small amount of defects (see Figure 3.1a, b). It follows the symmetry direction of the underlying Cu(111) substrate. Indeed, the network is commensurate with the substrate, displaying an  $(8 \times 8)$  LEED pattern (Fig. 3.1d). We refer to a monolayer (ML) of molecules as the quantity required to cover all the substrate with this porous phase (see Figure 3.1a). By depositing a sub-monolayer of DCA we get islands of the network as the ones in Figure 3.1e, f. Note that in sub-monolayer configurations, all the islands have the same domain arrangement even if they are in different substrate terraces. At their borders, edge states should be observable if it was a topological insulator. From direct STM measurements and from LEED patterns, the lattice parameter calculated as the pore-pore distance is  $2.04 \pm 0.03$  nm.

### 3.1.2 Electronic characterization by ARPES

To unequivocally clarify whether this network is an OTI, we need to characterize its electronic structure and check for the existence of extended network multi-bands that would evidence its electronic conjugation. The excellent growth quality of the network allows us to do so mesoscopically by ARPES, as shown in Figures 3.2 to 3.4 (see also Figures 3.9 to 3.12 in the Supplementary material section). Figure 3.2 compares the ARPES signal of a clean Cu(111)



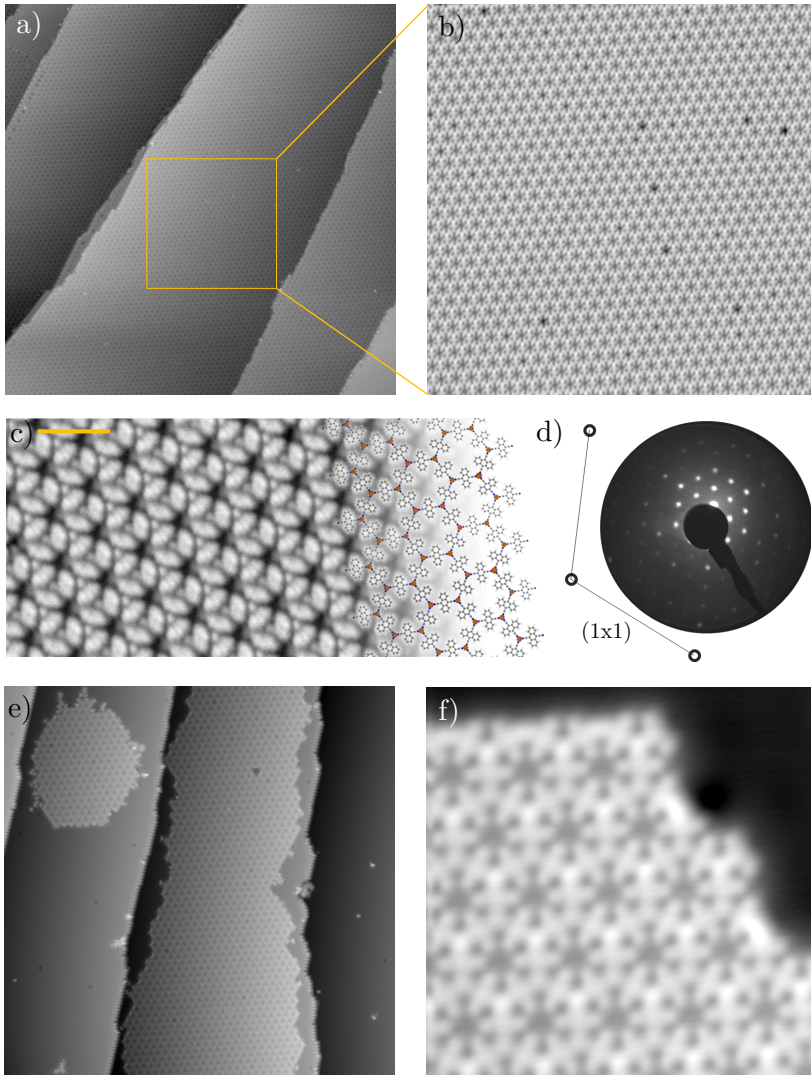


Figure 3.1: Cu+DCA/Cu(111) network probed by STM and LEED. a) and b) display STM overviews of a network monolayer presenting a single domain along different atomic steps with a very low quantity of defects. c) Close up of the network with an schematic model overlaid. d) LEED pattern of the extended 2D-MOF acquired at RT presenting a  $(8 \times 8)$  commensurate arrangement with the substrate. e) Sub-monolayer DCA deposition condensed into single-domain large islands. f) Detail of an island border, where an edge state should be hosted if the 2D-MHK lattice is an OTI. Image parameters: a)  $150 \times 150 \text{ nm}^2$ ,  $I_t = 100 \text{ pA}/V_B = -1 \text{ V}$ ; b)  $50 \times 50 \text{ nm}^2$ ,  $I_t = 100 \text{ pA}/V_B = -1 \text{ V}$ ; c) Scalebar=3 nm,  $I_t = 300 \text{ pA}/V_B = -1 \text{ V}$ ; d)  $E = 25 \text{ eV}$ ; e)  $100 \times 100 \text{ nm}^2$ ,  $I_t = 100 \text{ pA}/V_B = -1 \text{ V}$  f)  $10 \times 10 \text{ nm}^2$ ,  $I_t = 100 \text{ pA}/V_B = -1 \text{ V}$ .

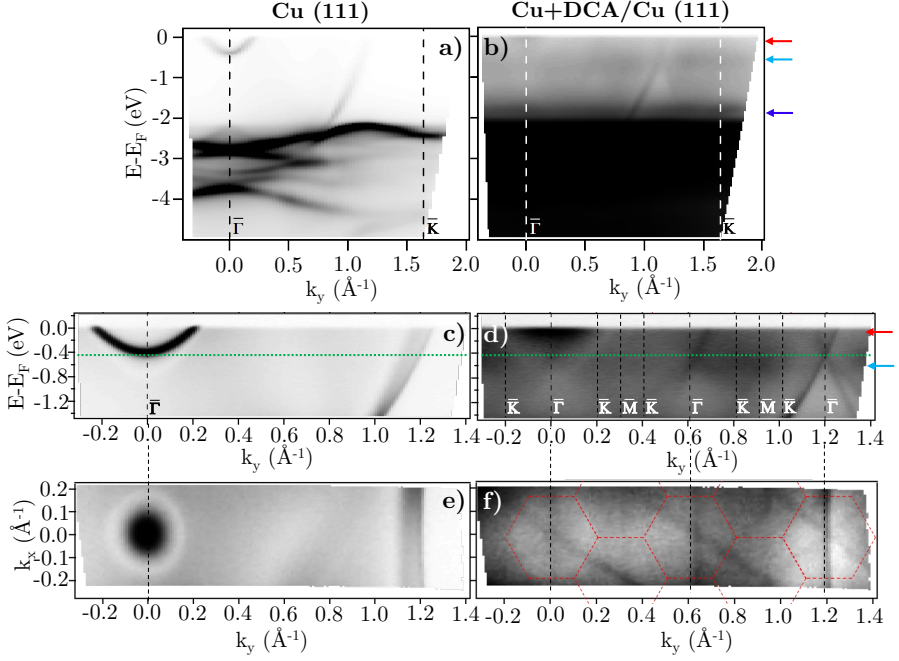


Figure 3.2: ARPES characterization before and after the network formation. a), c), e) represent different plots of the electronic structure of a clean Cu(111) substrate measured with ARPES. b), d) and e) correspond to the same measurements performed after the network formation, which evidence a change in its electronic structure. e) and f) contains an isoenergetic cut at 0.42 eV (marked by the green, dotted line in the panels above). In all the plots, the darker contrast represents higher intensities. Note that in b, the intensity is saturated to visualize surface-related features, since the volume  $d$ -bands contribution is very strong. The horizontal green dotted line is close to the fundamental energy of the surface state of Cu(111), which is upshifted due to the presence of the network on the surface. The discontinuous hexagons in f indicate the Brillouin zone of the network, which is smaller than the substrate one. The colored arrows in the right indicate the three states related to the 2D-MHK lattice and explained in the text. ARPES parameters:  $h\nu = 21.2$  eV (He  $I_\alpha$ );  $T_S = 150$  K.

substrate with the one of a monolayer of network. In the Cu(111) measurement, we can distinguish different bands. The surface state, centered at the  $\bar{\Gamma}$  point, featuring free-electron character (parabolic dispersion) and with a fundamental energy of  $(E-E_F)=-0.4$  eV. The highly dispersive band which is located at  $k_y \sim 1.0 - 1.25 \text{ \AA}^{-1}$  above  $-2$  eV is the volume  $sp$ -band, and the bands between  $-2$  and  $-3$  eV constitute the volume  $d$ -bands.

In the case of the network ARPES signal (Fig. 3.2b, d, f), these features are strongly modified, which provides evidence of an electronic structure change. Figure 3.3a presents this progressive evolution as a function of the network coverage on the surface. The upper plot corresponds to the clean Cu(111) substrate, whereas the one at the bottom corresponds to almost a monolayer coverage. Then, the middle ARPES plots correspond to sub-monolayer regimes, characterized by the presence of network islands. At the bottom one, where the surface is almost saturated with the network, we observe three main features that we discuss in the following: i) strong, highly dispersive bands, ii) residual intensities close to the Fermi energy ( $E_F$ ) at the  $\bar{\Gamma}$  points and, iii) a weak, broad state around  $-0.6$  eV.

To discriminate whether these bands have a bulk or surface origin, we probed the photoemission signal at different photon energies at the synchrotron facility of Elettra (APE beamline) (see Fig. 3.3b). We find that the dominant, highly dispersive bands change their energy and momentum with photon energy, so they must originate from bulk bands. Indeed, they are band umklapps resulting from folding the  $sp$ -bands of Cu(111) into the  $(8 \times 8)$  network periodicity. The exceptional quality of the network can be judged by the umklapp perfection in the ARPES signal (cf. Fig. 3.2).

The two other detected features are surface-related states since they do not change their energy and momentum upon photon energy variations. As the network progressively covers the surface, they either shift towards the Fermi level or gain intensity (see Fig. 3.3a). Both features can be better visualized at Figure 3.4a with a shorter energy window that excludes the  $d$ -bands or at 3.4b, in a second derivative of the signal integrated along  $k_x$ . In the case of the state closest to the Fermi level around the  $\bar{\Gamma}$  points, its origin is the altered Shockley surface state that is confined at the network pores and forms a delocalized band [98–101]. Such confinement produces an upshift in energy, while the broadening of this feature is produced by a certain degree of delocalization. However, the dispersion of this band cannot be detected in ARPES because its weight predominantly lies in the unoccupied region (above the Fermi level). Contrarily, the state centered at  $-0.6$  eV is entirely in the occupied region

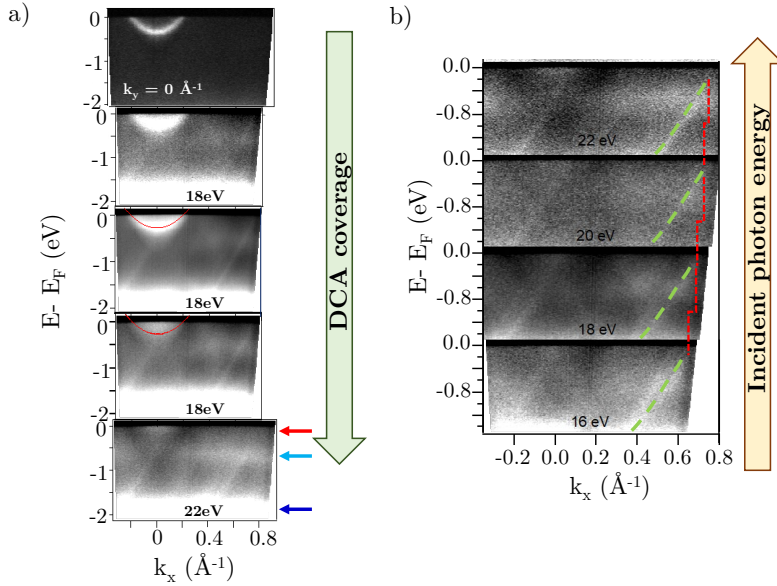


Figure 3.3: ARPES measurements as a function of the molecular coverage and of the incident photon energy. a) ARPES plots as a function of network coverage. The upper one corresponds to the clean Cu(111) substrate, where the only feature is the surface state. As the network coverage increases, other features appear and the SS shifts towards  $E_F$ . Once again the colored horizontal arrows at the bottom mark the 2D-MOF related features. b) ARPES plots taken with different incident photon energies evidence that the dispersive bands highlighted in green are bulk bands, since their momentum and energy are modified. The rest of intensities observed, are surface-related features. In all the plots, brighter features correspond to higher intensities and  $k_y = 0$ .  $T_S = 78$  K.

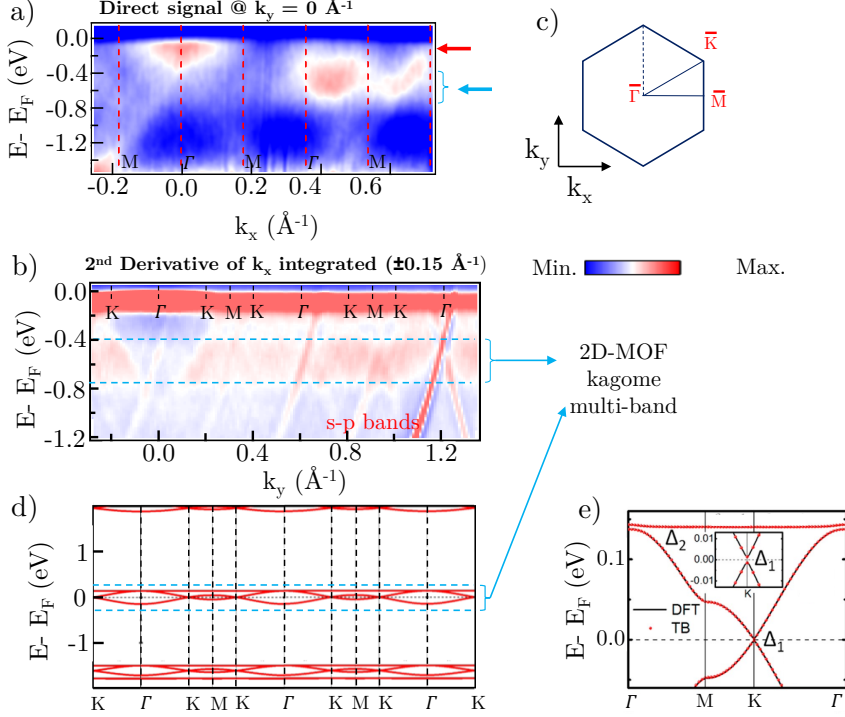


Figure 3.4: Electronic structure of the Cu+DCA/Cu(111) network close to saturation studied by ARPES. a) ARPES spectral function recorded along the  $\overline{\Gamma M}$  direction ( $k_y = 0$ , which in the real space is orthogonal to the shortest pore-pore direction). The color scale of the direct intensity is shown on the right. b) Second derivative of the integrated ARPES signal between  $k_x = \pm 0.15 \text{ \AA}^{-1}$  along the  $\overline{\Gamma K}$  direction. In a) and b) the highly dispersive bands correspond to umklapps of the bulk  $sp$ -bands, whereas the intensity at around  $-0.6 \text{ eV}$  (blue arrow) stems from the network. The intensity close to the Fermi level in a) at the  $\overline{\Gamma}$  points corresponds to the pore confined surface state. The vertical discontinuous lines indicate high-symmetry points. c) Sketch of the Brillouin zone and high-symmetry points of the network [8 times smaller than that of the Cu(111) substrate].  $k_x$  runs parallel to the  $\overline{\Gamma M}$  direction, whereas  $k_y$  is perpendicular to it. d) Repeated band structure reproduced from ref. [55] where the free-standing kagome multi-band is located at the Fermi energy. e) Close up of this band structure where the mini-gaps in which edge states should be hosted are visible. ARPES parameters: a)  $h\nu = 18 \text{ eV}$ ;  $T_S = 78 \text{ K}$ ; b)  $h\nu = 21.2 \text{ eV}$  (He  $I_\alpha$ );  $T_S = 150 \text{ K}$ .

and features an overall bandwidth of  $\approx 200$  meV according to the integrated ARPES intensity (see Figs. 3.4 and 3.11). We discard its origin as a discrete molecular orbital [102, 103] since no trace of such state exists at this energy when molecules are uncoordinated with the Cu metal centers [97, 104]. Instead, this broad state gains intensity as the network coverage increases and is the expected kagome multi-band of a 2D-MOF. Despite this MHK lattice not being covalently bonded, the conjugated band manifold is of comparable quality to the one recently reported for a 2D-COF [86]. Interestingly, the prediction for this free-standing OTI band manifold is around the Fermi energy (see Fig. 3.4d, e) [55] so the kagome multi-band is downshifted by the Cu(111) substrate presence.

### 3.1.3 Electronic characterization by STS

Finding such 2D-MOF kagome multi-band fulfills the first requisite for our system to host edge states as an OTI. In the following, we use scanning tunneling spectroscopy to access the local density of states (LDOS) of this electronically conjugated MHK lattice and compare it to the ARPES datasets. Figure 3.5c shows several differential conductance ( $dI/dV$ ) spectra at selected network positions (marked with coloured dots in the inset image), where we detect several prominent peaks. Figure 3.5d-h displays their spatial distribution extracted from  $dI/dV$  grid maps at the corresponding energies, while Figure 3.5i-m shows schematic models of these states. From higher to lower bias, we find the first complete peak at  $\sim 0.8$  V maximizing at the center of the molecules. We attribute this peak to the network’s first unoccupied molecular orbital that is quite localized in the central ring (it is practically absent at the DCA lobes) and weakly extends throughout the network. We name hereafter this state as LUMO. However, at  $\sim 1.5$  V we also detect a peak onset at the molecular center position that extends out from our energy range. Further down, the next prominent peak is found at  $\sim 0.2$  V, which maximizes at the pore center. This has been previously identified as the Cu surface state  $n = 1$  confined resonance [97] that results from the scattering at the potential barriers generated by the 2D-MOF. Nevertheless, this peak carries significant intensity at every position of the MHK lattice indicating a delocalized character. This agrees with ARPES, since we observe that the peak’s onset is just below the Fermi energy (at  $-0.1$  V), which matches the state found at the  $\bar{\Gamma}$  points that leads to a dispersive quantum dot array band [98–101].

Next, we find in STS a peak centered at  $\sim -0.6$  V, which coincides with the previously identified 2D-MOF kagome multi-band with  $\approx 200$  meV bandwidth.

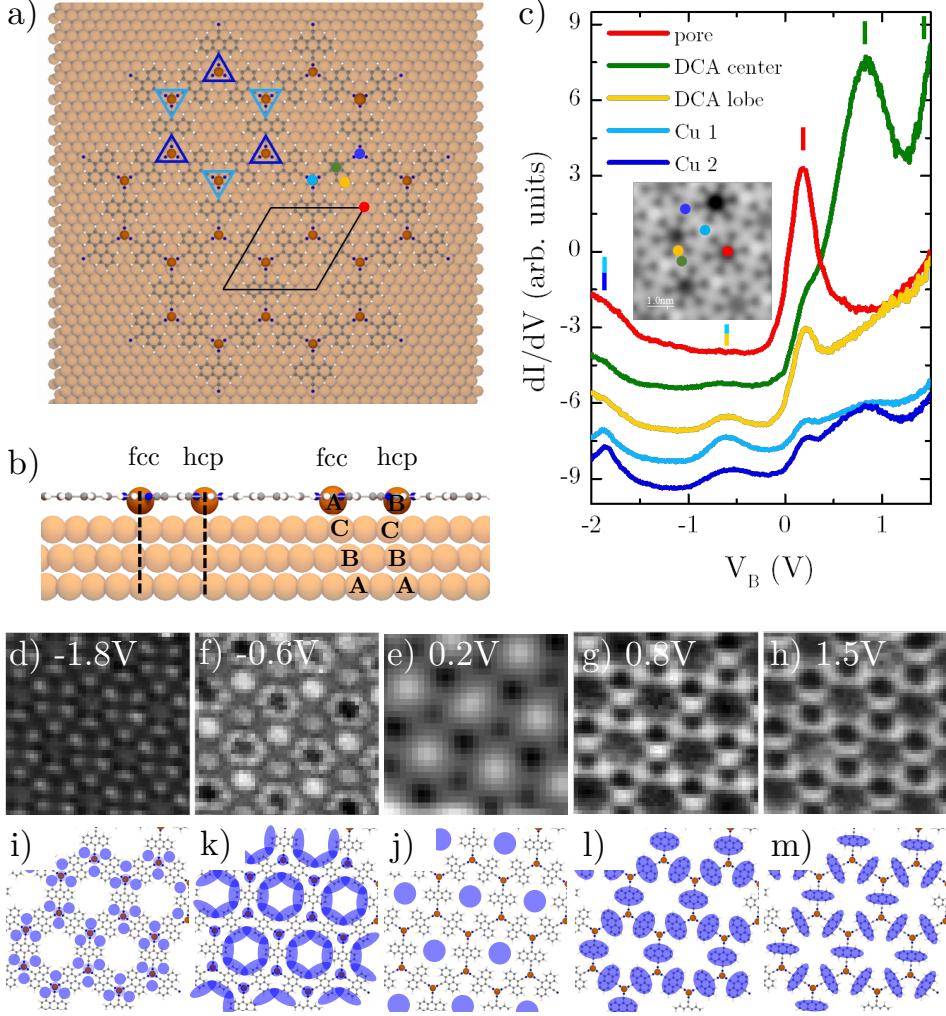


Figure 3.5: Structural and STS characterization of Cu+DCA/Cu(111) network. a) Model of the commensurate 2D-MOF. All coordination atoms are in hollow sites, but occupy alternatively fcc or hcp sites (dark or light blue triangles). A black rhombus indicates the  $(8 \times 8)$  network unit cell. b) Close-up side view of the system. Cu(111) atomic packing is repeated every 3 layers (A-B-C), that show the fcc (A) and hcp (B) adsorption sites of the Cu coordination adatoms. c) STS spectra at the network main characteristic points indicated by color dots at the inset image. The colored vertical ticks above the STS spectra mark the energy positions of the peaks. d)-h)  $dI/dV$  grid maps at the energies highlighted in c) from two different grid measurements. i)-m) Schematics of the states spatial distribution presented in d)-h). STM/STS parameters: c) Inset image:  $I_t = 100$  pA/ $V_B = -1$  V. d, f, g, h) Regulation point  $I_t = 80$  pA/ $V_B = -1$  V;  $V_{rms} = 6.6$  mV,  $f_{osc} = 913$  Hz. e) Regulation point  $I_t = 150$  pA/ $V_B = -1$  V;  $V_{rms} = 9.6$  mV,  $f_{osc} = 817$  Hz.

This peak is present not only at the Cu adatom positions but also at the external anthracene rings of DCA molecules (DCA lobes). In perfect agreement with ARPES, we find that it has a delocalized character and its peakwidth coincides with the observed bandwidth. Notably, we find that there are two electronically different Cu adatoms that alternate in the network. As visualized in the topography inset (cf. inset of Fig. 3.5c) or in Figure 3.1f, the two Cu adatom types exhibit different intensities although they are equally connected to all molecules. We note that the Cu1 adatoms (brighter ones) display a sharper lineshape with stronger intensity at  $-0.6$  V compared to the Cu2, but this situation is reversed in the peak centered at  $\sim -1.8$  V. An electronic band similar to the one at  $-0.6$  eV is also found in ARPES right at this lower energy (cf. Figs. 3.2b and 3.12). We also note that at the LUMO energy ( $\sim 0.8$  V) the intensities are nonequivalent for the two Cu adatom types (cf. Fig. 3.5c).

### 3.1.4 Edge state at the kagome multi-band

After this careful characterization of the electronic structure of our network, the energies around the kagome multi-band emerge as candidates to host the elusive edge states (the OTI fingerprint). To promote the edge states, we reduce the molecular coverage and form large islands with well-defined borders separated by extended pristine Cu regions. We acquired several  $dI/dV$  grids at the 2D-MOF island borders using different tips and preparations with the purpose of its experimental detection. However, as evidenced in Fig. 3.6, the edge state is absent. Note that Fig. 3.13 in the Supplementary material section shows just two of the five grids acquired for this purpose that reproduce identical results. Therefore, it is reasonable to assume that some physical mechanism should be responsible for this edge state absence within the electronically conjugated 2D-MOF.

### 3.1.5 Assessment of possible causes for the edge state absence

The studied MHK lattice shares a common condition with the other experimentally studied networks proposed as OTIs [65–68]: the edge state is undetectable at the island borders. This happens despite this network gathers all essential ingredients to be an OTI: a specific theoretical prediction [55], excellent structural formation, long-range order, proximity of the kagome multi-band to  $E_F$  [85] and negligible amount of defects as judged by LEED, STM and ARPES. Consequently, we may conclude that some underlying physical mechanism, probably related to the substrate presence must disrupt the predicted



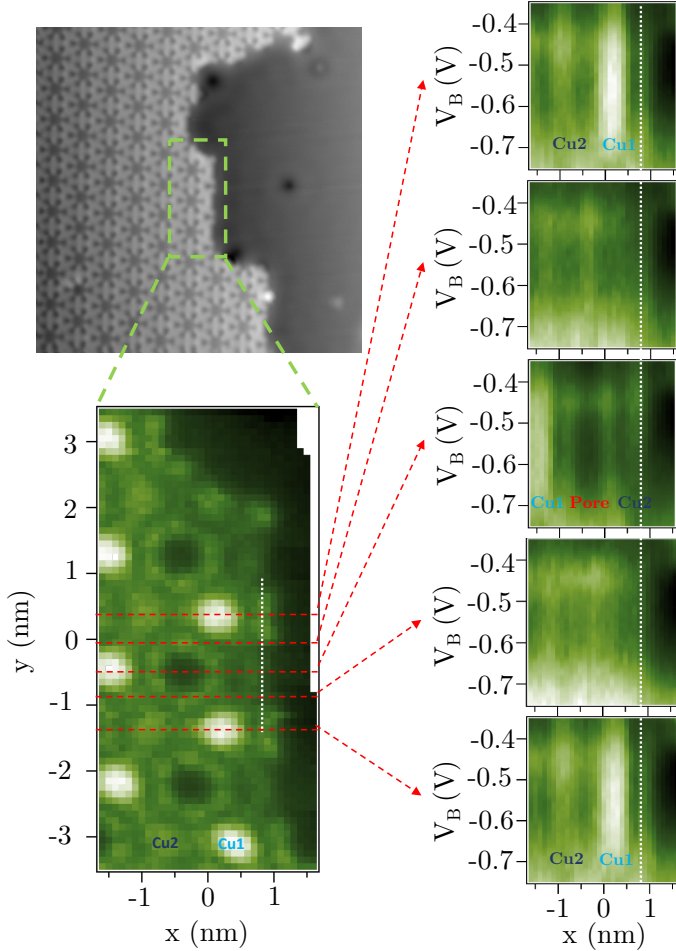


Figure 3.6:  $dI/dV$  map acquired at  $-0.6$  V (bottom left) at the area enclosed by the rectangle in the STM image. Five selected horizontal line scans (right) extracted from a  $dI/dV$  grid in the energy range of the 2D-MOF kagome multi-band. The position of the right  $dI/dV$  green color plots (bright being more intense) are indicated by horizontal discontinuous red lines on the left and the white vertical line is a guide to the eye marking the place where the edge states would be expected. The first and the last horizontal lines are equivalent. STM image parameters:  $I_t = 300$  pA/ $V_B = -1$  V; STS parameters:  $I_t = 300$  pA/ $V_B = -1$  V;  $V_{rms} = 9.6$  mV,  $f_{osc} = 817$  Hz.

topologically protected states in these MHK lattices. A plausible explanation is the closing of the gap due to substrate induced Rashba effect competing with the SOC induced gap [67]. However, the intercalation of decoupling layers does not promote the manifestation of these edge states [65].

Another possibility is the orbital hybridization of the network states with Cu(111) bands. The extended kagome multi-band from the 2D-MOF exhibits the largest spectral weight at the adatoms. From a naive perspective, it could originate from an array of Cu bound states [105], i.e. a locally modified version of the Shockley state in the presence of its own adatoms [106–108]. In this bound state scenario, an antibonding state should also be present above the surface state onset [105], but we do not find it anywhere and therefore must be discarded. Moreover, we do not detect any alteration (or energy shift) of the *sp*-band dispersion and umklapps in ARPES that would be indicative of a significant orbital hybridization between the MHK network and the substrate. Nevertheless, the substrate influence cannot be disregarded since a significant charge transfer occurs that shifts down in energy the calculated free-standing kagome multi-band (cf. Fig. 3.4b,d) [55].

Interestingly, two spectroscopically different coordination adatoms are detected by STS in the network (see Figs. 3.5 and 3.6), which should provide some inner structure into the kagome multi-band. However, such intricate band manifold details cannot be resolved in ARPES neither at the home laboratory setup nor at the synchrotron endstation (cf. Figs. 3.2 and 3.4). The spectroscopic difference between the Cu adatoms could originate from the alternate registry (although still commensurate) with the underlying substrate. Although both types of atoms are on hollow sites, one type are vertically positioned on fcc sites, while the other is on hcp positions (see Fig. 3.5a, b). We expect this structural dissimilarity to be a second order effect that cannot explain by itself the significant electronic variation found in the STS measurements nor the edge state absence.

### 3.1.6 Emergence of symmetry breaking in the 2D-MOF using functionalized tips

We look for an alternative explanation and investigate the network morphology through constant height current maps using a CO-functionalized tip [77, 109] (see Fig. 3.7). These bond-resolved images provide insight into the chemical structure of the 2D-MOF and reveal relative height differences of its organic units with respect to a plane above the surface [110]. The constant height cur-

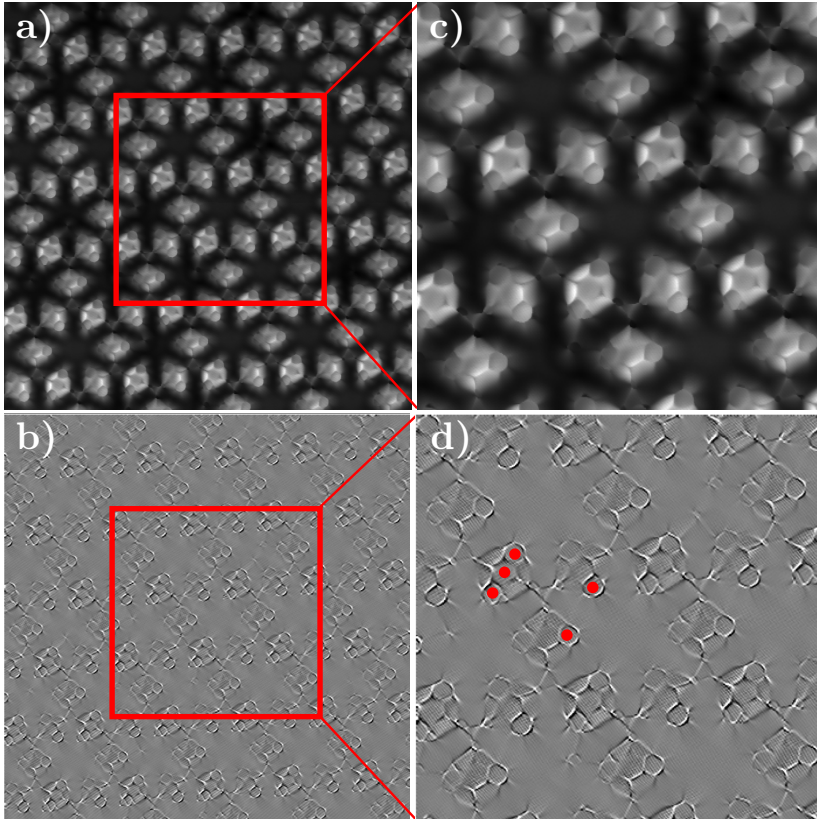


Figure 3.7: Constant-height current maps of Cu+DCA/Cu(111) network. a) and c) are raw data images of  $10 \times 10 \text{ nm}^2$  and  $5 \times 5 \text{ nm}^2$ , respectively. b) and d) show these images after a Laplacian filtering for a proper visualization (differentiated with respect to  $x$  and  $y$  directions). Red dots in d) mark protruding rings around a Cu adatom that is continued by each molecule orientation. All images acquired at  $V_B \approx 0 \text{ mV}$ .

rent maps we acquired are displayed in Figures 3.7a, c, while the same images with a Laplacian filter are presented in Figures 3.7b, d. In Figure 3.7c, one can observe that inside each molecule, not all the benzene rings are visualized equally, which means that these rings are not at the same height with respect to the substrate plane. We discard local electronic contributions when measuring at zero bias since the only relevant state at this energy is the confined surface state, which is isotropic in origin. In other words, observed relative differences must be attributed to morphological alterations of this 2D-MOF. Red dots in Figure 3.7d highlight protruding sections of different molecules. It evidences that some molecules are inclined around their cyano bond axes. We observe that the molecules are periodically tilted revealing a regular non-planar structure made up with three molecular orientations. This is quite unexpected, since the anthracene backbones are all equally positioned with their ring centers on top of surface atoms (see Fig.3.5a). Thus, the observed arrangement is unrelated to substrate-molecule registry differences. Moreover, this is a long-range correlation since the molecular tilting is maintained throughout the extended 2D islands (cf. Fig. 3.7a, b). We also detect that on each molecule the central ring is better defined on the side of one cyano group and blurred on the other side. This means that there is an additional rotation of molecules with respect to their anthracene backbone axes. We can observe that this rotation is also periodic: around alternate Cu adatoms, all cyano groups are the higher or lower side of their molecule. This suggests that Cu adatoms are located alternatively at two different heights, with the same periodicity that they were bright or dark atoms (Cu1 or Cu2) in topography images. In consequence, the spectroscopic differences between alternating Cu adatoms (see Fig. 3.5c) can also be due to their different height with respect to the substrate.

The structurally different molecules and adatom types have a direct impact in the network symmetry: the six-fold symmetry of the 2D MHK lattice becomes utterly upset. Such condition must alter the electron transport within the metal-organic array, which can be qualitatively modeled in the form of different hoppings between adjacent kagome lattice sites using a simple tight binding model. Figure 3.14 in the Supplementary material section shows a complete tight binding calculations study with variation on different parameters, while in Figure 3.8 the most relevant cases are presented. In the latter, the columns represent calculations performed for two different SOC strength to hopping parameter ratios ( $\lambda/t = 0.02$  and  $0.1$ ), while the rows represent variations in the hopping parameters between kagome lattice sites. The first row calculations were performed for uniform hopping parameters ( $t_{AB} = t_{BC} = t_{AC} = t$ ), while in the second,  $\pm 10\%$  differences in the first-neighbor hopping terms are

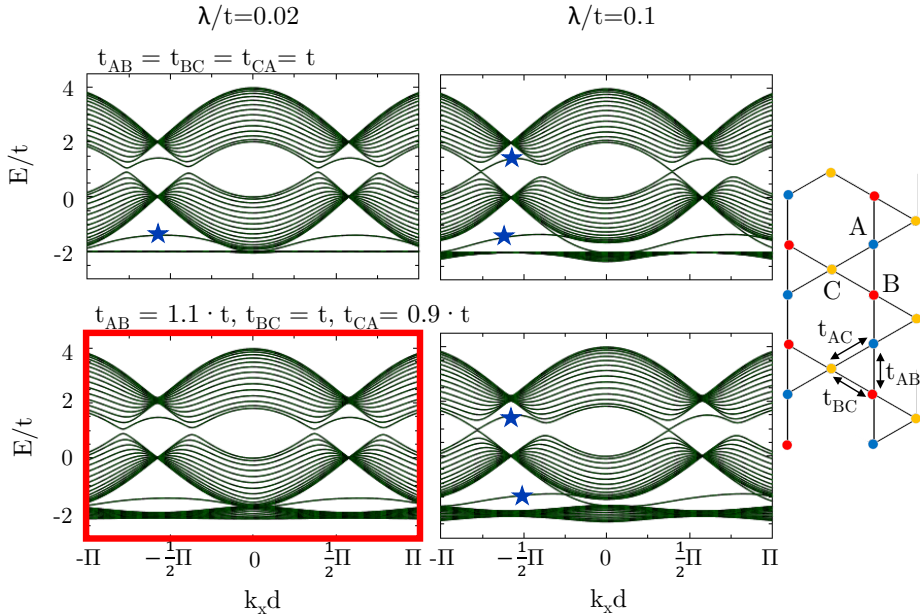


Figure 3.8: First neighbor tight binding models for the kagome lattices projected into the island borders with varying ratio between the spin-orbit strength ( $\lambda$ ) and hopping terms ( $t$ ). Protected edge states are visible always at  $\lambda/t = 0.1$ , as indicated by the dark blue stars. Note that the left column ( $\lambda/t = 0.02$ ) shows the OTI case reported in Ref. [55]. The breaking of the network symmetry is qualitatively emulated here by introducing differences in hopping values (bottom row). Particularly, the red box highlights the case closest to our experimental case, where  $t_{AB} = 1.1t$ ;  $t_{BC} = t$ ;  $t_{CA} = 0.9t$  and  $\lambda/t = 0.02$ , where no edge state develops. At the right side, a sketch of the kagome lattice identifies its lattice sites and hoppings.

introduced. The bands at the top left panel were calculated taking the same parameters of Ref. [55]. We find here, for  $\lambda/t = 0.02$ , a band connecting the Dirac and the flat bands, which is in essence an edge state, according to their calculations. Since we experimentally detected a breaking of the symmetry in the Cu+DCA/Cu(111) network (Fig. 3.7), our case would be one at the bottom left. In this case, the tiny gaps are closed and so the system cannot host topological states anymore. Nevertheless, the second column calculations demonstrate that these topologically protected edge states could be preserved in a hypothetical lattice with a high enough SOC ( $\lambda/t = 0.1$ ) despite this symmetry breaking. In essence, our toy model qualitatively demonstrates that for MHK lattices with limited SOC the symmetry breaking avoids the formation of the edge states, thereby disrupting their OTI condition [111].

Unlike this studied network, the free-standing 2D-MOFs theoretically proposed always preserve some mirror and inversion symmetries that lead to preservation of their topological properties, despite being buckled or twisted [53, 112, 113] or in different forms and shapes [114, 115]. We stress that total absence of symmetry does not “per se” lead to closing of the multi-band gaps since our toy model calculations shows that topological conditions are still reachable by increasing the  $\lambda/t$  ratio in reduced symmetry scenarios (see Fig. 3.8). However, the experimental recurrent absence of edge states in theoretically proposed OTIs studied so far suggests that the 2D-MOFs could favor structural alterations capable of closing these tiny gaps (of the order of several mV, see Fig. 3.4e). Indeed, a dicyanobiphenyl + Co network grown over graphene presents long-range ordered alternate phenyl rotations [65], while other MHK lattices show tiny morphological distortions [116] that break any existing mirror symmetry. In essence, such spontaneous symmetry breaking must relate to a subtle correlation between the morphology and the system’s electronic energy. In our case, the morphological difference of the Cu adatoms positions (fcc vs hcp) with respect to the substrate introduces a very small energy imbalance that must affect the metal coordination with their neighbouring cyano groups. This is apparently not enough by itself to lift the topological protection, but triggers the molecular tilting that further affects the system’s equilibrium. In consequence, the 2D-MOF kagome multi-band splits in energy, which closes the mini-gaps of the OTI. We infer that this small symmetry alterations are enough to remove the edge states. Closing the very small band gaps of OTIs could reduce the energy cost required to maintain the topological protection of the edge states upon the substrate presence. In essence, this collective symmetry breaking reminds of Jahn-Teller [117] and pseudo Jahn-Teller distortions [118] that are very efficient mechanisms to lift the system’s degeneracies that compete with other electronic interactions [119–121].

## 3.2 Conclusions

In summary, we have formed a long-range ordered MHK lattice (2D-MOF) predicted to be an OTI. We experimentally identify its expected kagome multi-band both by ARPES and STS, which validates the MHK lattice overall electronic conjugation. Despite the excellent growth and precise morphology that display a perfect registry (commensuration) with the underlying substrate, the edge states are absent. Although substrate related mechanisms like hybridization and/or SOC lifting cannot be totally discarded, we find that the network is unexpectedly non-planar and the molecules are tilted with respect to the sur-

face plane. These morphological alterations (that encompass the Cu adatoms forming a honeycomb lattice) suggest that breaking the overall mirror symmetry of the network leads to a more stable condition. This could efficiently close the tiny gaps of the 2D-MOF kagome multi-band and promote the edge state absence. This symmetry breaking mechanism might extend to other MHK lattices and explain the recurrent experimental absence of their edge states. However, the challenge of experimentally achieving an OTI system remains. Expanding the kagome multi-band gaps in MHK lattices using massive coordination atoms such as Bi [53] might yield materials with the sought non-trivial properties. The established network conjugation and highly crystalline structure observed in our 2D-MOF ensures the feasibility for building robust organic-based materials with well-defined topological properties imposed by their lattice [94]. These are essential requirements to develop new electronic and photonic applications capable of operating with stability and robustness up to RT.

### 3.3 Supplementary material for Chapter 3

In this section, some supplementary Figures mentioned along the main text of Chapter 3 are presented.

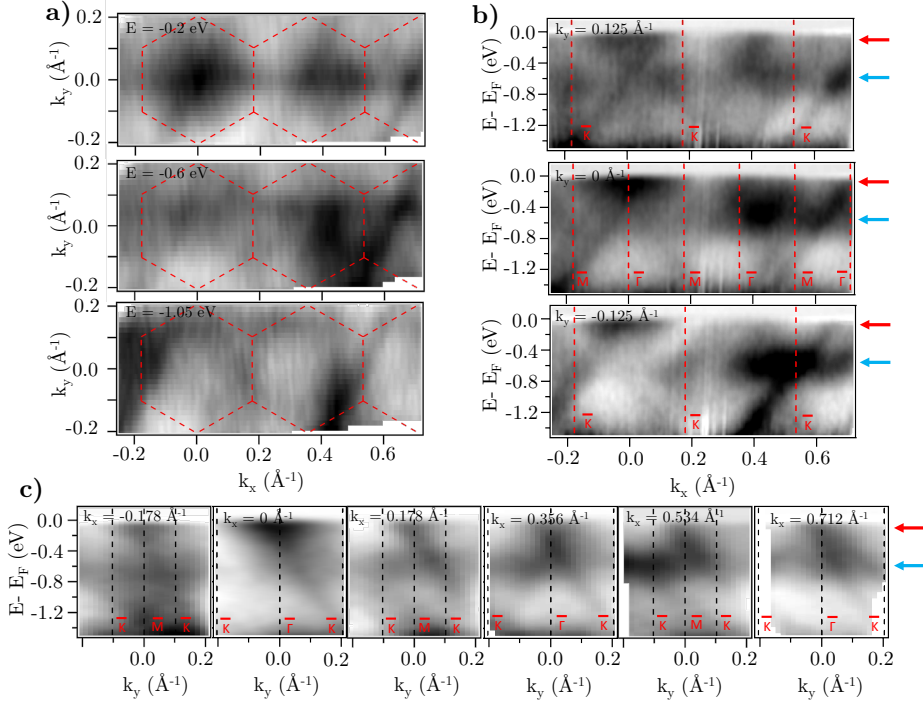


Figure 3.9: Direct ARPES signal of a saturated surface of the Cu+DCA/Cu(111) network in a synchrotron. a) Three different isoenergetic cuts at the energies indicated within each panel. The dotted hexagons indicate the repeated Brillouin zones. b) Band structure parallel to the  $\overline{\Gamma M}$  direction at selected  $k_y$ . c) Band structure cuts parallel to  $\overline{\Gamma K}$  (perpendicular to b) at the  $k_y$  values containing the high symmetry points. The colored side arrows indicate the network features discussed in the main text. ARPES details: Linear grayscale where darker corresponds to higher intensities.  $h\nu = 18$  eV;  $T_S = 100$  K



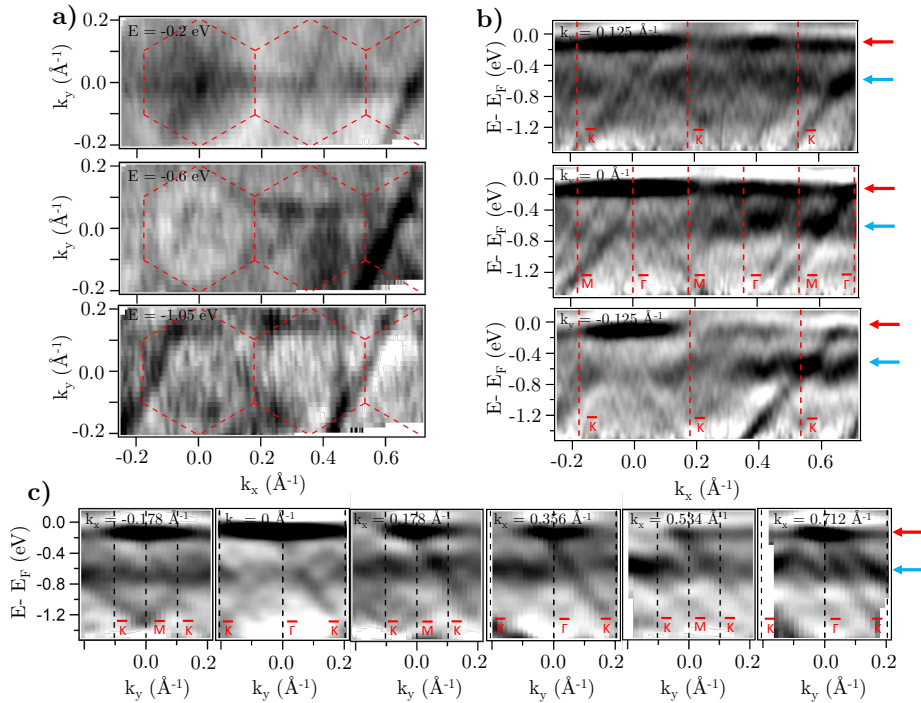


Figure 3.10: Same as Figure 3.9 but showing the  $2^{nd}$  derivative of the direct ARPES signal. The presence of the bulk  $sp$ -band umklapps hinders from a proper visualization of the network bands. Darker parts correspond to higher intensities

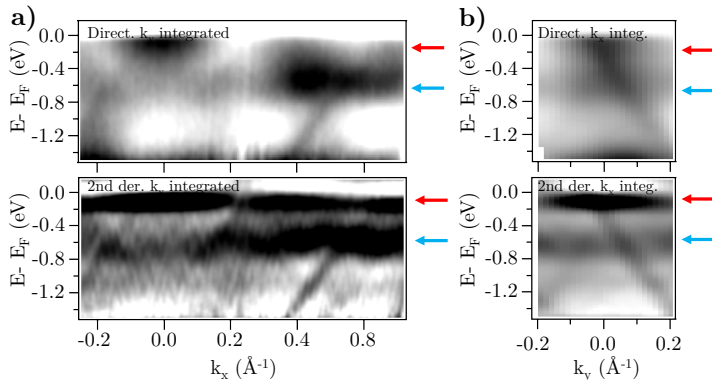


Figure 3.11: Direct (top row) and  $2^{nd}$  derivative (bottom row) ARPES signal integrated along the  $\overline{\Gamma M}$  (left column) and  $\overline{\Gamma K}$  (right column) directions. The data clearly shows the broad network state at  $-0.6$  eV. In the linear grayscale, darker corresponds to higher intensities. ARPES parameters:  $\hbar\nu = 18$  eV;  $T_S = 100$  K.

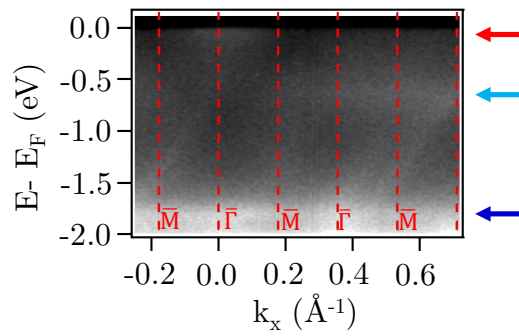


Figure 3.12: Direct ARPES signal along the  $\bar{\Gamma}\bar{M}$  direction for a larger energy range. The grayscale (brighter corresponds to a more intense signal) shows three features indicated by the arrows that matches the STS peaks. Photon energy used  $h\nu = 22$  eV;  $T_S = 100$  K.

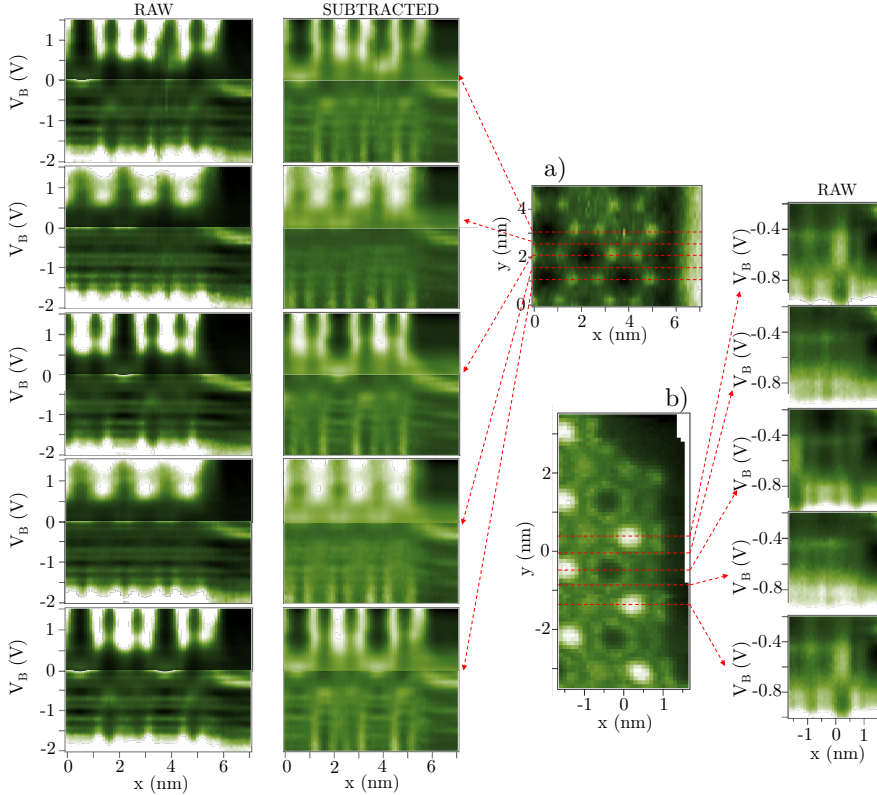


Figure 3.13:  $dI/dV$  colorplots showing that no edge state develops. Data were extracted from two different  $dI/dV$  grids at two different island terminations.  $dI/dV$  maps of these regions are presented on the center and labelled as a) and b). On the side, five horizontal line scans are selected from each grid, resulting in the  $dI/dV$  green colorplots (bright being more intense) as a function of position and bias. Note that in both panels, the first and the last horizontal lines are equivalent. In panel a), the intensity scale of the  $dI/dV$  colorplots are independent for positive and negative  $V_B$  for better visualization. Intense tip states are detected in the occupied region (horizontal streaks), so the right column shows the data after subtraction at each grid point of an integrated  $dI/dV$  spectrum. With this subtraction, we visualize better the different features and reduce the tip state contribution. STS parameters: a) Setpoint:  $I_t = 140$  pA/ $V_B = -1$  V;  $V_{rms} = 6.6$  mV,  $f_{osc} = 913$  Hz; voltage range  $[-2$  V,  $1.5$  V]. b) Setpoint:  $I_t = 300$  pA/ $V_B = -1$  V;  $V_{rms} = 9.6$  mV,  $f_{osc} = 817$  Hz; voltage range  $[-1$  V,  $-0.2$  V].

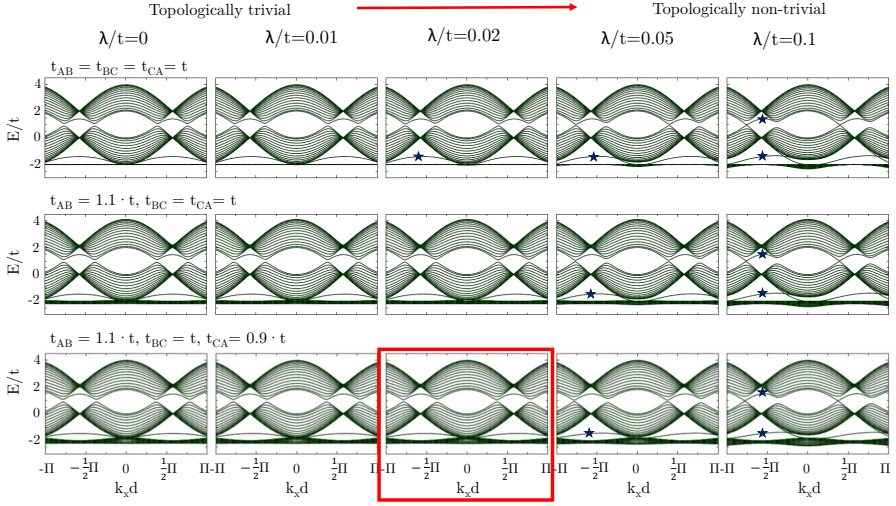


Figure 3.14: First neighbor tight binding models for the kagome lattices projected into the island border with varying ratio between the spin-orbit strength ( $\lambda$ ) and hopping terms ( $t$ ). The topologically trivial case always occurs for  $\lambda/t = 0$ , whereas the non-trivial topology of the kagome is displaced towards larger ratios. Indeed, protected edge states are visible always at  $\lambda/t = 0.1$ , as indicated by the dark blue stars. Note that the middle column ( $\lambda/t = 0.02$ ) shows the case reported in Ref. [55]. The breaking of the network symmetry is qualitatively emulated here by introducing differences in the hopping values. Particularly, the red box highlights the case closest to our experimental case, with  $t_{AB} = 1.1t$ ,  $t_{BC} = t$ ,  $t_{AC} = 0.9t$  and  $\lambda/t = 0.02$ , where the mini-gaps are closed and no edge state develops.

## Chapter 4

# Role of the coordination atom and substrate in the electronic properties of DCA-based networks

Several free-standing MHK networks have been theoretically predicted to be OTIs. However, their realization requires the presence of substrates as support of these networks. Substrate-molecule and molecule-metal contacts can drastically affect the electronic properties of such ultrathin organic films [52, 104, 122–124]. In the previous chapter we demonstrated that the substrate presence can change significantly the free-standing electronic structure leading to the absence of edge states. Furthermore, the interaction with the Cu(111) promotes a noticeable charge transfer.

In this chapter, we form 7 variations of the previous Cu+DCA MHK lattice, by combining different coordination atoms and substrates. We expect to tune the MHK lattice interaction with the substrate to drastically limit the influence of the interface and discard it as the cause of the symmetry breaking observed in Chapter 3. For this, we use Ag(111), Au(111) and Bi<sub>2</sub>Te<sub>3</sub> as substrates, since a weaker interaction between the MHK network and the substrate is expected in these cases than with Cu(111). The fact that the molecules do not spontaneously form the metal-organic network on these alternative substrates uptaking their adatoms at RT allows to generate these MHK lattices with selected *3d* atoms. Since the role of coordination atoms forming a honeycomb sublattice is to provide SOC while maintaining the network stability, we use

elements with similar atomic radius. These networks will be denoted hereafter as M+DCA, where M=Cu, Fe, Co. With the electronic information obtained on Cu+DCA/Cu(111), we study and compare the new MHK networks' topography and electronic properties using STM and STS as experimental tools. We observe that in spite of an important substrate decoupling, no edge state is ever revealed, possibly related to the strong structural symmetry breaking that is always found, independently of the adatom-substrate interaction. We will show that M+DCA/Au(111) networks appear as highly decoupled, comparatively as much as Co+DCA/Bi<sub>2</sub>Te<sub>3</sub>, where a weak substrate-network interaction is expected, due to the scarce surface DOS.

In the following, we present a detailed and systematic study of all the systems. As it will be shown, they present noticeable similarities. In the Discussion section we will compare all these systems, including Cu+DCA/Cu(111) that was studied in Chapter 3.

## 4.1 Results

### 4.1.1 DCA assembly on Ag(111) and Au(111) substrates without metal coordination

With the purpose of forming MHK lattices on less interacting substrates, we first evaporate DCA molecules on Ag(111) and Au(111) substrates at RT and check the resulting structures. In both cases, the molecules adsorb in a planar configuration, with their anthracene backbones parallel to the substrate. The molecules self assemble forming large compact islands, as shown in Figure 4.1a, b. The cyano groups of each DCA point to H atoms of other molecules, so we identify hydrogen bond as the main mechanism driving this self-assembly. With such DCA configuration, we confirm that Ag and Au adatoms do not participate in these island assembled on Ag(111) and Au(111) substrates at RT, unlike the case of Cu(111) studied in Chapter 3. The arrangement found is a rectangular oblique phase with vectors (obtained from the STM images)  $|\vec{a}_1| = 1.18$  nm and  $|\vec{a}_2| = 0.93$  nm forming an angle of  $52^\circ$  to each other in the case of Au(111) and  $|\vec{a}_1| = 1.14$  nm and  $|\vec{a}_2| = 0.97$  nm forming an angle of  $50^\circ$  on Ag(111). According to our LEED measurements (see Figs. 4.14 and 4.15 in the Supplementary material section) both phases appear to be identical, suggesting that the tiny differences detected by STM are in the limit of its accuracy. On each substrate, we observe three different molecular domains that follow the symmetry directions of the underlying substrate.

Note that very irregular patches of Au+DCA/Au(111) where the molecules coordinate with Au adatoms from the substrate have been reported when keeping the substrate at  $\sim 200$  K during DCA deposition [65]. However, at RT we find an absence of spontaneous formation of DCA-Au bond that allows us to use both substrates to form MHK lattices with selected coordination atoms, as will be presented later.

Before that, we obtained the electronic structure of compact DCA molecular arrays by STS. We present these electronic structures through STS spectra taken at three representative points (see Fig. 4.1c, d): the DCA center, the DCA lobe and the substrate reference. In the case of Ag(111), both molecular spectra have a step-like feature at  $\sim 0.1$  V. Also, we observe a peak at  $\sim 0.4$  V at the DCA lobe. In the molecular assembly formed on Au(111), the molecular spectra present also a step-like feature at  $\sim -0.35$  V. We assigned the LUMO to the peak observed at  $\sim 1.4$  V, although the complete feature is not fully contained in the measured energy range. Another peak distributed uniformly along the molecule at  $\sim -1.1$  V is assigned to be the HOMO, resulting in a gap of  $\sim 2.5$  V.

We find that the presence of the molecular islands does not destroy the step-like feature stemming from the surface states. Instead, it is upshifted by  $\sim 150$  mV on both substrates, which defines it as an interface state, characteristic of weakly interacting overlayers [125–127]. This state is absent in a similar uncoordinated assembly formed on Cu(111) [97], already suggesting a stronger interaction of DCA with this substrate that quenches the surface state. Contrarily, the molecular states at the unoccupied part, assigned to be their LUMO states, appear with different intensities and at different energies on each metallic substrate [66, 125]. The LUMO formed on Au(111) is much more intense compared with the substrate surface state than in the case of the same assembly formed on Ag(111). Also, their energy differs by  $\sim 1$  V [ $\sim 0.4$  V on Ag(111) and  $\sim 1.4$  V on Au(111) substrate]. We find that similar DCA arrays on insulating substrates [NaCl/Cu(111) and gr/Ir(111)] have their LUMO at  $\sim 1.1$  V and  $\sim 1.8$  V, respectively [65, 104]. Such findings suggest that DCA molecules interact more weakly with Au(111) than with Ag(111), since in the former less charge transfer occurs and the LUMO is energetically further away from  $E_F$ , while in Ag(111) the LUMO is closer to be occupied.

The observed modulation in the molecule-substrate interaction allows us to investigate the nature of symmetry breaking observed in Cu+DCA/Cu(111) network and find out whether it is primarily induced by a strong coupling with the substrate. Note that in the case of the Cu(111) substrate, we cannot

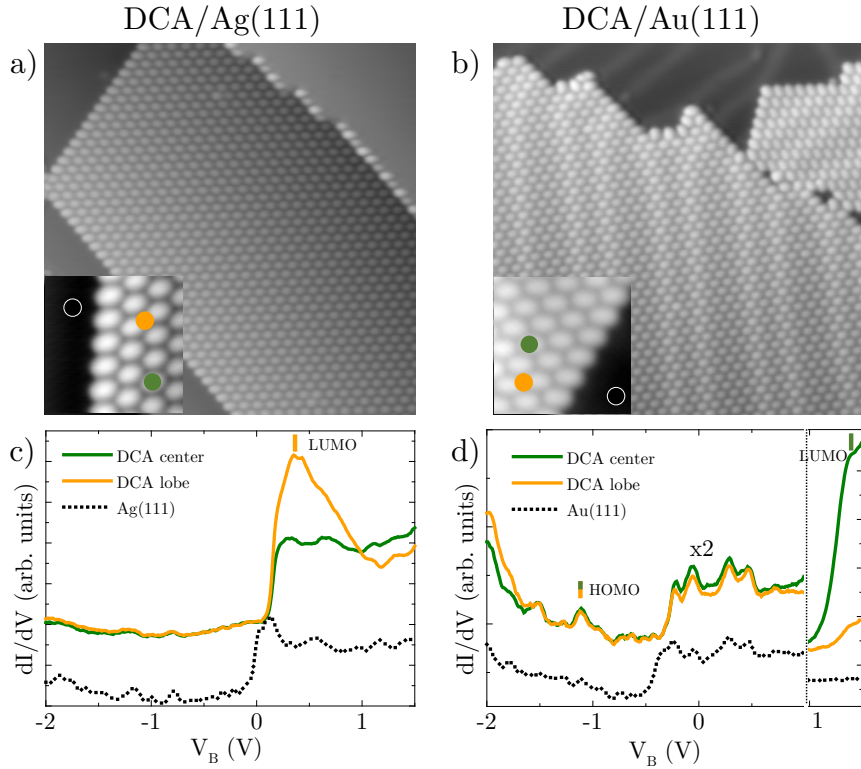


Figure 4.1: Topography and electronic characterization of DCA molecules on Ag(111) and Au(111). a), b) STM overviews of DCA molecules self assembled on Ag(111) and Au(111), respectively. Inset images showing the point spectroscopy positions. Note that the herringbone reconstruction is unaffected upon molecular presence. c), d) Electronic characterization by STS, where the HOMO and LUMO positions are indicated on the STS spectra. Curves in d) present different scaling above and below  $V_B = 1$  V to properly visualize the HOMO and the interface state. STM/STS parameters: a), b)  $30 \times 30$  nm<sup>2</sup>,  $I_t = 100$  pA/ $V_B = -1$  V; inset images  $5 \times 5$  nm<sup>2</sup>,  $I_t = 100$  pA/ $V_B = -1$  V. STS parameters:  $I_t = 100$  pA/ $V_B = -1$  V;  $V_{rms} = 9.6$  mV,  $f_{osc} = 817$  Hz.



form the network with other coordination atoms, since Cu adatoms available at RT bond spontaneously to the molecules. Overall, we present 7 analogous 2D-MOFs, so a detailed description will be given for the first system presented on each substrate, whereas the rest will just mention the key points.

#### 4.1.2 MHK lattices on Ag(111)

The M+DCA/Ag(111) networks (where M=Cu, Fe, Co) are generated by the evaporation of DCA molecules followed by subsequent evaporation of the coordination metal on a Ag(111) substrate at RT. After this, an annealing of 20' at  $\sim 100^\circ\text{C}$  is performed to improve the islands size and order. In Figures 4.2, 4.3 and 4.4 STM topographies and electronic characterization by STS are presented for M+DCA/Ag(111) networks coordinated with Cu, Fe and Co, respectively. Their arrangement is the same as the one observed in Cu+DCA/Cu(111): the kagome sublattice formed by the DCA centers is interwoven with the honeycomb sublattice formed by the coordination atoms. However, their lattice parameters calculated as the pore-pore distance is 1.98 nm, which is slightly compressed with respect to the Cu+DCA/Cu(111) case. Unlike the Cu+DCA/Cu(111) network, M+DCA/Ag(111) are not commensurate with the substrate, and also form different domains, as deduced by the LEED patterns presented in Figure 4.14 in the Supplementary material section. Two main equivalent domains are generated at  $30 \pm 16^\circ$  with respect to the substrate high symmetry directions. Also, a minority domain is formed at  $30^\circ$  with respect to the substrate. Note that despite local disturbances, each network island observed with the STM appears as monodomain and quite extended.

#### Cu+DCA/Ag(111)

The topography and electronic structure of the Cu+DCA/Ag(111) network is presented in Figure 4.2. As shown, large network islands are formed with a very low quantity of defects after the annealing process. DCA molecules at the island borders are slanted in the plane, probably due to the lack of commensuration with the substrate. In Figure 4.2c, d, bond-resolved images of the network exhibit that not all the rings of the anthracene backbone are at the same height, thereby vertically disrupting the structural symmetry. We expect this to lead to the quenching of the edge states characteristic of OTIs following our findings in Chapter 3.

The electronic characterization is performed by means of  $dI/dV$  grids and STS acquired at the characteristic points of the network and the substrate for

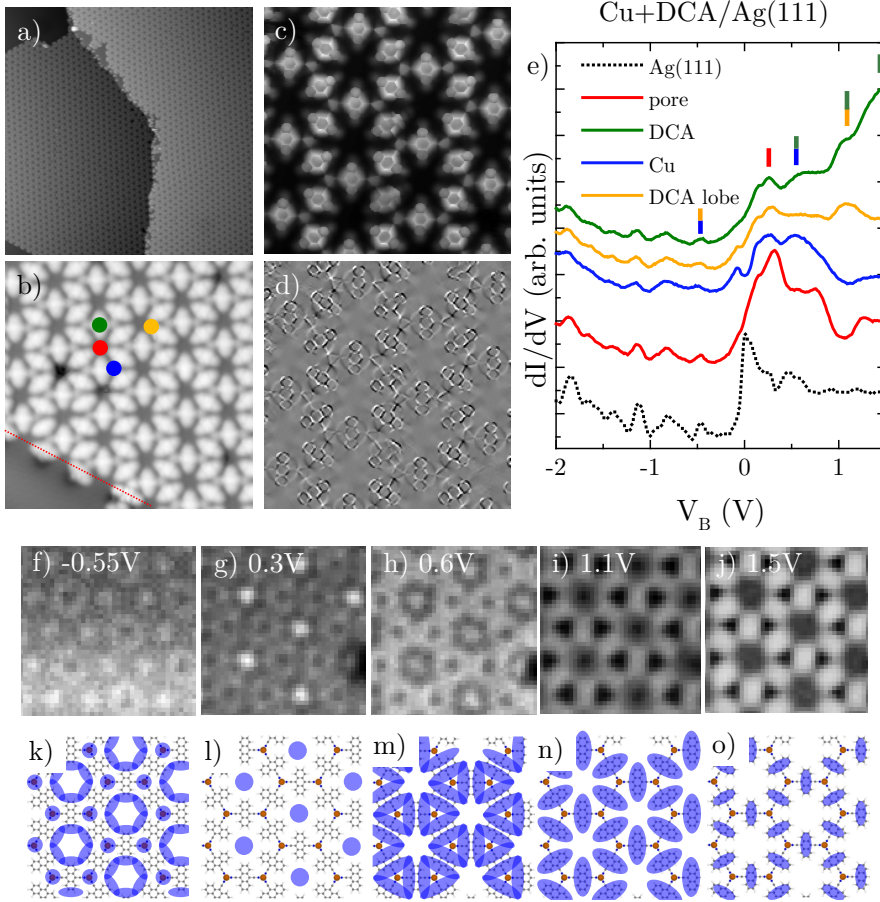


Figure 4.2: Structural and electronic characterization of Cu+DCA/Ag(111) network. a) Overview of the long range ordered network. b) Close up to a network island edge. c) Constant height current image with the tip functionalized with a CO molecule (raw data). d) Same as in c with a Laplacian filter. e) STS spectra taken at the network positions extracted from a  $dI/dV$  grid. The ticks' colour indicate the network position where relevant intensity is detected at each marked energy. f)-j)  $dI/dV$  grid maps at the energies highlighted in e. k)-o) Schematics of the states spatial distribution presented in f-j. STM/STS measurements parameters: a)  $75 \times 75 \text{ nm}^2$ ,  $I_t = 100 \text{ pA}/V_B = -1 \text{ V}$ ; b)  $10 \times 10 \text{ nm}^2$ ,  $I_t = 20 \text{ pA}/V_B = 10 \text{ mV}$ ; e) Regulation point:  $I_t = 100 \text{ pA}/V_B = -1\text{V}$ ;  $V_{rms} = 9.6 \text{ mV}$ ,  $f_{osc} = 817 \text{ Hz}$ ; f)-j)  $5 \times 5 \text{ nm}^2$ ,  $V_B$  in the images.

reference, and is presented in Figure 4.2e. Since we found that all the studied M+DCA/Ag(111) systems have similar electronic structures, we are describing this one in detail, while the other two will be more concise to avoid repetitions. From lower to higher bias, we identify the following signatures, whose spatial distribution is represented in Figure 4.2f-j: i) A state at  $\sim -0.55$  V located mainly at the DCA lobes and Cu adatoms. This state is similar to the one attributed on the multi-band manifold in Cu+DCA/Cu(111) (see Fig. 4.2f, k). It will be named hereon *multi-band state*. ii) A broad feature peaking at  $\sim 0.3$  V with a bandwidth of  $\sim 0.6$  V mainly located at the pores but with contribution in all the characteristic points (see Fig. 4.2g, l). We attribute this state to the confinement of the Ag(111) surface states in the network pores and will be denoted hereafter as *pore state*. Its bandwidth and its presence in the rest of the network positions supports the delocalization expected from a partially confined surface state band. iii) A peak at  $\sim 0.6$  V in the STS mainly localized at the Cu coordination atoms and at the molecule center. However, its spatial distribution (see Fig. 4.2h, m) suggests that this is mainly a molecular state, and that the intensity observed in the Cu atom spectrum is contributed by the surrounding molecules. This state will be named hereon *cyano state*. iv) A molecular peak at  $\sim 1.1$  V which is mainly located at the DCA center and its lobes (*anthracene broad state*). v) An onset at the molecular center at  $\sim 1.5$  V extending further away from our energy range, that is presumably a prominent molecular state (*anthracene slim state*).

### Fe+DCA/Ag(111)

When using Fe as coordination atom [Fe+DCA/Ag(111) system], similar topography and electronic structure are found, as shown in Figure 4.3. The network arrangement forms large monodomain islands with almost no defects. Looking in detail to the close-up topography image (see Fig. 4.3c), one can observe that some of the molecule anthracene backbones are slightly rotated with respect to the out-of-plane axis. These rotations induce mirror and inversion symmetry breaking that are apparently sufficient to close the tiny gaps required for the OTI, as no protected edge state was detected.

The Fe+DCA/Ag(111) electronic structure is presented in Figure 4.3d-n. In panel d the spectra at the characteristic points are shown while in panels e-i their spatial distribution is presented. Following the same increasing voltage order than in the previous system we observe similar states (5) with slight differences in bias: i) The *multi-band state* located at the Fe atoms and at the molecular lobes as in the previous system, but in this case it is at  $\sim -0.25$  V.

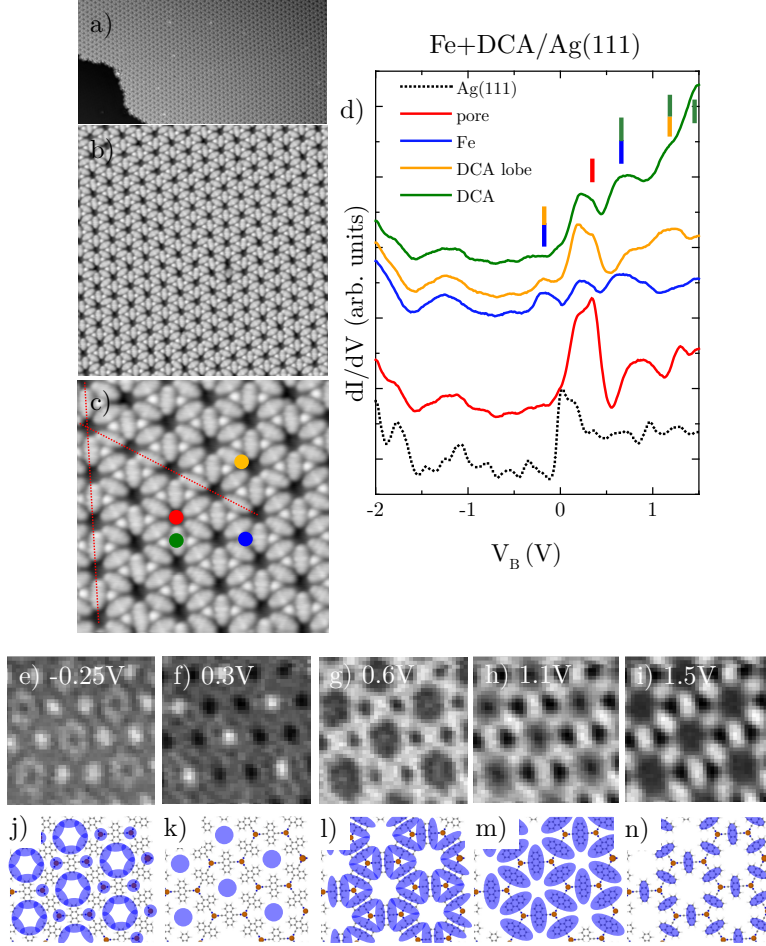


Figure 4.3: Structural and electronic characterization of the Fe+DCA/Ag(111) system. a) and b) correspond to large overviews and c) represents a network close-up. In d) the electronic structure is described through STS spectra at the characteristic network positions extracted from a  $dI/dV$  grid. The ticks' colour indicate the network positions where relevant intensity is detected at each marked energy. e)-i)  $dI/dV$  grid maps at the energies highlighted in d). j)-n) Schematics of the states spatial distribution presented in e)-i). STS/STM parameters: a)  $50 \times 100 \text{ nm}^2$ ,  $I_t = 100 \text{ pA}/V_B = -1 \text{ V}$ ; b)  $25 \times 25 \text{ nm}^2$ ,  $I_t = 100 \text{ pA}/V_B = -100 \text{ mV}$ ; c)  $10 \times 10 \text{ nm}^2$ ,  $I_t = 200 \text{ pA}/V_B = -100 \text{ mV}$ ; d) Regulation point:  $I_t = 100 \text{ pA}/V_B = -1 \text{ V}$ ;  $V_{mod} = 15.8 \text{ mV}$ ,  $f_{osc} = 817 \text{ Hz}$ ; e)-i)  $5 \times 5 \text{ nm}^2$ ,  $V_B$  in the images.

ii) The *pore state* with its maximum peak at  $\sim 0.3$  V and a bandwidth of  $\sim 0.45$  V. iii) The *cyano state* located at the DCA sides and with contribution to the Fe adatoms coming from the surrounding molecules at  $\sim 0.6$  V. iv) The *anthracene broad state*, located at DCA lobes and center at  $\sim 1.1$  V. v) The *anthracene slim state* located at the DCA center at  $\sim 1.5$  V or above.

### Co+DCA/Ag(111)

Finally, we describe the Co+DCA/Ag(111) system, whose main characteristics are presented in Figure 4.4. Bond-resolved imaging of this system (see Fig. 4.4c, d) shows in this case that the central ring of each molecular anthracene is higher than the other two, which indicates an arching of the molecules. Its electronic structure is shown in Figure 4.4e-o and presents very similar features compared with the previous two networks formed on Ag(111): i) The *multi-band state* is here weakly observed at  $\sim -0.43$  V. ii) The *pore state* with its maximum intensity at  $\sim 0.3$  V and with a bandwidth of  $\sim 0.5$  V. iii) The *cyano state* at 0.6 V is located at the external parts of DCA. iv) The *anthracene broad state* distributed along all the molecule is present, although with a weak intensity, at  $\sim 1.1$  V. v) The *anthracene slim state* is observed at  $\sim 1.5$  V.

Interestingly, this network has been recently reported to present Kondo screening at the Ag(111) [69]. The peak reported is close to zero bias. However, we did not detect with clarity this peak since we used a too high modulation voltage ( $V_{mod} = 15.6$  mV) in our  $dI/dV$  grid acquisition and a large energy step of 10 mV. Such bias oscillation and coarse energy step will wash out this sharp peak, hiding it in the large bias window we probed.

In summary, M+DCA/Ag(111) networks are characterized structurally and found to be slightly deformed. The central ring of DCA molecules is more prominent than the other two, which happens due to molecular arching. Also, some of the molecules are slanted, specially at the island borders. Electronically, all the three systems are very similar to each other and also to the Cu+DCA/Cu(111) network, as they present the same states at close energies. First, in the occupied region the *multi-band state*, located in adatoms and DCA lobes is detected. Its energy is slightly different depending on the coordination atom ( $-0.55$  V on Cu,  $-0.43$  V on Co and  $-0.25$  V on Fe). The second is the *pore state* that stems from the SS and peaks at  $\sim 0.3$  V. In the unoccupied part, we find three different molecular states in all the networks formed on Ag(111) at the same energies: the *cyano state* at  $\sim 0.6$ , the *anthracene broad state* at  $\sim 1.1$  and the *anthracene slim state* at  $\sim 1.5$  V or higher. The

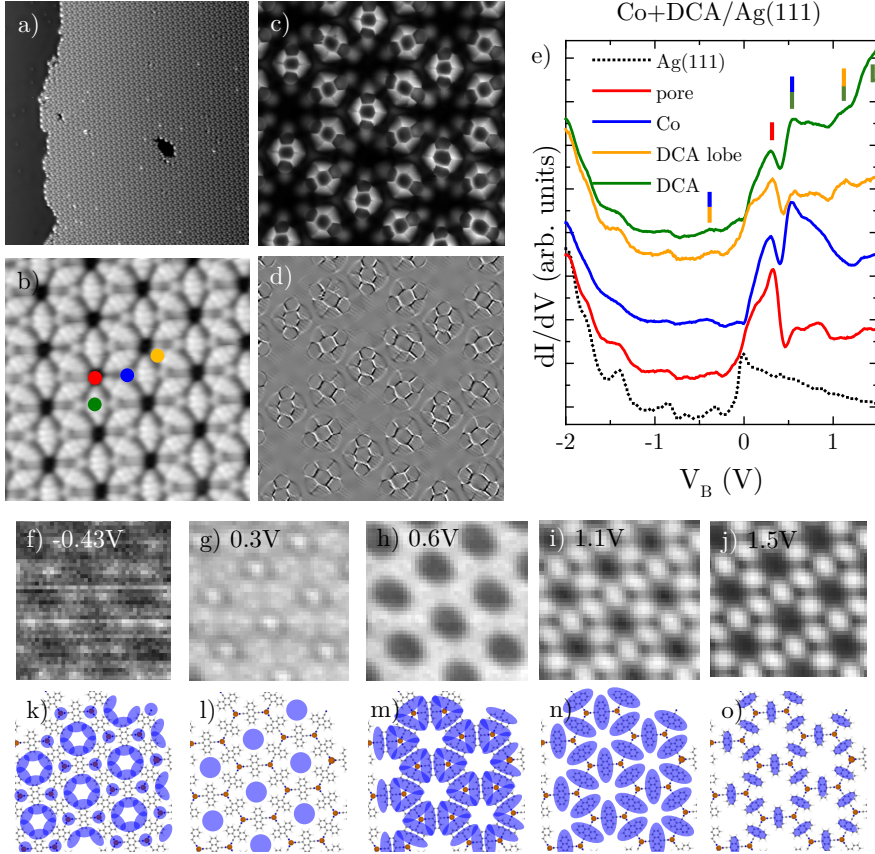


Figure 4.4: Structural and electronic characterization of the Co+DCA/Ag(111) system. a) and b) show an overview and a close-up topography images of this network. c) is a constant height current map with the tip functionalized with CO to get bond-resolution. d) is the same with a Laplacian filter. e) The main STS spectra obtained from a  $dI/dV$  grid. The ticks' colour indicate the network positions where relevant intensity is detected at each marked energy. f)-j)  $dI/dV$  grid maps at the energies highlighted in e). k)-o) Schematics of the states spatial distribution presented in f)-j). STS/STM parameters: a)  $75 \times 75 \text{ nm}^2$ ,  $I_t = 100 \text{ pA}/V_B = -1 \text{ V}$ ; b)  $8 \times 8 \text{ nm}^2$ ,  $I_t = 100 \text{ pA}/V_B = -1 \text{ V}$ ; e) Regulation point:  $I_t = 100 \text{ pA}/V_B = -1 \text{ V}$ ;  $V_{rms} = 15.6 \text{ mV}$ ,  $f_{osc} = 817 \text{ Hz}$ ; f)-j)  $5 \times 5 \text{ nm}^2$ ,  $V_B$  in the images.

*cyano state* is mainly located at the external atoms (H and CN groups) of the molecule. The *anthracene broad state* is observed at the molecule center and its lobes and finally, the *anthracene slim state* is centered at the backbone.

### 4.1.3 MHK lattices on Au(111)

M+DCA/Au(111) networks are prepared following the same protocol as for the M+DCA/Ag(111) network formation: sequential DCA molecules and coordination metal evaporation on the clean Au(111) substrate kept at RT. After this, a soft annealing improves the order and reduces the quantity of defects. We have observed that better order is achieved when the sample is annealed at slightly lower temperatures than in the case of Ag(111), specially when the coordination metal is Cu. Such networks are presented in Figures 4.5 to 4.7, together with their electronic characterization. Their lattice parameter has been calculated from STM to be 1.96 nm, slightly compressed with respect to the previously studied M+DCA networks on Cu(111) or Ag(111). Network islands turn out to be a single domain on this surface when coordinated with Co or Fe (see Fig. 4.15 in the Supplementary material section), which are rotated by an angle of  $30^\circ$  with respect to the Au(111) high symmetry directions. However, Cu+DCA/Au(111) network forms different domains. It is important to stress that these networks do not destroy the herringbone reconstruction, suggesting a weak surface-network interaction.

#### Cu+DCA/Au(111)

Figure 4.5 shows a representative topographic and electronic characterization of Cu+DCA/Au(111) samples. Unlike other DCA-based MOFs, in this case, during the MHK network formation we find the usual structure, but also others with larger pores, that form due to some hydrogen bond interactions between DCA molecules (see Fig. 4.13 in the Supplementary material section). However, these regions can be reduced by decreasing the annealing temperature until most of the surface is covered with the usual MHK network. Constant height current maps using CO terminated tips at zero bias are presented in Figure 4.5c, d and show mainly the anthracene backbone, while the cyano groups of DCA molecules and even the coordination atoms are practically invisible. Moreover, we observe that the DCA backbones are in different heights following the corrugation of the Au(111) herringbone below the network.

The network electronic properties have been studied by acquiring  $dI/dV$  grids from which STS were extracted and presented in Figure 4.5e. The elec-

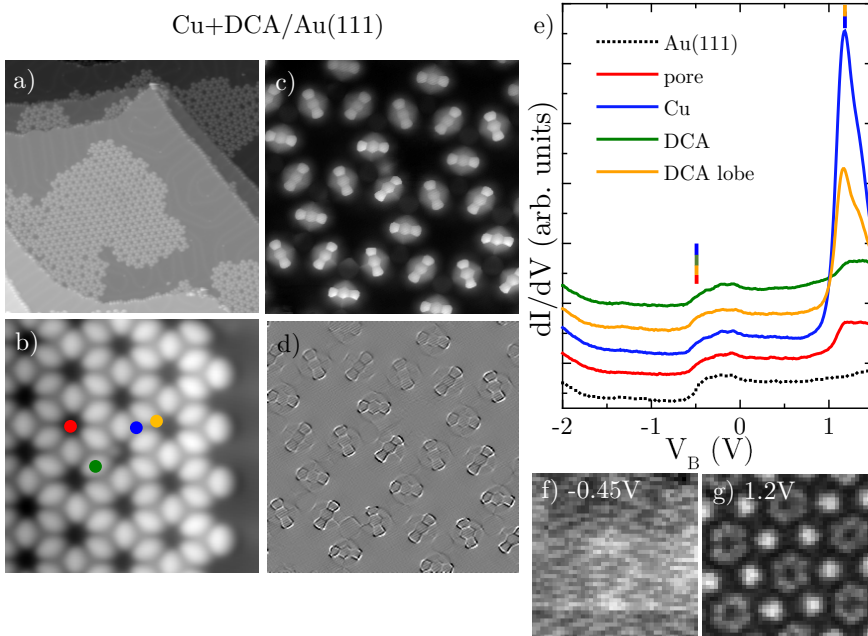


Figure 4.5: Structural and electronic characterization of the Cu+DCA/Au(111) system. a) Large overview of the sample. b) Close-up of the network. c) Constant height current map with a CO-functionalized tip, resolving C-C bonds. d) The same image than in c with a Laplacian filter. e) Electronic characterization using selected STS spectra obtained from  $dI/dV$  grids of this network. f), g)  $dI/dV$  grid maps at the energies highlighted in e. STM/STS parameters: a)  $75 \times 75 \text{ nm}^2$ ,  $I_t = 100 \text{ pA}/V_B = -1\text{V}$ ; b)  $10 \times 10 \text{ nm}^2$ ;  $I_t = 100 \text{ pA}/V_B = -1 \text{ V}$ ; c)  $V_B \approx 0 \text{ V}$ ; e) Regulation point:  $I_t = 100 \text{ pA}/V_B = -1 \text{ V}$ ;  $V_{rms} = 15.8\text{mV}$ ,  $f_{osc} = 817 \text{ Hz}$ .



tronic structure is apparently much simpler than the already studied networks on Ag(111). Since the electronic structure of all the M+DCA/Au(111) studied systems are quite similar when formed on this substrate, the different features will be described here and then briefly mentioned in the networks containing Fe and Co atoms. We observe only two main features: i) A broad step-like feature at  $\sim -0.45$  V that corresponds to the surface state. Note that we do not find confinement at the pores, so we infer that our surface state evolves into an interface state, which is indicative of a very weak interaction of the 2D-MOF with the Au(111) surface. ii) A very intense peak dominating at  $\sim 1.2$  V that is mainly located at the Cu adatoms and at the DCA lobes. It also carries some intensity on the DCA center and pore, probably contributed by the former positions. This state has been identified in the previous MHK lattices as the *multi-band state*. Although the metal centers seem highly decoupled from the substrate, the  $dI/dV$  grids performed at island borders failed again to show an edge state around this dominant peak.

### **Fe+DCA/Au(111)**

When we generate the MHK lattice using Fe as coordination atom on a Au(111) substrate, widely extended monodomain islands are easily formed, as presented in Figure 4.6. In Figure 4.6c, d, constant height current maps show non-periodic height differences between molecules, that are due to the Au(111) herringbone corrugation. In Figure 4.6e, the STS spectra extracted from a  $dI/dV$  grid and representing characteristic network positions is presented and is mainly characterized for the following features: i) A quite weak interface state without pore confinement. ii) The *multi-band state* observed as a prominent peak located mainly at the DCA lobe and Fe atom, in this case at  $\sim 0.6$  V and comparatively much weaker in intensity than in the Cu+DCA/Au(111).

### **Co+DCA/Au(111)**

Finally, Figure 4.7 presents the Co+DCA/Au(111) network, whose topography is as the previously described ones. Its electronic properties described from STS measurements presented in Figure 4.7c have as main features: i) The interface state located at all the measured points without traces of pore confinement. ii) The *multi-band state* as the most prominent peak at  $\sim 0.8$  V and again with strong contribution in the DCA edge and the Co coordination atom. In this case, the maximum intensity is apparently located at the pore. However, we infer that this intensity comes from a too broad tip probing all the DCA

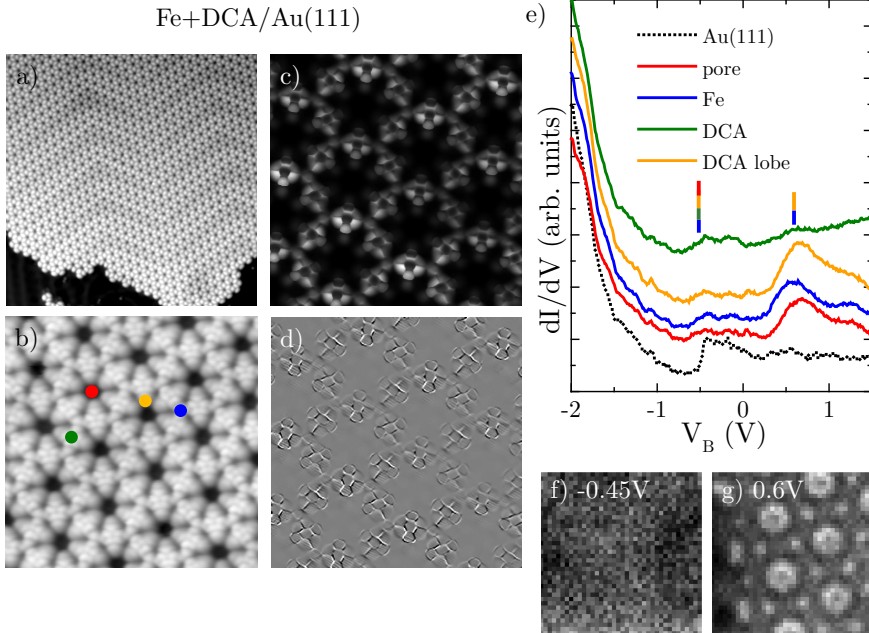


Figure 4.6: Structural and characterization of the Fe+DCA/Au(111) system. a) Large overview of the network. b) Small network close-up. c) Constant height current map performed with a CO-functionalized tip. d) The same than in c) with a Laplacian filtering. e) STS spectra at different network positions as extracted from a  $dI/dV$  grid. f), g)  $dI/dV$  grid maps at the energies highlighted in e). STS/STM parameters: a)  $50 \times 50 \text{ nm}^2$ ,  $I_t = 100 \text{ pA}/V_B = 1.7 \text{ V}$ ; b)  $8 \times 8 \text{ nm}^2$ ,  $I_t = 20 \text{ pA}/V_B = 10 \text{ mV}$ ; e) Regulation point:  $I_t = 100 \text{ pA}/V_B = -1 \text{ V}$ ;  $V_{rms} = 15.8 \text{ mV}$ ,  $f_{osc} = 817 \text{ Hz}$ .

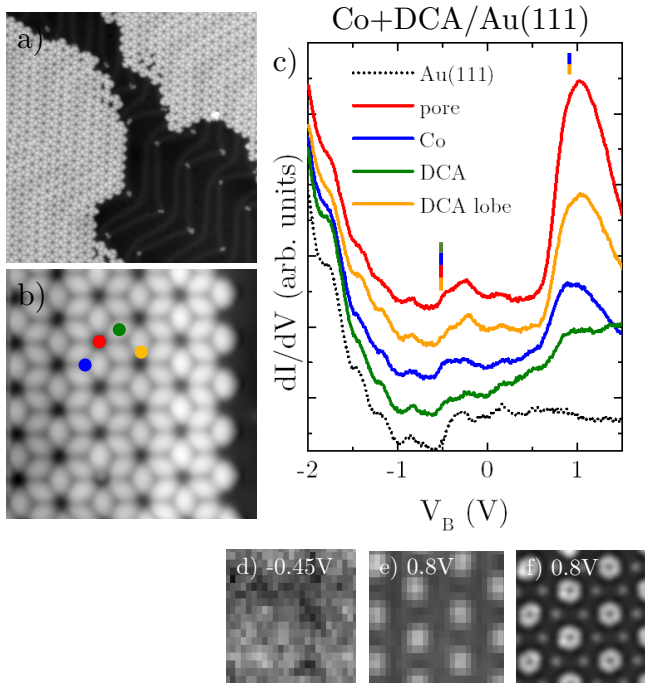


Figure 4.7: Structural and electronic characterization of Co+DCA/Au(111) system. a) Large overview of a monodomain island. b) Small close-up of a network edge. c) Electronic structure of the network acquired using a  $dI/dV$  grid and presented as STS at selected positions. d), e)  $dI/dV$  grid maps at the energies highlighted in c). f) Constant current  $dI/dV$  map at 0.8 V using a different tip than at the grid maps. STM/STS parameters: a)  $50 \times 50 \text{ nm}^2$ ,  $I_t = 100 \text{ pA}/V_B = 1.7 \text{ V}$ ; b)  $12 \times 12 \text{ nm}^2$ ,  $I_t = 200 \text{ pA}/V_B = -1 \text{ V}$ ; c) Regulation point:  $I_t = 100 \text{ pA}/V_B = -1 \text{ V}$ ;  $V_{rms} = 15.8 \text{ mV}$ ,  $f_{osc} = 817 \text{ Hz}$ ; e-f)  $5 \times 5 \text{ nm}^2$ .

lobes at the pore center accompanied by a low spatial resolution of the  $dI/dV$  grid (insufficient pixel density). Such ring-like feature exhibiting minimum intensity at the pore center is revealed at a constant height  $dI/dV$  map with an optimal tip in Figure 4.7f.

In conclusion, M+DCA/Au(111) networks interact weakly with the substrate, since the herringbone reconstruction is kept and an interface state (no evident pore confinement) is detected. Structurally, such networks are not planar, but follow the herringbone corrugation, which we believe to provide enough distortion to prevent the edge state formation, which we could never detect. Electronically, they host the characteristic and extended network state that we name as *multi-band state* in different unoccupied energies with dominant intensities. Surprisingly, the previous molecular states detected at the

MHK lattices formed on Cu(111) and Ag(111) are not observed in this energy window.

#### 4.1.4 MHK lattices on topological insulators

Finally, the Co+DCA network is formed on a 3D topological insulator as substrate ( $\text{Bi}_2\text{Te}_3$ ) that has a much lower density of states on its surface than the previous noble metal surfaces. Consequently, we expect a weakly interacting network with the underlying substrate. To form it, DCA molecules and Co atoms are subsequently evaporated onto the  $\text{Bi}_2\text{Te}_3$  substrate kept at  $\sim -30^\circ\text{C}$ . Once the network is formed, the sample has to be kept at temperatures below  $\sim -20^\circ\text{C}$  in order to avoid desorption. Unlike the metallic substrates previously studied, Co+DCA/ $\text{Bi}_2\text{Te}_3$  network only presents small islands limited in lateral size to 15 nm, as observed in Figure 4.8a, b. We find islands with two different orientation domains, that are rotated to each other by an angle of  $11^\circ$ , and the measured lattice parameter between pores is 2 nm.

The electronic structure of these islands is presented in Figure 4.8c-e. We distinguish two main features: i) a weak peak at  $\sim -0.4$  V mainly located at the DCA edge and the Co atom, and ii) a very prominent peak at  $\sim 0.8$  V distributed along all the island. The high intensity observed in the pore is probably due to a broad tip apex receiving intensity from different the DCA lobes accompanied by a low spatial resolution of the  $dI/dV$  grid (insufficient pixel density). Such ring-like feature exhibiting minimum intensity at the pore is revealed in Figure 4.8e. Such simple electronic structure is reminiscent of the networks generated on Au(111). This indicates a similar (and highly reduced) level of interaction of the networks with their underlying substrates.

## 4.2 Discussion

In this section we discuss and compare the topography and electronic structure of all MHK lattices of this and the previous chapter. Importantly, we did not find any topologically protected edge state in any of the studied networks, despite our efforts to tune both the SOC through the coordination adatoms and the substrate-network interaction by exchanging the substrate. Thus, the MHK lattices built with DCA molecules and  $3d$  atoms are not OTIs.

First, we consider the symmetry and registry of the networks, as they can play an important role in the morphological and electronic properties.

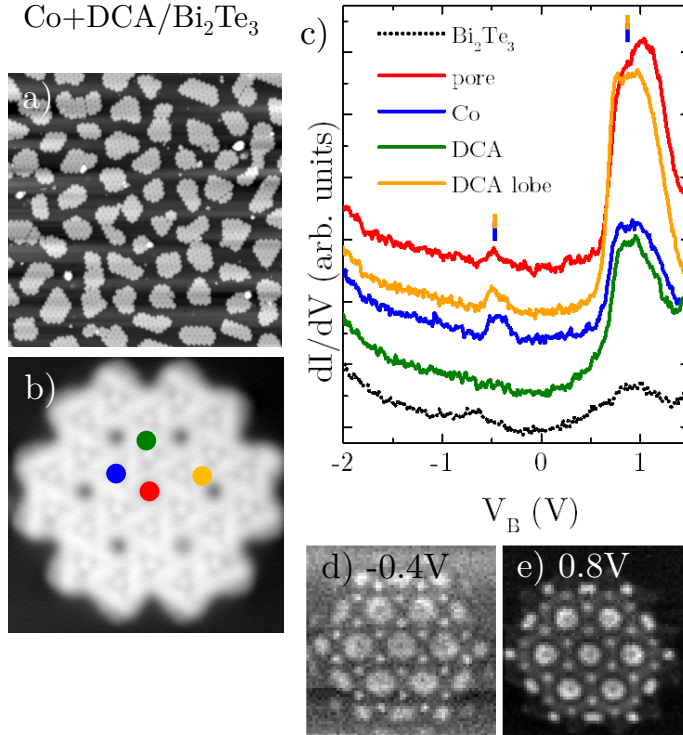


Figure 4.8: Structural and electronic characterization of the  $\text{Co}+\text{DCA}/\text{Bi}_2\text{Te}_3$  system. a) Large overview of different network assemblies. b) Detail of a network island. c) STS spectra performed at the characteristic network positions. d), e)  $dI/dV$  grid maps at the energies highlighted in c). STM/STS parameters: a)  $50 \times 50 \text{ nm}^2$ ,  $I_t = 100 \text{ pA}/V_B = 1.7 \text{ V}$ ; b)  $12 \times 12 \text{ nm}^2$ ;  $I_t = 200 \text{ pA}/V_B = 0.8 \text{ V}$ ; c) Regulation point:  $I_t = 100 \text{ pA}/V_B = -1 \text{ V}$ ;  $V_{rms} = 15.8 \text{ mV}$ ,  $f_{osc} = 817 \text{ Hz}$ .

We showed in Chapter 3 that the Cu+DCA network is commensurate with Cu(111) substrate, forming an  $(8 \times 8)$  supercell with pore distance of 2.04 nm, where all the benzene rings lie exactly onto a Cu atom and all the Cu adatoms lie on hollow substrate sites. However, the longer lattice vectors of Ag(111) and Au(111) substrates prevents the network from following the substrate's high symmetry directions. In principle, the herringbone reconstruction of the Au(111) could even hamper the formation of extended networks. However, LEED patterns show that M+DCA (where M=Fe or Co) lattices on Au(111) form a single domain, which is rotated  $30^\circ$  with respect to the substrate unit vectors. In this configuration, coordination atoms still lie on hollow substrate sites but the anthracene backbones can no longer follow the high symmetry directions. Contrarily, we find that M+DCA/Ag(111) networks form three different domains with non-equivalent intensities in the LEED pattern. There are two main predominant domains formed at  $30 \pm 16^\circ$  and a weaker one at  $30^\circ$ . Here, adatoms cannot be accommodated in straight lines of hollow substrate sites and the anthracene backbones deviate much more than on Au(111). We observe that some of the DCA molecules are rotated in order to align themselves with the substrate high symmetry directions, as observed in Figure 4.3c.

These deviations from a purely periodic structure result in symmetry breaking structures, that hampers the edge state formation. In other words, none of the networks are planar or symmetric MHK lattices, and all of them break mirror or inversion symmetries (taking the pore center as the origin of the coordinate system). Unlike Cu+DCA/Cu(111) symmetry breaking that turned out to be periodic, M+DCA/Au(111) lattices are found to reduce their overall planarity by following the corrugation of the herringbone reconstruction. M+DCA/Ag(111) lattices instead, break the symmetries by molecule rotation with respect to the network high symmetry directions, due to an imperfect matching with the substrate and also bending the anthracene backbones. Such morphological distortions block the presence of protected topological edge states as discussed in the previous chapter.

In the following, we analyze the electronic properties of such networks. Figure 4.9 presents the collection of STS spectra from all the MHK lattices studied, including Cu+DCA/Cu(111) from Chapter 3. Rows represent network STS spectra performed on different substrates, while columns correspond to the coordination atom. Judging by these spectra, the MHK lattice electronic structure is more affected by the underlying substrate than by its coordination atom. Nevertheless, some influence on the electronic features is still exerted by the choice of these coordination adatoms. In Table 4.1, in the Supplementary material section, a summary of all the states found in these systems is

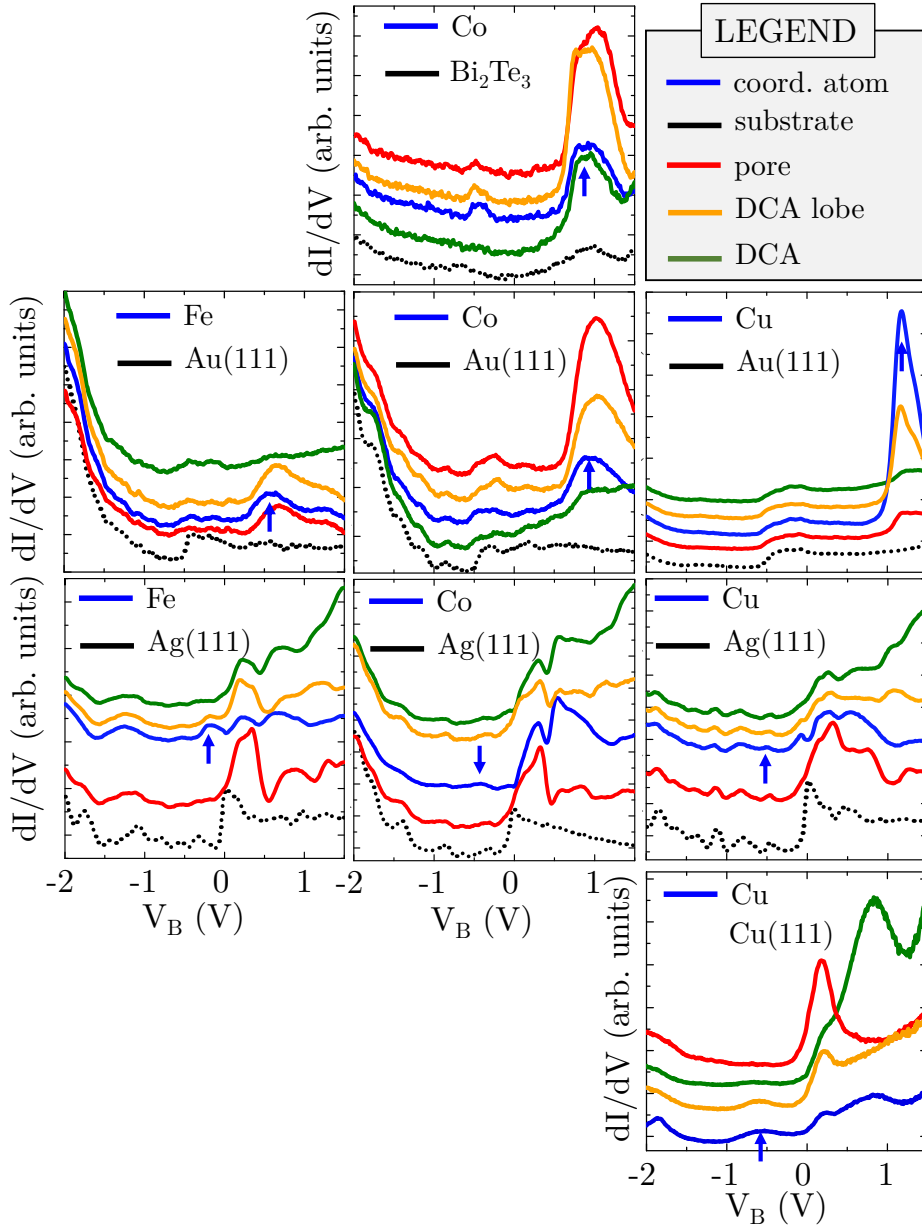


Figure 4.9: Collection of the STS spectra presented in the MHK lattices described in Chapters 3 and 4. Each row corresponds to a different substrate and each column to a coordination atom. STS parameters can be found in the corresponding previous figures. Blue arrows in graphs mark the energy where the extended network band identified in Chapter 3 (i.e., the *multi-band state*) is found on each system.

presented.

A measure of the interface interaction between the surface nanostructures and the underlying substrate can be assigned to the modification and confinement of the surface state. The presence of a pristine surface state or an interface state in a metallic substrate upon molecule deposition indicates a weak coupling between them [126–128]. Contrarily, when a strong coupling occurs, the metallic surface state is quenched [129, 130] or very strongly confined in porous structures. Thus, the intensity and shape of the *pore state* provides a qualitative measure of the degree of network-substrate coupling [98–101, 131]. In Figure 4.10 we present the STS spectra obtained at the pore on all the studied MHK lattices. Cu+DCA network formed on Cu(111) strongly confines its surface state, giving as a result a prominent peak at  $\sim 0.2$  V, with an estimated bandwidth of 0.4 V. This suggests a strong network-substrate interaction. In the case of M+DCA lattices formed on Ag(111) substrate, a confined surface state is present in all of them with its maximum intensity at  $\sim 0.3$  V. However, compared to the Cu(111) case, they exhibit broader bandwidths and smaller SS shifts with respect to their pristine case. These two experimental findings agree with a lower pore confinement and larger electronic intercoupling induced by the network on the Ag(111) substrate in comparison with Cu(111). Finally, Au(111) surface state electrons appear to be weakly modified by the presence of M+DCA networks. An electronic surface state is ubiquitous and no confinement of such states is observed in our measurements, which suggests the weakest interaction. Therefore, we conclude by analyzing the pore STS spectra that the networks exhibit a strong scattering of surface electrons with Cu(111), intermediate with Ag(111) and rather weak with Au(111).

Topological insulators used as substrates can also have their surface states affected by the self assembly of molecules on them [132–136]. Although Bi<sub>2</sub>Se<sub>3</sub> has been shown to quench its surface state in the first quintuple layer upon CoPc deposition, the same molecules on Bi<sub>2</sub>Te<sub>3</sub> keep it almost unaltered [132–134]. The authors attribute this to the larger electron affinity of Se atoms that form the substrate in the first case. However, the similar electron affinity of Co, Bi and Te, prevents them from developing strong interactions [134]. Thus we expect the Co+DCA/Bi<sub>2</sub>Te<sub>3</sub> system to be weakly interacting, which is further supported by the similarities between this system electronic structure and the corresponding of the 2D-MOF formed on Au(111).

Three different states are found in the unoccupied part of all the M+DCA systems formed on Ag(111) in the vicinity of 0.6, 1.1 and 1.5 V, which we respectively named *ciano state*, *anthracene broad state* and *anthracene slim state*.



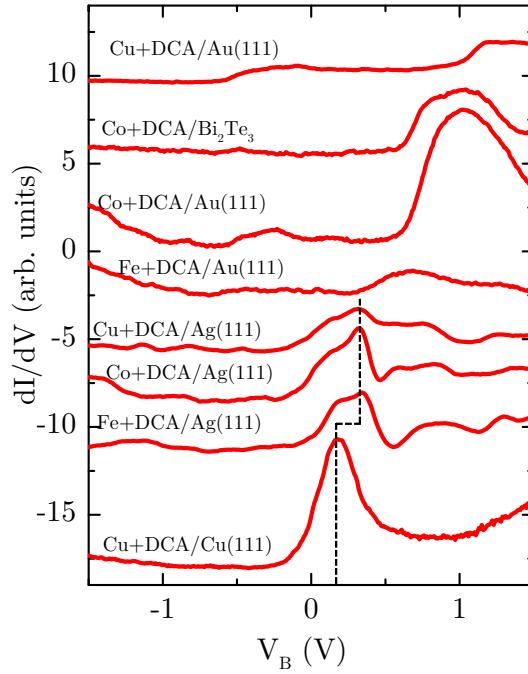


Figure 4.10: Evolution of the *pore state* measured by STS at all the MHK lattices. The black dashed line marks the energy of the confined surface state in those systems presenting it. Cu+DCA/Cu(111) and all the M+DCA/Ag(111) networks present a confinement of the surface state, but Co+DCA/Bi<sub>2</sub>Te<sub>3</sub> or M+DCA/Au(111) do not. Their main features are contributions from neighbouring *multi-band states*.

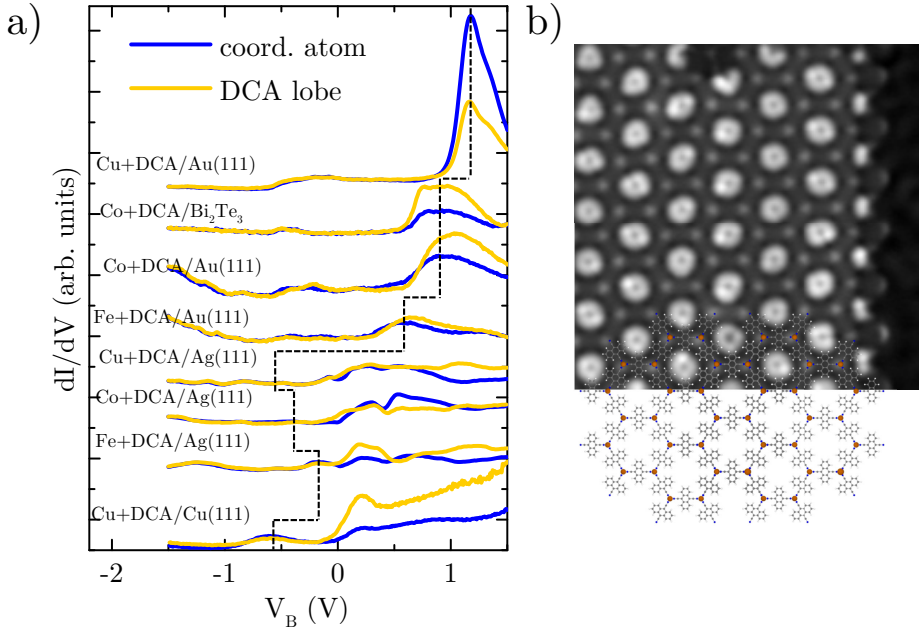


Figure 4.11: Network conjugated *multi-band state* at the MHK lattices of the same kind as the one identified in Chapter 3 for Cu+DCA/Cu(111). a) All STS from DCA lobes and coordination atom spectra are presented, that were identified as the kagome band manifold there. The black dotted line marks the energy where the *multi-band state* is found on each system. b)  $dI/dV$  constant current map of a Co+DCA/Au(111) system performed at its corresponding energy. It evidences the distribution of the *multi-band state* intensity in DCA lobes and coordination atoms. STM/STS parameters:  $I_t = 200$  pA/ $V_B = 0.9$  V;  $V_{rms} = 50$  mV,  $f_{osc} = 817$  Hz.

We assign these peaks to a molecular origin, based on the displayed LDOS intensities. Moreover, the energy shifts are relatively small for the different coordination atoms. Two similar features were observed in Cu+DCA/Cu(111) systems as shown in Figure 3.5 in Chapter 3 that were clearly separated in energy (0.8 V and 1.5 V). However, M+DCA networks formed on Au(111) do not present these molecular states in the probed energy range. We assign such absence to the much higher energy position of the LUMO in the purely molecular DCA assembly (1 V higher than on Ag(111) substrate, see Fig. 4.1).

Most importantly, we identify a *multi-band state* common to all the studied MHK lattices. It is simultaneously localized at coordination atoms and DCA lobes, denoting the formation of a conjugated network band in all these 2D-MOFs [124]. This was previously identified as the kagome manifold band in Chapter 3 for the case of Cu+DCA/Cu(111). In Figure 4.11 we present the STS spectra of the DCA lobes and coordination atoms of all the MHK lattices and tag the energy of this *multi-band state* for each network (discontinuous black line), as well as a  $dI/dV$  map that shows its generic spatial distribution. Interestingly, it depends energetically on the coordination atom and underlying substrate, as indicated in Table 4.1, in the Supplementary material section. This state does not present the same intensity in all the networks; in some cases, they are practically undetected in a STS spectrum but still visible in  $dI/dV$  maps. We believe this variations to be indicative of different network-substrate interactions [122]. In Figure 4.16 in the Supplementary material section, the corresponding  $dI/dV$  maps at the *multi-band state* energy are shown for all the MHK lattices. The energy and intensity of this conjugated network state appear to be mainly conditioned by the underlying substrate: on Au(111) and Bi<sub>2</sub>Te<sub>3</sub> we find them as very prominent peaks in the STS spectra, whereas on Ag(111) and Cu(111) they are either very weak or practically unnoticed features. This is in agreement with the already discussed surface state alteration between network and substrate in the pore spectra analysis and in other studies [137].

To a lesser extent, the coordination atom also plays a role in this network-substrate interaction. Such phenomenon has been widely studied on transition metal phtalocyanine molecules on different substrates [134, 138–141] and suggest stronger molecule-substrate interaction for transition metals with lower atomic number. This happens because a lower filling of 3*d* states of transition metal atoms promotes a higher coupling with substrates. In our case, this dependency is clearly observed for all M+DCA/Au(111) networks, where the *multi-band state* presents narrower and more intense peaks at higher energies on the network coordinated with Cu, followed by Co and finally Fe. However,

MHK networks formed on Ag(111), where a stronger interaction exists, such relation between band state energy and atomic number is reversed.

Around these *multi-band state* is where a topologically protected edge states should show up. However, it has not been observed in any of the 7 systems, not even in Cu+DCA/Au(111) where the weakest coupling has been found. Notably, a non-planar configuration is detected also in this case, generalizing the inversion and symmetry breaking on these particular MHK lattices.

Interestingly, all the studied MHK networks formed on Ag(111) and Cu(111) have their *multi-band states* in the occupied part, whereas Bi<sub>2</sub>Te<sub>3</sub> and Au(111) show this characteristic state in the unoccupied region. This explains that in STM topography images performed at  $V_B = -1$  V, the coordination atom is observed in Ag(111) and Cu(111). Such observation is remarkable, since coordination atoms in similar 2D-MOFs are rarely visualized by STM [142–147]. In this case it is observed due to the formation of an extended state overlapping between molecules and adatoms [34]. At this large negative bias, we are probing all the states at energies comprised between  $-1 \text{ V} \leq V_B \leq 0 \text{ V}$ , which contains the *multi-band state* of MHK lattices formed on Ag(111) and Cu(111). Contrarily, the coordination atoms on Au(111) and Bi<sub>2</sub>Te<sub>3</sub> substrates become visible when scanning at sufficiently high positive bias voltages, where the *multi-band state* becomes accessible.

### 4.3 Conclusions

In this chapter we have formed 7 analogous MHK lattices, using as reference Cu+DCA/Cu(111) network studied in the previous chapter. For this, we have used different substrates [Ag(111), Au(111) and Bi<sub>2</sub>Te<sub>3</sub>] and coordination atoms (Fe, Co, Cu) to tune the interface interaction. Extended and monodomain islands of network are formed on the metallic substrates. We find that M+DCA networks grown on Ag(111) are slightly more decoupled from the substrate than Cu+DCA/Cu(111). However, when using Au(111) or Bi<sub>2</sub>Te<sub>3</sub> as substrate, an even higher decoupling is found. The network electronic properties are mainly conditioned by their underlying substrate, but slight variations are observed also depending on the coordination atom. We identify in all the structures *multi-band states* where the edge states should be hosted. However, edge states were recurrently absent, independently of the level of interaction between network and substrate. We ascribe the origin of the topological protection loss (i.e., closing of the mini-gaps) to the structural symmetry breaking that is produced in all the studied systems.

## 4.4 Supplementary material for Chapter 4

In this section, some supplementary Figures are presented to support the main findings from the chapter.

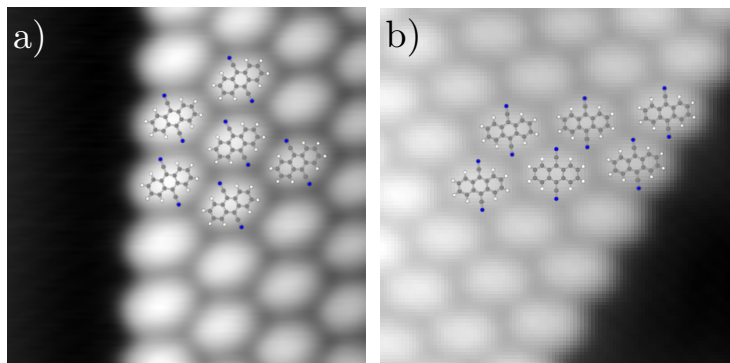


Figure 4.12: Structure of DCA compact assemblies on a) Au(111) and b) Ag(111) formed with hydrogen bonds, since there are no coordination atoms. STM parameters:  $5 \times 5 \text{ nm}^2$ ,  $I_t = 100 \text{ pA/V}_B = -1 \text{ V}$ .

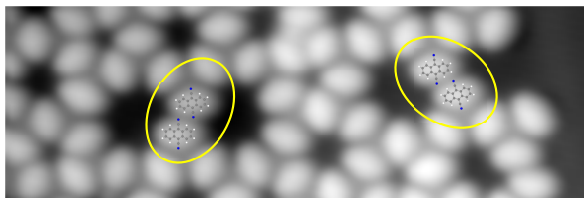


Figure 4.13: The formation of larger pores in Cu+DCA/Au(111) networks has been observed to occur due to hydrogen bonding between DCA molecules. STM parameters:  $5 \times 15 \text{ nm}^2$ ,  $I_t = 100 \text{ pA/V}_B = -1 \text{ V}$ .

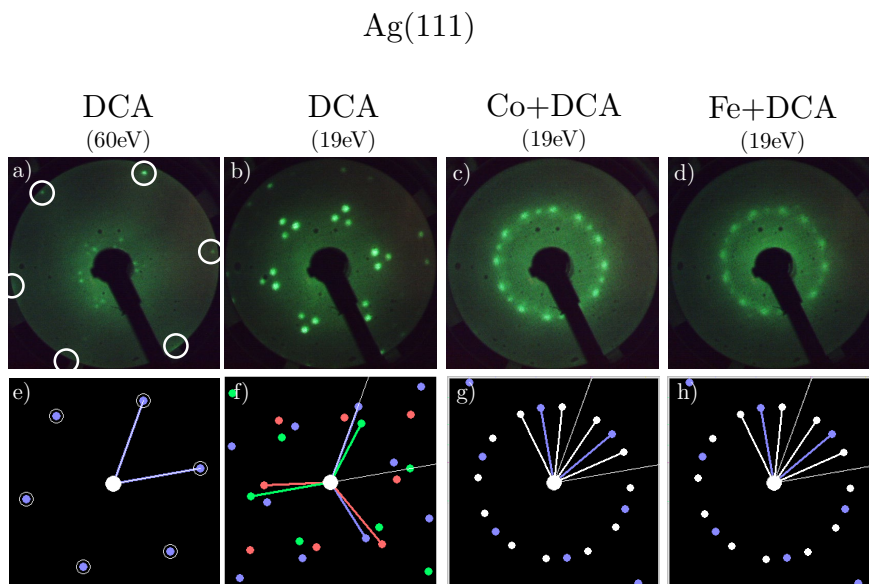


Figure 4.14: LEED characterization of MHK networks on Ag(111). a-d) present real LEED patterns, while at e)-h) we present the corresponding simulated patterns. a) At 60 eV, the first order substrate spots, that are highlighted with white circles, are detected. b) Pattern of the DCA compact assembly without metal coordination, that follows the substrate high symmetry directions. c) and d) correspond to Co+DCA and Fe+DCA networks, that have the same structure and LEED pattern containing three different domains with different intensities rotated with respect to the substrate. e) Simulated patterns from the clean substrate, f) DCA molecular assembly and g), h) the molecular islands of M+DCA networks on Ag(111). The dots represent the network spots and their colour, a different domain. The white lines indicate the substrate first order spots directions.

## Au(111)

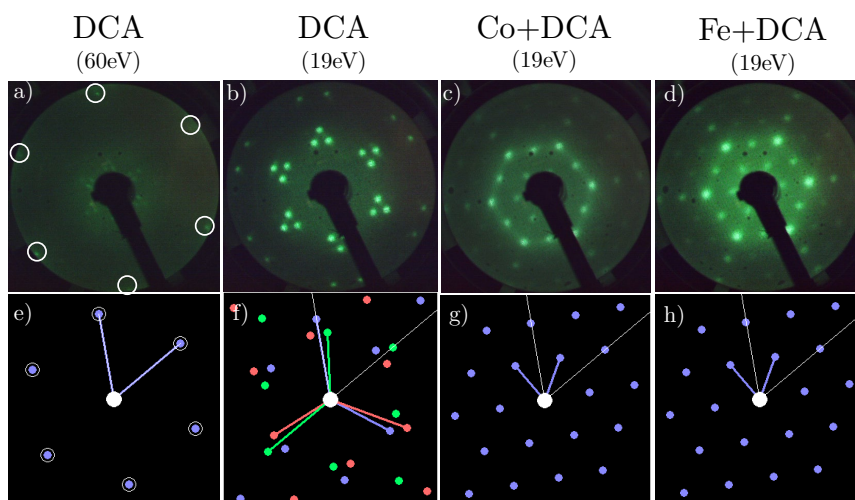


Figure 4.15: LEED characterization of MHK networks on Au(111). a)-d) present real LEED patterns, while at e)-h) we present the corresponding simulated patterns. a) At 60 eV, the first order substrate spots, that are highlighted with white circles, are detected. b) Pattern of the DCA compact assembly without metal coordination, that follows the substrate high symmetry directions. c) and d) correspond to Co+DCA and Fe+DCA networks, that have the same structure and LEED pattern, which is rotated  $30^\circ$  with respect to the substrate. e) Simulated patterns from the clean substrate, f) DCA molecular assembly and g), h) the molecular islands of M+DCA networks on Au(111). The dots represent the network spots and their colour, a different domain. The white lines indicate the substrate first order spots directions.

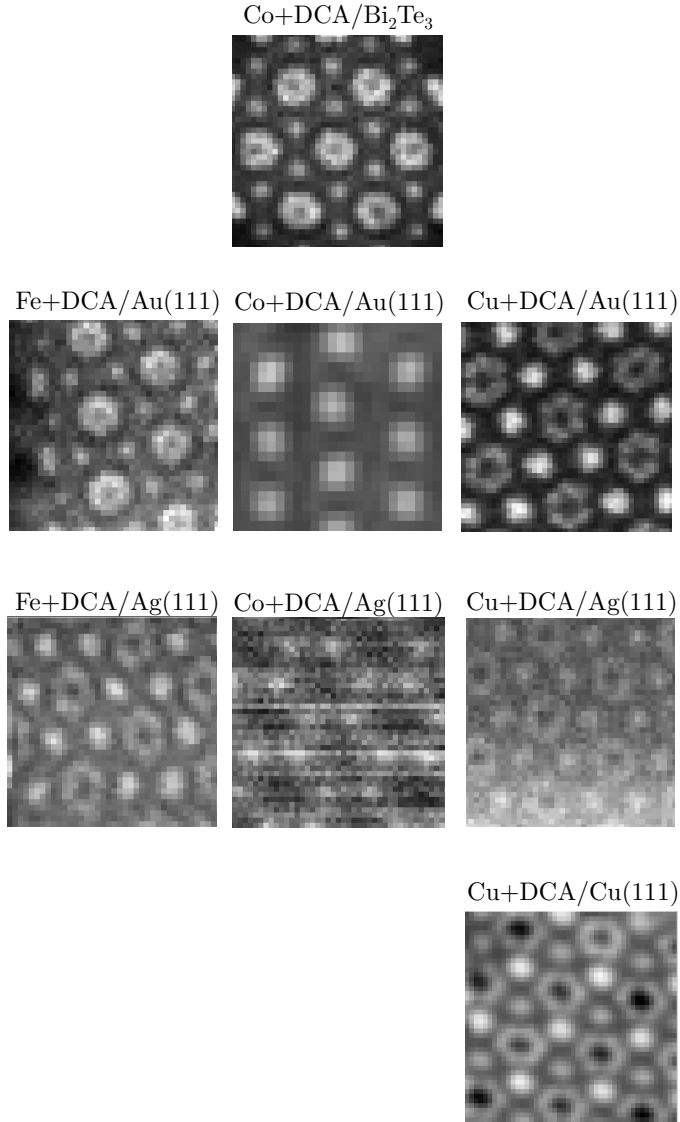


Figure 4.16: *Multi-band state* ubiquity in MHK lattices. All the studied systems contain this network state visualized at different energies. The images are obtained from  $dI/dV$  grids at the energy indicated on Table 4.1. Note that the proper visualization of these images depends on the tip morphology. Here, the details of Co+DCA/Au(111) network state are not properly visualized, but they are in Figure 4.11b. The low image quality and existing distortions are due to the pixel size of these grids and the long acquisition time required for these measurements ( $\sim 24$  to 40h). All images dimensions  $5 \times 5 \text{ nm}^2$ . STS parameters are indicated on the previous corresponding figures.



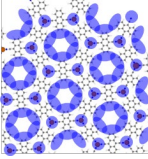
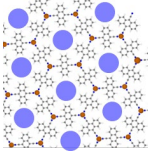
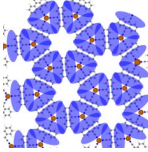
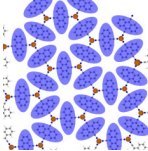
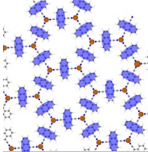
	Cu(111)	Ag(111)	Au(111)	Bi <sub>2</sub> Te <sub>3</sub>
	<i>multi-band state</i>			
Fe		-0.25	0.6	
Co		-0.43	0.8	0.8
Cu	-0.6	-0.55	1.2	
	<i>pore state</i>			
Fe		0.3	-	
Co		0.3	-	-
Cu	0.2	0.3	-	
	<i>cyano state</i>			
Fe		0.6	-	
Co		0.6	-	-
Cu	-	0.6	-	
	<i>anthracene broad state</i>			
Fe		1.1	-	
Co		1.1	-	-
Cu	0.8	1.1	-	
	<i>anthracene slim state</i>			
Fe		1.5	-	
Co		1.5	-	-
Cu	1.5	1.5	-	

Table 4.1: Energy (in V units) where the indicated states are located on each system. Columns classify by substrates and lines, by coordination atom.



## Chapter 5

# Magnetic properties of DCA-based 2D-MOFs

In the previous chapters, we have been able to grow extended M+DCA networks that share a coherent state (that we named *multi-band state*) independently of the noble metal substrate and 3d-atom coordination. The fact that these networks were grown using magnetic atoms (Fe, Co) offers the possibility to investigate the magnetic response of these networks. Indeed, a central problem in theoretical magnetism, and specifically 2D magnetism, is the Ising model. In 1920, Lenz proposed this model to his student Ising, who solved it in 1923 in the form of a scientific article [148]. It describes a regular lattice of nodes (in 1D, 2D or 3D) that can adopt one of two variables (spin-up or spin-down). Each node interacts with those around it in such a way that the total energy of the system is lower if one node has the same spin than their neighbors [149]. Ising demonstrated that in 1D a transition phase to an ordered (ferromagnetic) phase was not possible at finite temperature [148]. Almost two decades later, in 1944, Onsager obtained the exact analytical solution in 2D by calculating the partition function [150] showing that a phase transition takes place in 2D for 1D (Ising) spins. However, on the basis of the Heisenberg model (3D spins), that includes more complicated interactions between spins, Mermin and Wagner predicted that no phase transition could occur in 2D Heisenberg-like magnetic materials [151]. Berezinskii [152], Kosterlitz and Thouless [153] showed that a 2D array of 2D spins attain a topologically non-trivial, short-range ordered state, but a long-range order was never attained. For this reason, finding experimental evidence of 2D ferromagnetic materials is an important issue for the complete understanding of such models and our

M+DCA networks allows us to carry it out.

In addition to the interest of 2D systems as an experimental approach to theoretical models, low-dimensional magnetism could also be potentially relevant for applications in the industry. The miniaturization of devices has promoted the need for smaller magnets, however, they are reaching their fundamental limit. The magnetic anisotropy of a magnet can be expressed as  $nK$ , where  $n$  is the number of atoms forming the magnet and  $K$  the magnetic anisotropy per atom. This factor has to be high enough to overcome thermal fluctuations ( $\sim k_B T$ ). A logical path to search for a solution when decreasing the number of atoms is to increase the anisotropy per atom. The magnetic anisotropy is strongly related to the orbital moment, which, in turn, depends on its local environment. Notably, 2D-MOFs have metallic coordination atoms in a low-coordination environment produced by the ligand field that present a small (yet relevant) electronic decoupling from the substrate. These conditions provide an escape pathway from the orbital quenching typical of bulk materials.

Here, we study by means of XAS and XMCD the magnetic properties of M+DCA networks (where M=Fe, Co) on Ag(111) and Au(111). Such 2D materials could be an optimal experimental approach to the Ising model if they present strong uniaxial anisotropy and magnetic centers interacting to each other. Indeed, we find that Fe+DCA network fulfills these conditions when formed on Au(111) and constitutes a metal-organic 2D ferromagnet with  $T_C \sim 35$  K. Contrarily, the Fe magnetic moment is almost vanished when the same network is formed on Ag(111). Finally, Co+DCA networks present quite isotropic orbital magnetic moments on both substrates with no evidence of magnetic ordering.

## 5.1 Results and discussion

The measured 2D-MOFs were prepared as described in Chapter 4. Here, special care was placed in obtaining the precise stoichiometry between DCA and coordination atoms (3:2). An excessive evaporation of atoms would result in the formation of metallic clusters that could bury the signal coming from the coordination atoms. Thus, we were extremely carefull to obtain a coverage of  $\sim 1/32$  ML. The metal adatom local environment is determined by a planar (approximately) three-fold symmetry formed by the N atoms from the molecular cyano groups and the underlying surface ( $C_{3v}$ ). XAS and XMCD measurements were performed at the  $L_{2,3}$  edges of Fe and Co. All the mea-

measurements presented here were acquired at the ID32 beamline of ESRF and BOREAS beamline in ALBA. XAS (and XMCD) spectra shown in this chapter were measured at  $H=6$  T and  $T\sim 2$  K unless otherwise stated.

### 5.1.1 Ferromagnetism in 2D-MOFs: Fe+DCA/Au(111)

We study first the magnetic properties of Fe+DCA/Au(111) network by X-ray techniques. Figure 5.1a, b presents XAS and XMCD spectra acquired at normal ( $\varphi = 0^\circ$ ) and grazing ( $\varphi = 70^\circ$ ) incidence. In all XAS spectra, Fe  $L_{2,3}$  edges are found on top of an oscillating background, which is the extended X-ray absorption fine structure (EXAFS) of the underlying substrate (Au). To unambiguously determine that these spectra correspond to Fe single atoms embedded on the metal-organic network, an identical sample preparation was carried out without molecules (Fig. 5.1c, d). For this, the same Fe quantity was evaporated under identical conditions directly on a clean Au(111) substrate [Fe/Au(111)]. Such preparation is known to result in the formation of small Fe clusters on the herringbone elbows [154, 155]. XAS and XMCD spectra obtained from these Fe clusters (see Fig. 5.1c, d) strongly differ from those corresponding to the network (see Fig. 5.1a, b), indicating that the Fe atoms have very different chemical environments.

In Fe+DCA/Au(111) system, the larger peak intensity at normal incidence compared to the grazing incidence in the XMCD spectra, clearly suggests a strong anisotropy with an out-of-plane easy magnetization axis. Contrarily, Fe/Au(111) spectra do not present such a strong difference, but still shows an out-of-plane easy magnetization axis. This indicates that embedding single Fe atoms in the network highly increases their anisotropy.

The line shape of XAS and XMCD spectra yields information on the electronic configuration. Fe/Au(111) XMCD spectra are formed by two broad peaks corresponding to  $L_3$  and  $L_2$  edges, respectively. This type of line shapes with smooth and broad features are typical from metals [156, 157]. Contrarily, in Fe+DCA/Au(111) those  $L_3$  and  $L_2$  edges are not broad but present contribution from different narrow peaks. This type of spectrum is common to systems of Fe atoms isolated on surfaces [157, 158], embedded in other 2D-MOFs [159], in molecules [160] or oxides [161]. Another difference between our two studied systems is the relative intensity of  $L_3$  and  $L_2$  XMCD edges ( $L_3/L_2$  branching ratio). In Fe+DCA/Au(111) it is much higher than in the purely metallic system, which is indicative of a high Fe orbital moment.

To get insight into the oxidation state of Fe atoms embedded in the net-

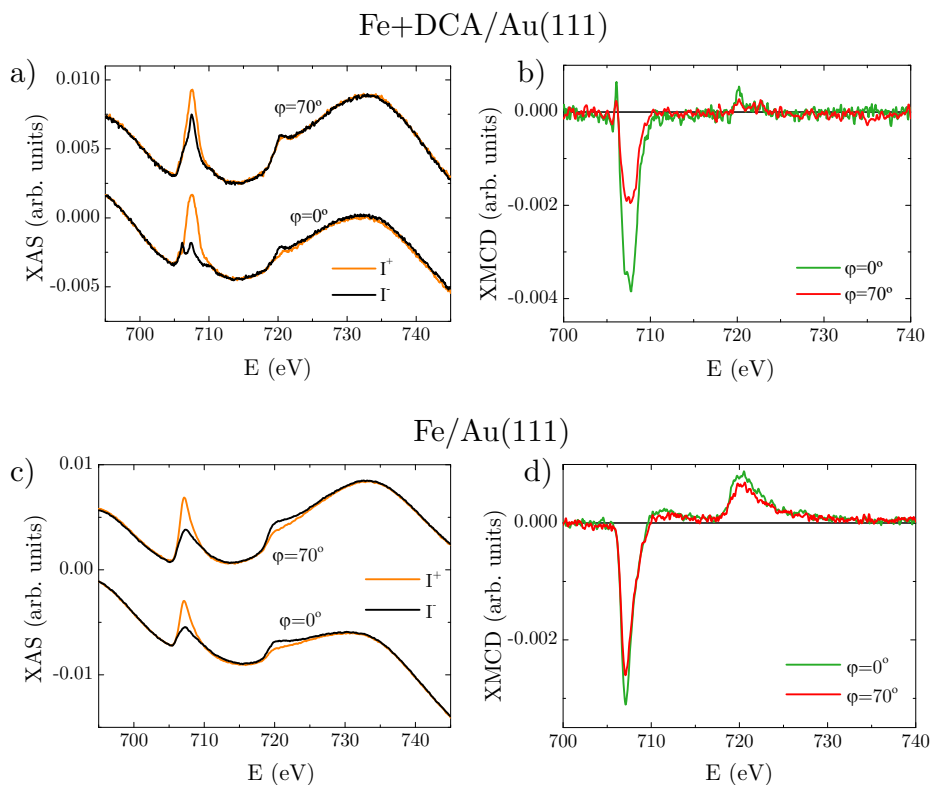


Figure 5.1: Fe+DCA/Au(111) and Fe/Au(111) systems XAS and XMCD characterization. a) Fe+DCA/Au(111) XAS spectra acquired with parallel and antiparallel X-ray alignment with respect to the external magnetic field for normal and grazing incidence at the  $L_{2,3}$  edges of Fe. This signal sits on top of the Au EXAFS background. b) XMCD spectra obtained from data in a. The different intensity in the  $L_3$  peaks measured at normal and grazing incidence suggests a strong out-of-plane anisotropy. Also, the high  $L_3/L_2$  branching ratio reveals a high orbital magnetic moment. c) Fe/Au(111) XAS spectra acquired in identical conditions as in a. d) XMCD spectra obtained from data in c. XAS and XMCD line shapes strongly differ from one system to the other, indicating that the Fe atoms have very different chemical environments.

work, multiplet calculations were performed with CRISPY software [162], from Quanty [163]. A good correspondence with our experimental results is found with  $\text{Fe}^{2+}$ , as shown in Figure 5.10 in the Supplementary material section.  $\text{Fe}^{2+}$  usually presents a  $3d^6$  electronic configuration, that is compatible with a high orbital moment and strong anisotropy. In contrast,  $\text{Fe}^{3+}$  typically arranges into a  $3d^5$  electronic configuration. According to the Hund's rules, this yields maximum spin moment ( $S=5/2$ ) and no orbital moment ( $L=0$ ), except for very strong crystal fields. Such orbital and spin magnetic moments would be hardly compatible with the high orbital moment or strong anisotropies that we detect in the measured spectra.

Orbital and spin magnetic moments can be estimated from XAS and XMCD spectra through the calculation of the sum rules (already indicated in Eqs. 2.9 and 2.10) [82, 83]. We used spectra acquired at 4 different incidence angles ( $\varphi = 0^\circ, 30^\circ, 54.7^\circ, 70^\circ$ ). In such an uniaxial ( $C_{3v}$ ) system, the angle dependence of the orbital and effective spin magnetic moments is, respectively [164]:

$$\mu_L(\varphi) = \mu_L^z \cos^2(\varphi) + \mu_L^{xy} \sin^2(\varphi) \quad (5.1)$$

$$\mu_S^{\text{eff}}(\varphi) = \mu_S - 7[\mu_T^z \cos^2(\varphi) + \mu_T^{xy} \sin^2(\varphi)] \quad (5.2)$$

where  $\mu_S = -2\langle S_z \rangle \mu_B / \hbar$  is isotropic, but both the orbital moment  $\mu_L(\varphi) = -\langle L_z^\varphi \rangle \mu_B / \hbar$  and the dipole magnetic moment of the spin density distribution  $\mu_T(\varphi) = \langle T_z^\varphi \rangle \mu_B / \hbar$  are intrinsically anisotropic. The dipolar tensor is traceless, and therefore  $\mu_T^z + 2\mu_T^{xy} = 0$ , leaving only four moment components in Eqs. 5.1 and 5.2 as independent. A particular case worth mentioning occurs at the so-called *magic* incident angle ( $\varphi^m = 54.7^\circ$ ), where  $2\cos^2(\varphi^m) = \sin^2(\varphi^m)$  so the dipolar term is canceled in Eq. 5.2 yielding a direct measure of  $\mu_S$  [165].

In Figure 5.2 the magnetic moments obtained from the sum rules as well as their fitting to Eqs. 5.1 and 5.2 are presented for Fe+DCA/Au(111) and Fe/Au(111). The fitting parameters are indicated in Table 5.1. Fe/Au(111) and Fe+DCA/Au(111) present large differences in their orbital magnetic moments, as previously deduced by their XMCD line shapes. This is in accordance with the different ligand environment of Fe atoms when forming clusters or embedded in the 2D-MOF. Fe+DCA/Au(111) has a very high out-of-plane orbital moment ( $\mu_L^z = 1.5 \mu_B/\text{Fe}$ ) with a strong anisotropy. In contrast, Fe/Au(111) clusters present a slight out-of-plane anisotropy with an orbital moment reduced by  $\sim 84\%$  with respect to the molecular array ( $\mu_L^z = 0.24 \mu_B/\text{Fe}$ ). In contrast, the spin moment is almost unchanged in both systems.

Element-specific magnetization curves were obtained by recording the XMCD

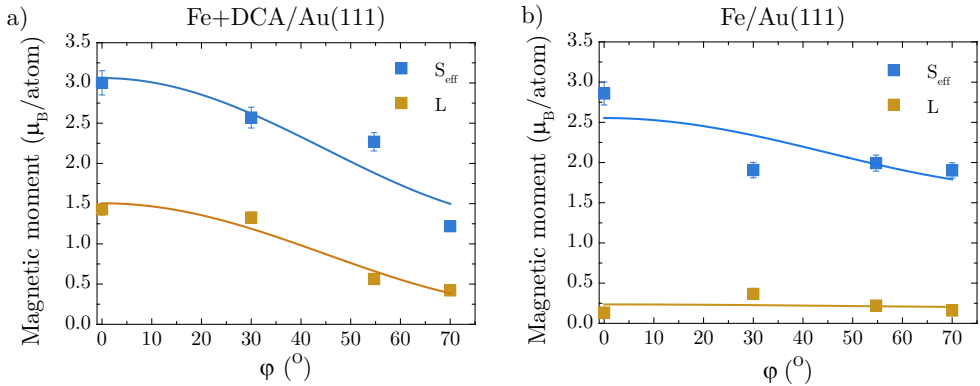


Figure 5.2: Angular dependence of the orbital and spin effective moments of a) Fe+DCA/Au(111) and b) Fe/Au(111) obtained from the sum rules. The data are fitted to Eqs. 5.1 and 5.2. The orbital moment is higher and much more anisotropic in the 2D-MOF than for the Fe atoms directly adsorbed on the Au substrate.

	$\mu_L^{xy}$ ( $\mu_B$ )	$\mu_L^z$ ( $\mu_B$ )	$\mu_S$ ( $\mu_B$ )	$\mu_T^z$ ( $\mu_B$ )
Fe+DCA/Au(111)	$0.24 \pm 0.12$	$1.50 \pm 0.15$	$1.88 \pm 0.20$	$-0.17 \pm 0.04$
Fe/Au(111)	$0.2 \pm 0.11$	$0.24 \pm 0.10$	$1.98 \pm 0.22$	$-0.08 \pm 0.02$

Table 5.1: Orbital and spin magnetic moments of Fe in Fe+DCA/Au(111) and Fe/Au(111) obtained from fitting the points in Fig. 5.2 and following Eqs. 5.1 and 5.2.



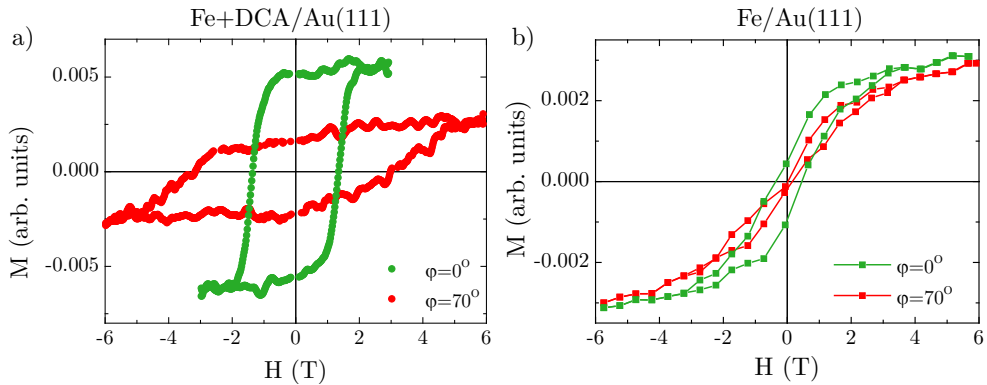


Figure 5.3: a) Fe+DCA/Au(111) hysteresis loop measured at the  $L_3$  edge of Fe at normal ( $\varphi = 0^\circ$ , green) and grazing ( $\varphi = 70^\circ$ , red) incidence. Both measurements present open loops with very high coercive fields, which is  $\sim 1.5$  T for the out-of-plane and  $\sim 3$  T for the in-plane. Such condition has never been reported in a 2D-MOF. At normal incidence, the magnetization is saturated at 1 T, while at grazing incidence it is not saturated even at 6 T, which evidences a huge anisotropy. b) Fe/Au(111) magnetization curves measured at normal and grazing incidence. Coercive fields are lower than 1 T for both incidence angles. Indeed, the grazing incidence curve presents a butterfly hysteresis loop. Each point plotted corresponds to the average of 25 measured experimental points.

signal at the  $L_3$  edge energy as a function of the magnetic field, cycling it from 6 to  $-6$  T and back to 6 T at normal and grazing incidence. Figure 5.3 shows the curves obtained for both systems. Fe+DCA/Au(111) presents open hysteresis loops with high coercive field values for both incidences. At normal incidence, the coercive field is  $\sim 1.5$  T and magnetization is saturated at a field of less than  $\sim 1$  T. At grazing incidence, we found a coercive field of  $\sim 3.1$  T while saturation is not reached at 6 T, (maximum accessible field at BOREAS). This evidences the high magnetic anisotropy in this 2D-MOF as well as the presence of collective magnetism. In the Fe/Au(111) system (see Fig. 5.3b), magnetization curves at both incidences present similar behavior. At 6 T both incidences show similar magnetization values without fully reaching saturation. Moreover, the coercive field is significantly less than 1 T for both incidences. In fact, at grazing incidence, the magnetization curve presents a closure at 0 T forming a butterfly hysteresis, that is characteristic of systems with long relaxation times [166, 167]. Such differences evidence that the hysteresis loop signals shown in Figure 5.3a come almost exclusively from Fe atoms embedded in the 2D-MOF.

To gain further insight on the interaction between Fe atoms and to con-

firm that these novel hysteresis loops come from a collective behavior of Fe atoms, two different experiments were performed. First, XMCD spectra were recorded as a function of temperature (see Fig. 5.4a, b) under a very small applied field ( $H=0.05$  T). Starting from RT, XMCD spectra were sequentially acquired at decreasing temperatures until clear detection of a XMCD signal occurred at  $T=30$  K. Then, the system was warmed up to  $T=45$  K, where we confirmed the disappearance of the XMCD signal. Then, for a second time, we reversed the temperature trend and recorded several more XMCD spectra until reaching  $T=2$  K. Roman numbers in Figure 5.4a, b indicate such measurement order, starting from  $T=60$  K (i) and finishing with  $T=2$  K (viii). Importantly, at 40 K (green line in Figure 5.4a) we start to observe a peak corresponding to the  $L_3$  edge that is not detected at 45 K. This signal grows as the temperature decreases and reaches its maximum at 2 K (the minimum accessible temperature).

Figure 5.4b represents the area enclosed in the XMCD  $L_3$  peaks (from 705 to 712.5 eV) as a function of temperature. Note that we alternatively measured above and below the system's critical temperature, reproducibly detecting a XMCD signal below it, which is indicative of a real phase transition. We use two different models to fit this experimental data: the Onsager exact solution for the 2D Ising model [150] (in orange) and a fitting to a Monte Carlo simulation (in green). The Monte Carlo simulation was calculated for a honeycomb lattice of  $\sim 10.000$  atoms with first neighbor interactions. The best agreement is reached with this calculations, since the Onsager exact solution describes an abrupt decrease of the magnetization at the critical temperature, while the Monte Carlo simulation describes a smooth transition. A reason for this disagreement is that in the Ising model the nodes can adopt only two states (spin up or spin down), while in our experimental case, although presenting a strong out-of-plane anisotropy, they are not purely two-valued.

The second experiment we performed consists in acquiring magnetization curves at normal incidence (ramping the field from 6 T to 0 T) at different temperatures with the intention of constructing an Arrot plot [168]. In essence, we follow the evolution with temperature of the top section of the hysteresis loop (green curve in Fig. 5.3a). The results of these magnetization measurements at normal incidence are presented in Figure 5.4c. Since most of the magnetization curves do not fully saturate at the maximum magnetic field experimentally available (6 T), the Arrot could not be finally constructed. However, the general shape of the magnetic curves with the temperature can still provide some relevant information. Exponential and linear fittings have been added to each magnetization measurement as a guide to the eye. At tem-

peratures  $T \leq 20$  K, such curves have a remnant magnetization showing a clear ferromagnetic behavior. Contrarily, above 60 K these curves approximate to straight lines, as expected for a paramagnet at low field and high temperature. Finally, the curves measured in the range of  $35 \text{ K} \leq T \leq 45 \text{ K}$  present a convex shape without remnant magnetization, that cannot be unambiguously assigned to paramagnetism or ferromagnetism. In conclusion, taking into account both methods we estimate  $T_C = 35 \pm 5$  K in the Fe+DCA/Au(111) system.

Now that we have determined  $T_C$ , the exchange constant ( $J$ ) can be estimated from the analytical Onsager solution as  $J = [T_C k_B \log(\sqrt{3} + 2)]/2$  [150]. In this case (and using  $T_C = 35$  K) it is  $J \approx +1.98$  meV. Finding such value supports the ferromagnetic behavior of the Fe atoms in this system. Indeed, several exchange mechanisms could be responsible of this collective behavior. Direct exchange requires overlapping of the Fe electronic clouds, which is discarded in the 2D-MOF, since Fe atoms are bonded to each other through DCA molecules. An indirect coupling through the substrate electrons (RKKY) could be plausible, however, it does not usually provide such strong interactions [169–172]. For example, a lattice of hexadeca-fluorinated Fe phthalocyanine (FeFPc) and Mn phthalocyanine (MnPc) on Au(111) was reported to present long-range ferrimagnetic interactions directed by RKKY, but the reported exchange constant was  $J=0.12$  meV, which is an order of magnitude lower than ours [172]. Finally, superexchange through organic molecules emerges as the most convincing mechanism to drive the magnetic coupling in our system. Indeed, it has been reported to play a role at different 2D and 3D metal-organic assemblies [40, 159, 173]. Theory is required to confirm such hypothesis, so we are looking into it with our collaborators from CFM (San Sebastian).

The exchange constant found here is quite high when compared with other 2D-MOFs reported presenting ferromagnetic interactions [37, 39, 41, 159]. A similar network where Fe atoms are embedded in molecular N atoms in a three fold symmetry on a Au(111) substrate was studied by Umbach *et al.* [159]. It also resulted in a strongly anisotropic system with an out-of-plane easy magnetization axis. From comparisons between experimental and simulated magnetization curves, they conclude that this system presents superexchange through the organic molecules, resulting in an exchange constant of  $J \approx 80 \mu\text{eV}$ . Similarly, Abdurakhmanova *et al.* obtained superexchange with  $J \approx 0.27$  meV in a network formed with Ni coordination atoms and TCNQ molecules on a Au(111) substrate [41]. Independently of whether the magnetic coupling takes place through organic molecules or the substrate (RKKY) [39], these interactions are several times weaker than the one presented here. Remarkably, we present the first hysteresis loop with such a high coercive field in a 2D-

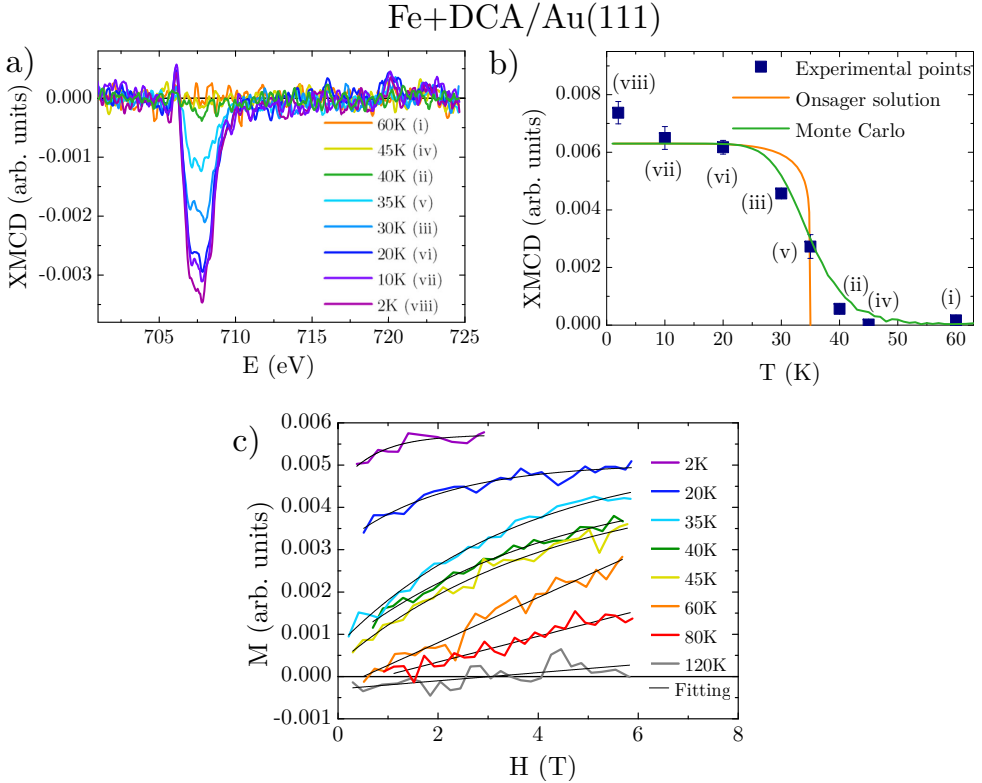


Figure 5.4: Fe+DCA/Au(111) system  $T_C$  calculation. a) XMCD spectra measured at different temperatures with an external field of  $H = 50$  mT. The roman numbers next to each temperature indicate the measurement order. b) Plot of the area enclosed in the XMCD  $L_3$  edge as a function of the temperature from data in panel a. These data is fitted to the Onsager analytical solution (orange) and to a Monte Carlo simulation (green). c) Magnetization curves as a function of sample temperature at normal incidence ramping the field from 6 T to 0 T. Black lines are exponential or straight line fittings used as a guide to the eye.

MOF [36–39, 41, 159]. Thus, although some of the cited networks claim to present ferromagnetic interactions, we present the first indisputable evidence a long-range ferromagnetic order in a 2D-MOF.

Several examples in inorganic 2D magnetism can be found in literature. The first were bulk materials undergoing in-plane interactions much stronger laterally than in the third dimension [174, 175]. More recently, the attention has been focused on van der Waals crystals. Some of them have been reported to present ferromagnetism [176–181], but most of them are not real 2D materials since their unit cell is thicker than a single atom (for example  $\text{Fe}_5\text{GeTe}_2$ ) [179] or they are formed by several weakly interacting 2D layers [181]. As exceptions,  $\text{CrI}_3$  [178] and graphitic  $\text{Zn}_{1-x}\text{Co}_x\text{O}$  [177] do present ferromagnetism in single layers.

In conclusion, we show that Fe+DCA/Au(111) presents ferromagnetism below 35 K. This is the first case of 2D ferromagnetic long-range order in a metal-organic material and constitutes a good experimental approach to the 2D Ising model.

### 5.1.2 The role of the substrate: Fe+DCA/Ag(111)

The same magnetic characterization was carried out for Fe+DCA/Ag(111) to determine the substrate’s influence on the magnetic properties of Fe+DCA network. As shown in Figure 5.5a, the  $L_{2,3}$  edges are visualized in the XAS spectra (which confirms the presence of Fe) on top of the Ag EXAFS. In spite of this, we find in Figure 5.5b that the XMCD signal is practically unnoticeable at the  $L_3$  edge at normal and grazing incidence [it is an order of magnitude smaller than in Fe+DCA/Au(111)]. We find that the grazing dichroic signal is slightly more prominent, which suggests an in-plane anisotropy.

Orbital and spin effective moments obtained with the sum rules are fitted by Eqs. 5.1 and 5.2. The results are presented in Figure 5.6 and summarized in Table 5.2. As deduced from XMCD spectra, orbital moments are quite low with a slight in-plane anisotropy ( $\mu_L^{xy} = 0.18 \mu_B$ ). This is highly reduced when compared with Fe+DCA/Au(111), whose orbital moment at its easy axis is  $\mu_L^z = 1.5 \mu_B$ . Moreover, we find a much lower spin magnetic moment  $\mu_S = 0.61 \mu_B$ .

In essence, we find that the Fe+DCA network magnetism is strongly modified depending if it is formed on Ag(111) or Au(111) substrates. On Au(111) it results in high orbital and spin magnetic moments with a strong out-of-plane anisotropy, presenting ferromagnetic long-range interaction between Fe atoms

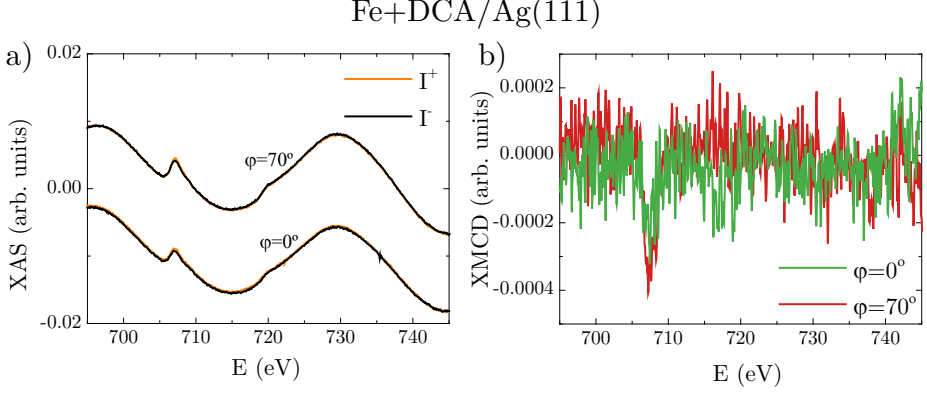


Figure 5.5: XAS and XMCD characterization of Fe+DCA/Ag(111). a) XAS acquired for parallel and antiparallel X-ray alignment with respect to the external magnetic field at normal and grazing incidence at the  $L_{2,3}$  edges of Fe. b) XMCD spectra at both incidences obtained from data in a. The XMCD signal is very weak for both incidences (an order of magnitude smaller than Fig. 5.1a), indicating a very weak Fe magnetic moment.

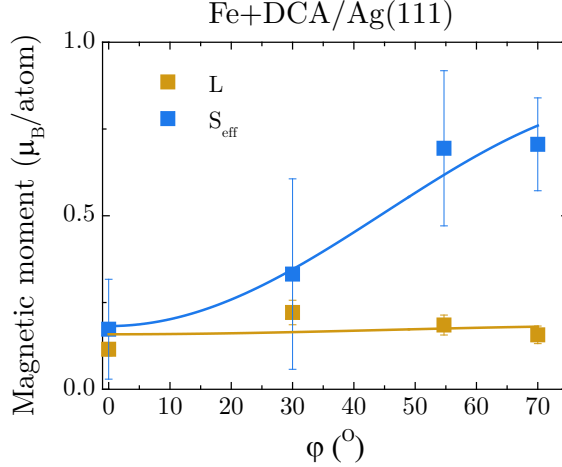


Figure 5.6: Angular dependence of the orbital and spin effective moments of Fe+DCA/Ag(111) obtained by the sum rules. The data are fitted to Eqs. 5.1 and 5.2 and the fitting results are presented in Table 5.2

	$\mu_L^{xy}$ ( $\mu_B$ )	$\mu_L^z$ ( $\mu_B$ )	$\mu_S$ ( $\mu_B$ )	$\mu_T^z$ ( $\mu_B$ )
Fe+DCA/Ag(111)	$0.18 \pm 0.05$	$0.16 \pm 0.04$	$0.61 \pm 0.04$	$0.06 \pm 0.01$

Table 5.2: Orbital and spin magnetic moments of Fe in Fe+DCA/Ag(111) network obtained from fitting the experimental data in Fig. 5.6.

with  $T_C \sim 35$  K. Contrarily, in Fe+DCA/Ag(111) the orbital and spin magnetic moments are strongly reduced and the anisotropy turns out to be very slightly in-plane.

In the previous chapter, we showed that the electronic properties of M+DCA networks are strongly modified by the substrate. Likewise, this applies to the magnetic properties of the networks. One of the possible reasons behind such different behavior could be related to the magnetic screening of surface electrons due to an enhancement of the electronic coupling of Fe with the Ag substrate. This is plausible since despite the stronger interaction with Ag(111), its surface state persists upon covering the substrate with Fe+DCA network. However, one would expect the high magnetic moment observed on Fe+DCA/Au(111) survive at least partially to the Kondo screening, as it is usually the case [182].

Another reason for the vanishing of the magnetic moment on Ag(111) could be the charge transfer from the substrate accompanied by a charge redistribution in Fe 3d orbitals, as reported in other metal-organic 2D systems [182–184]. We believe this option to be the most feasible, since this agrees with the strongly different interaction between M+DCA networks and both substrates [Ag(111) and Au(111)] determined in Chapter 4.

### 5.1.3 Coordination atom dependence: Co+DCA networks

To complement the previous study, the magnetic properties of Co+DCA networks on Au(111) and Ag(111) were investigated. For this, XAS and XMCD spectra were measured at the  $L_{2,3}$  edges of Co. We note however, that the results are inconclusive since we detected a significant beam damage that could very well alter the results presented in this subsection.

The magnetic characterization of Co+DCA/Au(111) is presented in Fig. 5.7. As in the previous cases, Co XAS sits on top of the Au EXAFS. The XMCD spectra line shapes show two main broad peaks from the  $L_{2,3}$  edges, which is characteristic from metallic systems. However, they also present a shoulder at  $\sim 782$  eV, which could be indicative of a slight decoupling of Co from the substrate.  $L_3$  XMCD peak intensity is higher for grazing incidence ( $\varphi = 70^\circ$ ), which suggests an in-plane anisotropy. Finally, magnetization curves measured at normal and grazing incidence angles are shown in Figure 5.7c. Both curves present similar shapes corresponding to a typical paramagnetic behavior, but beam damage altering these results cannot be discarded.

Equivalent measurements and analysis were performed for Co+DCA/Ag(111)

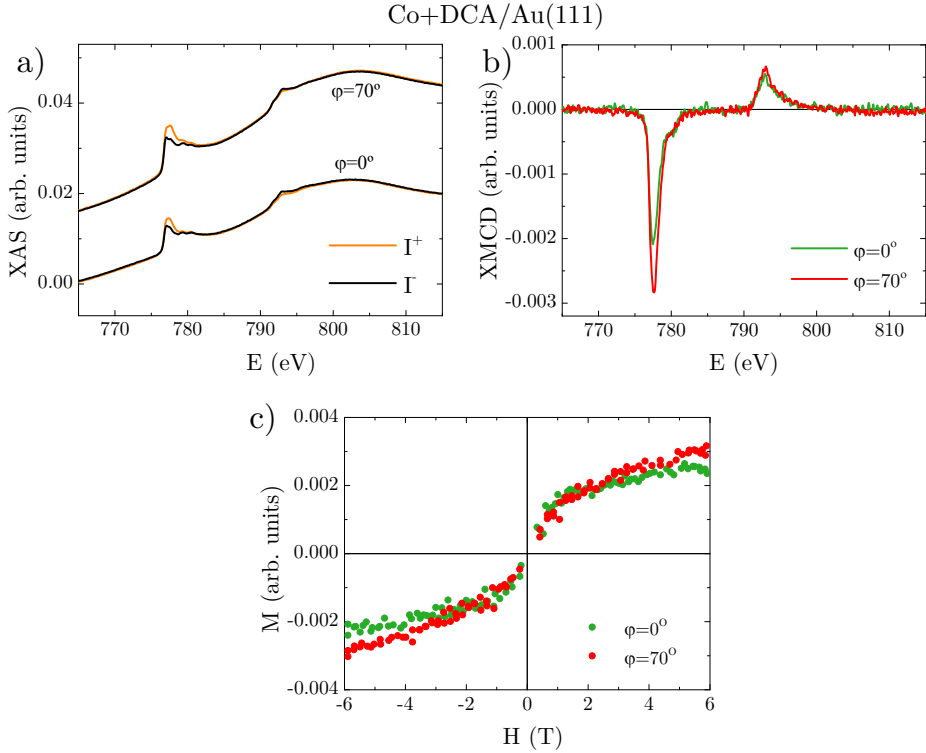


Figure 5.7: XAS and XMCD characterization at the  $L_{2,3}$  edges of Co for the Co+DCA/Au(111) network. We stress that beamdamage may exist in these datasets. a) XAS spectra acquired for parallel and antiparallel X-ray alignment with respect to the external magnetic field at normal and grazing incidence. b) XMCD spectra obtained from data in a) at both incidence angles. c) Magnetization curves acquired in the  $L_3$  edge ramping the magnetic field. Each point plotted corresponds to the average of 10 measured experimental points.



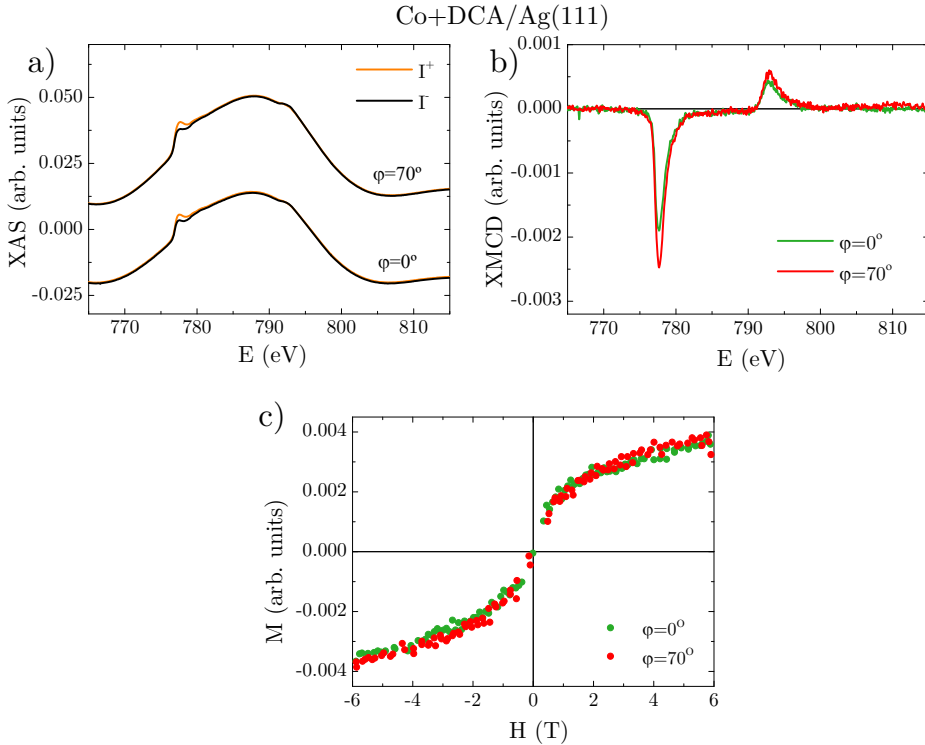


Figure 5.8: XAS and XMCD characterization at the  $L_{2,3}$  edges of Co for the Co+DCA/Ag(111) network. a) XAS spectra obtained for parallel and antiparallel X-ray alignment with respect to the external magnetic field at normal and grazing incidence. b) XMCD spectra obtained from data in a) at both incidence angles. c) Magnetization curves acquired by XMCD in the  $L_3$  edge ramping the magnetic field. Each point plotted corresponds to the average of 10 measured experimental points.

network that are summarized in Figure 5.8. XMCD line shapes are characterized by two featureless peaks corresponding to the  $L_{2,3}$  edges. Unfortunately, we cannot discard that beam damage might have altered again these results. As in the case of Co+DCA/Au(111), the  $L_3$  XMCD peak intensity is higher at grazing incidence, which suggests an in-plane anisotropy. Magnetization curves measured at normal and grazing incidence are similar to each other and their shape is typical from paramagnetic systems. Here, the magnetic signal at 6 T appears with similar intensity at both angles, which differs from the spectra obtained in Figure 5.8b. This difference could be due to molecular beam damage, since the sample is illuminated longer times for magnetization curve measurements than for XMCD spectra.

We derive the orbital and spin effective moments from the sum rules applied

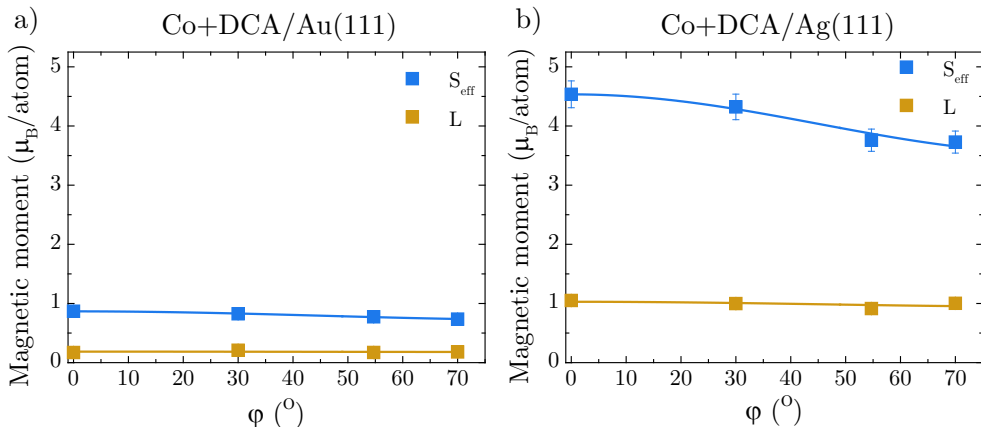


Figure 5.9: Angular dependence of the orbital and spin effective moments of a) Co+DCA/Au(111) and b) Co+DCA/Ag(111) obtained from the sum rules. The data are fitted to Eqs. 5.1 and 5.2 and the fitting results are presented in Table 5.3

to XAS and XMCD measurements performed at 4 different incidence angles ( $\varphi = 0^\circ, 30^\circ, 54.7^\circ, 70^\circ$ ). The obtained data were fitted to Eqs. 5.1 and 5.2, analogously to the Fe case and we show in Figure 5.9 the angular dependent results of the magnetic moments, which are summarized in Table 5.3. Contrarily to the  $L_3$  peak difference in the XMCD spectra, both systems appear quite anisotropic, not showing any preferential direction. Co+DCA/Ag(111) holds a high orbital moment ( $\mu_L^z = 1.03 \mu_B/\text{Co}$ ), that is reduced by a 81 % when the network is formed on Au(111). In the same way, the high spin moment observed in Co+DCA/Ag(111) ( $\mu_S = 3.87 \mu_B/\text{Co}$ ) is sharply reduced on Au(111).

	$\mu_L^{xy} (\mu_B)$	$\mu_L^z (\mu_B)$	$\mu_S (\mu_B)$	$\mu_T^z (\mu_B)$
Co+DCA/Au(111)	$0.18 \pm 0.02$	$0.19 \pm 0.02$	$0.77 \pm 0.08$	$-0.02 \pm 0.01$
Co+DCA/Ag(111)	$0.94 \pm 0.09$	$1.03 \pm 0.10$	$3.87 \pm 0.38$	$-0.09 \pm 0.01$

Table 5.3: Orbital and spin magnetic moments of Co in the indicated assemblies obtained from fitting the experimental data in Figure 5.7 and 5.8.

We stress that during the Co+DCA measurements a relevant beam damage was detected from the very intense X-ray flux on the metal-organic networks. Fortunately, after noticing lack of reproducibility, Fe+DCA systems were measured with a much lower flux rendering reliable and reproducible data. Consequently, we believe that the collective behavior of magnetic cen-

ters in Co+DCA networks, if any, could be lost due to the beam damage on the organic molecules.

In summary, Co+DCA networks present similar magnetic properties when prepared on Au(111) or Ag(111) substrate. Both of them show mainly broad peaks in their XMCD spectra, suggesting a certain hybridization or delocalization of Co  $3d$  electrons. However, the line shape of XMCD spectra on Co+DCA/Au(111) suggests that this system is more decoupled than the one formed on Ag(111). This idea coincides with the lower interaction of M+DCA networks with Au(111) shown in Chapter 4. Magnetization curves performed in both metal-organic structures present similar shapes that are typical from paramagnetic systems, so we infer that the interaction between Co atoms is weak or absent. Nevertheless, these measurements are subject to molecular beam damage, that could alter any existing magnetic collectivity. Finally, the magnetic moments calculated by the sum rules show that the Co+DCA networks are quite isotropic, while their magnetic moments are tailored by the choice of the underlying substrate.

## 5.2 Conclusions

In this chapter we have studied by X-ray techniques the magnetic properties of M+DCA networks coordinated with magnetic atoms (Fe or Co) on different noble metal surfaces [Au(111) and Ag(111)]. Importantly, Fe+DCA/Au(111) network has been demonstrated to be the first metal-organic 2D ferromagnet, with a Curie temperature of  $T_C \sim 35$  K. This, in addition to the strong out-of-plane anisotropy makes this system a very good experimental approach to the Ising model. In contrast, the same network formed on a Ag(111) substrate, the Fe magnetic moment is almost undetected at 6 T, presumably due to charge transfer and charge redistribution effects in the Fe atoms. Finally, although a conclusive result could not be reached due to beam damage, we observed Co+DCA networks to be slightly affected by the substrate. On both substrates, highly isotropic magnetic moments without any signal of collectivity is found.

### 5.3 Supplementary material for Chapter 5

In this section some supplementary figures mentioned along the main text are shown.

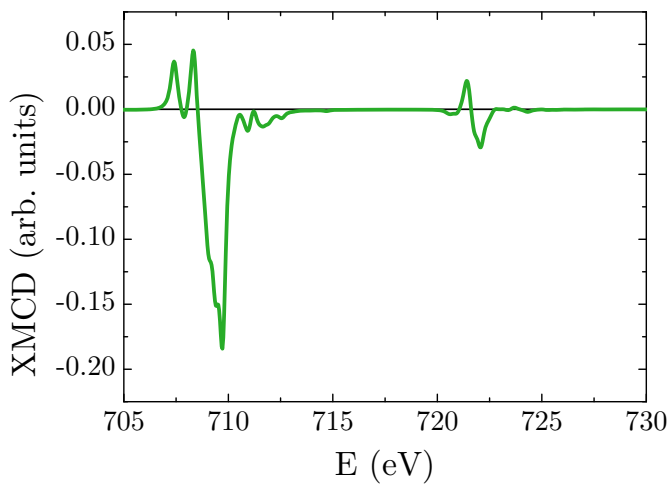


Figure 5.10: Simulated Fe XMCD spectrum obtained by multiplet calculations with the CRISPY software performed at the  $L_{2,3}$  edges of Fe at a  $Fe^{2+}$  ion. Crystal field parameters:  $Dq(3d)=0.013$ ,  $D\sigma(3d)=-0.053$ ,  $D\tau(3d)=-0.13$ .

## Chapter 6

# 2D-MOFs as templates to the growth of metals

The final property we shall study of these metal-organic networks is their use as templates to nanostructure different metals on them, as it has been reported for network components [46], pores [47] or both [48]. In particular, we use Cu+DCA/Cu(111) network as template to nanostructure Sm and Fe. We find that Sm forms a single atom superlattice after its evaporation at RT on the metal-organic network. Interestingly, the revealed superlattice structure and periodicity is directly provided by the underlying molecular phase. However, this formation distorts the underlying network and compromises its integrity, as observed when studying its topography and electronic properties. Such structural deformation is even more evident when evaporating Fe onto the Cu+DCA network. Small nanoclusters are formed that can be tuned in size by varying the Fe coverage and substrate temperature during deposition. This determines their orbital magnetic moment and coercive fields, that we find to increase as the particle size decreases.

## 6.1 Nanostructuring Sm atom arrays on 2D-MOFs

The most stable network we formed is Cu+DCA/Cu(111), judging by its perfect adatom-molecule stoichiometry, its perfect registry with the substrate and the flawless and extended self-assembled arrays. In this way, we use it as template to try to nanostructure a rare earth element, e.g. Sm. After preparing the network as described in Chapter 3, a dilute quantity of Sm atoms is evaporated onto it at RT. Sm atoms are visualized in the STM as bright spots that are identified as single atoms, which are positioned on top of the network, as shown in Figure 6.1. However, they do not lay exactly on the coordination Cu adatoms, but are slightly shifted to a position between the Cu adatom and the molecular cyano group. Interestingly, we find that the Sm atoms preferentially lay on the network or at the island borders, but never on the pristine Cu(111) surface (see Fig. 6.2a).

### Honeycomb superlattices

Knowing that the Sm atoms are attracted onto the coordination adatoms, we tried to form a long-range superstructure. For that, we sequentially added minute quantities of Sm atoms until they covered the Cu adatoms of the network. As a result, a quasi-honeycomb superlattice of Sm is formed, as shown

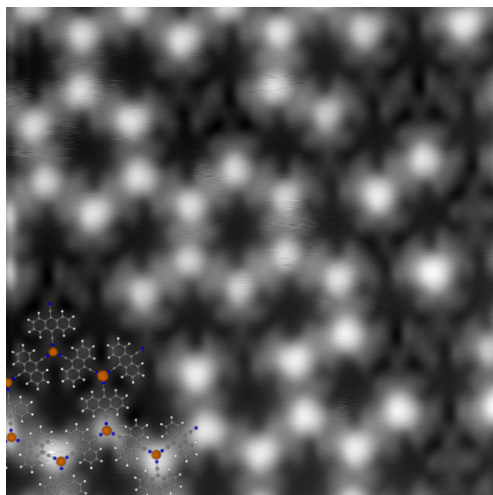


Figure 6.1: A diluted quantity of Sm deposited on Cu+DCA/Cu(111) at RT displays single atom positioning onto the coordination atoms of the network. STM parameters:  $10 \times 10 \text{ nm}^2$ ;  $I_t = 100 \text{ pA}$ / $V_B = -500 \text{ mV}$ .

in Figure 6.2. Hereafter, we will name this structure as  $Sm/(p)$ -DCA and refer to the quantity necessary to cover the 2D-MOF with a single atom superlattice (i.e. 2 Sm atoms per unit cell) as a monolayer of Sm. In Figure 6.2b, c, the same area scanned with opposite  $V_B$  provides a proper visualization of Sm atoms and network alternatively.

The formation of such Sm superlattice was achieved, as shown in Figure 6.2. However, the presence of Sm atoms generates distortions in the underlying network. This comes as a surprise, since the initial Cu+DCA/Cu(111) network is extremely regular and grows in extended domains, as shown in Figure 3.1. Indeed, the symmetry directions are no longer followed, as visualized from the parallel yellow lines depicted in Figure 6.2a, which exhibit an irregular rotation. Moreover, we detect the presence of large cavities within the network domains unobserved in absence of Sm. Therefore, the formation of Sm superlattice can strongly modify the initial periodicity of the underlying network. Nevertheless, a quasi-honeycomb Sm single atom superlattice is formed at the expense of introducing imperfections in the underlying metal-organic network.

Such distortions in the network must necessarily alter the electronic properties of Cu+DCA/Cu(111), especially the *multi-band state*, i.e. the electronic feature coming from extended network bands. In Figure 6.3, the electronic properties of  $Sm/(p)$ -DCA are shown. The  $dI/dV$  spectra are obtained from a large grid measurement performed at a sample region with a submonolayer quantity of Sm atoms (see Fig. 6.3b). In the image, Sm atoms appear brighter than those Cu coordination sites without them. In the legend of Figure 6.3a, the number inside the brackets indicates the number of adjacent Sm atoms linked to each DCA molecule: no neighbouring Sm atoms [DCA (0)], surrounded by 2 Sm atoms [DCA (2)] or by only one [DCA (1)]. The same is indicated for the pores: with no adjacent Sm atoms [pore (0)] or surrounded by 6 of them [pore (6)].

We now compare the spectral features observed with and without adjacent Sm atoms with the bare Cu+DCA/Cu(111) network explored in Chapter 3. First, we no longer detect the network state previously identified at  $-0.55$  V. This is somewhat expected since the loss of periodicity and the local interaction of the Cu and Sm quenches this collective state. Interestingly, at  $0.2$  V we detect the confined surface state, as in the bare network case. However, not all pores confine equally. We find energy dependent intensity differences depending on the number of surrounding Sm atoms (cf. brighter pores in Fig. 6.3e). In particular, there is an energy downshift (of  $\sim 50$  mV) of the *pore state* when surrounded by 6 Sm atoms compared to being surrounded by none.

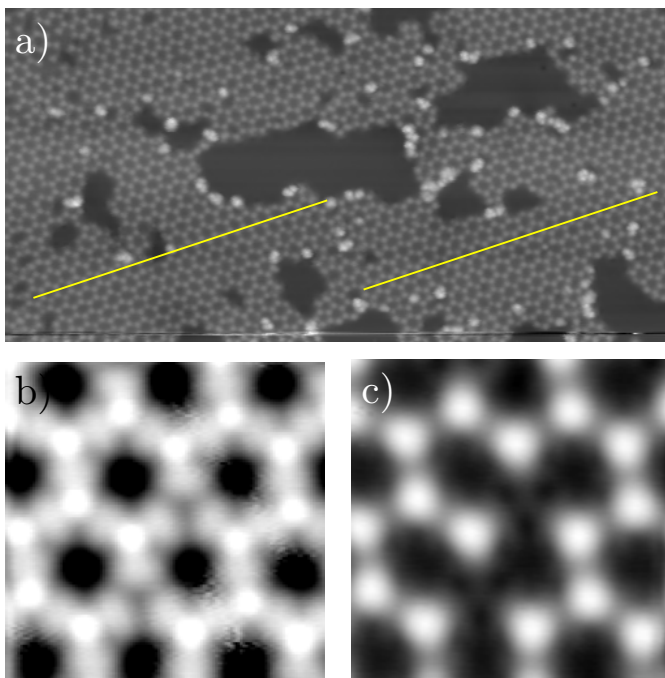


Figure 6.2: Sm hexagonal superlattice of single atoms grown on the Cu+DCA/Cu(111) network. a) Overview of the distorted honeycomb Sm superstructure grown on the Cu+DCA/Cu(111). b), c) Close ups performed at the same area with opposite bias voltages. In b the underlying network is well visualized while in c the Sm superlattice is more evident. The Sm is slightly displaced from the on top of the coordination atom, leading to a slightly irregular honeycomb lattice. STM parameters: a)  $100 \times 50 \text{ nm}^2$ ;  $I_t = 200 \text{ pA}/V_B = -1 \text{ V}$ ; b)  $6 \times 6 \text{ nm}^2$ ;  $I_t = 100 \text{ pA}/V_B = 1 \text{ V}$ ; c)  $6 \times 6 \text{ nm}^2$ ;  $I_t = 100 \text{ pA}/V_B = -1 \text{ V}$ .



Those pores with 6 Sm atoms near them present a downshifted confined surface state, at 0 V (see Fig. 6.3d). This downshift indicates a reduced capacity to confine the Cu(111) surface state upon the presence of Sm atoms. The network distortion and the vertical interaction occurring with the Cu adatoms could be the reason for this subtle confinement reduction. Finally, two strong molecular states are detected at 0.8 V (the *anthracene broad state*) and the onset of another at 1.5 V (the *anthracene slim state*), at similar energies than in the pristine network (see Figure 6.3f, g). Interestingly, the intensity of these molecular states is modulated by the presence of Sm atoms. In the STS spectra presented in Figure 6.3a, the *anthracene broad state* is prominently detected for DCA without Sm atoms (green triangles) that is quenched when the molecule has 2 Sm atoms at its sides (green squares). This effect can be observed in the  $dI/dV$  grid map in Figure 6.3f. A similar behavior is detected at the *anthracene slim state*, that is progressively attenuated with the presence of adjacent Sm atoms, but does not disappear (see Fig. 6.3a, g). We attribute the prominent peak at the Cu adatoms observed at 0.8 V in Figure 6.3a to be a contribution from the molecular states coming from DCA molecules around it, only accessible in absence of any on-top Sm.

### Unraveling new Sm superlattice phases

The spontaneous formation of a Cu+DCA MHK lattice is obtained by evaporation of DCA molecules on a clean Cu(111), as explained in Chapter 3. An excess of DCA molecules (above a porous monolayer coverage) results in the emergence of new, denser, compact network islands in coexistence with the porous one [96]. Figure 6.4a shows such coexistence and the detailed structure of both phases is presented in panels b and c. This new compact phase, that we will name (*c*)-DCA is formed by trimers joined by a Cu atom by one of their cyano groups and leaves no pores. The molecular density of the porous phase is of  $\sim 0.75$  DCA molecules per  $\text{nm}^2$  whereas in the compact phase,  $\sim 1$  per  $\text{nm}^2$ . By the precise tuning of DCA molecules evaporation, a monolayer of compact phase, porous phase or their coexistence can be selectively grown.

Analogously, the evaporation of a dilute quantity of Sm atoms on this compact phase at RT results in the formation of a denser Sm superlattice of independent atoms, when compared to *Sm/(p)-DCA*. In particular, the result of the evaporation of Sm atoms onto the coexistence of both molecular phases is presented in Figure 6.5. The honeycomb superlattice found in *Sm/(p)-DCA* transforms into a denser, squared superstructure of *Sm/(c)-DCA*. The already described network distortions introduced upon Sm vertical adsorption causes

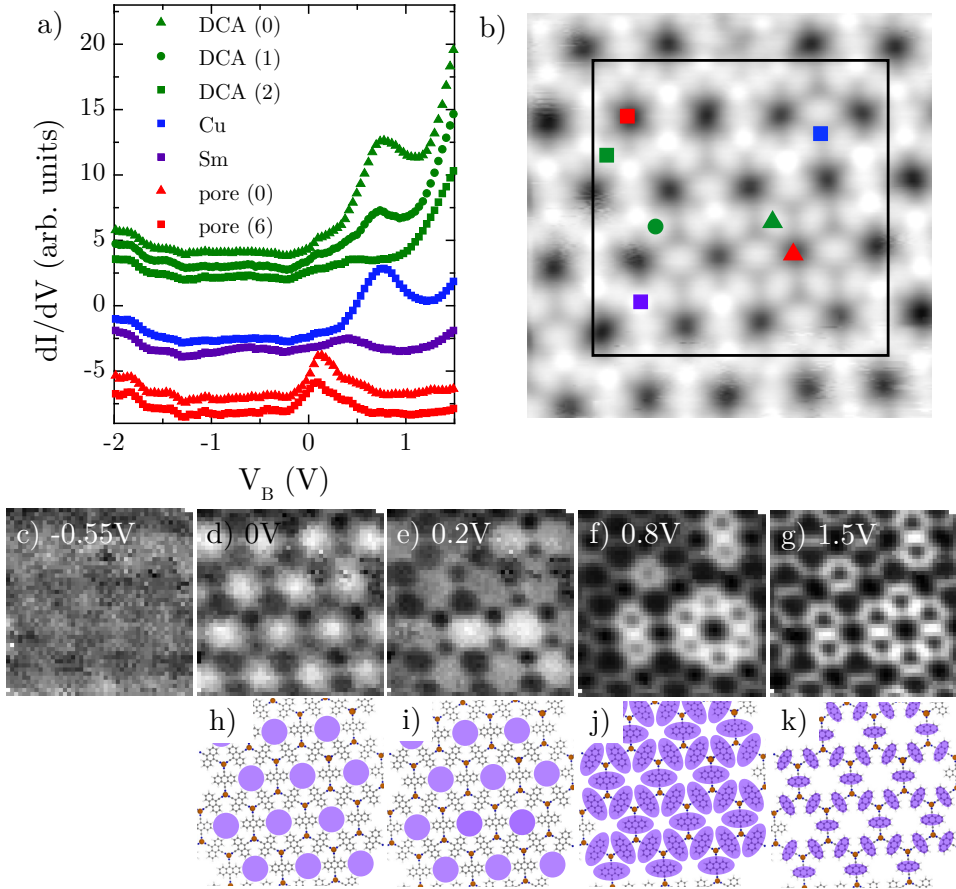


Figure 6.3: Electronic characterization of  $Sm/(p)$ -DCA network. a)  $dI/dV$  spectra at the characteristic points of the network. Numbers inside the brackets in the legend indicate the number of Sm atoms in proximity to each element. b) Close up of the network with Sm atoms that are identified as brighter dots in the Cu adatom positions. Coloured symbols indicate the position of spectra shown in a and the black square indicates the  $dI/dV$  grid measurement area. c)-g)  $dI/dV$  isoenergetic grid maps at the indicated energies. h)-k) Schematics of the states spatial distribution inferred from c-g). STS/STM parameters: a), c)-g) Regulation point:  $I_t = 100 \text{ pA}/V_B = -1V$ ;  $V_{rms} = 9.8 \text{ mV}$ ,  $f_{osc} = 817 \text{ Hz}$ ; b)  $10 \times 10 \text{ nm}^2$ ,  $I_t = 100 \text{ pA}/V_B = 1V$ .

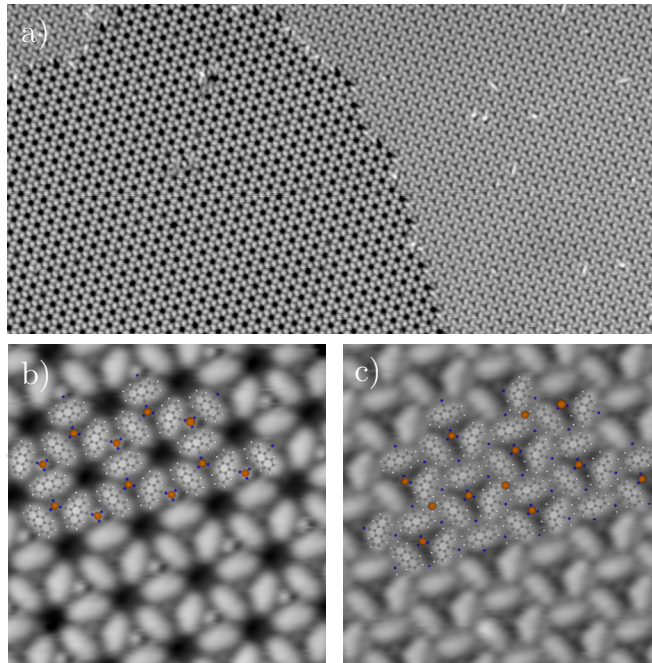


Figure 6.4: Porous [*p*]-DCA] and compact [*c*]-DCA] phases of Cu+DCA/Cu(111) networks. a) Coexisting phases when the coverage slightly exceeds the porous monolayer. b) Porous and c) compact phases with the stick-ball model overlaid. STM parameters: a)  $100 \times 50 \text{ nm}^2$ ,  $I_t = 200 \text{ pA}/V_B = 1 \text{ V}$ ; b)  $8 \times 8 \text{ nm}^2$ ,  $I_t = 100 \text{ pA}/V_B = 1 \text{ V}$ , with a CO-functionalized tip; c)  $8 \times 8 \text{ nm}^2$ ,  $I_t = 100 \text{ pA}/V_B = 1 \text{ V}$ , with a CO-functionalized tip.

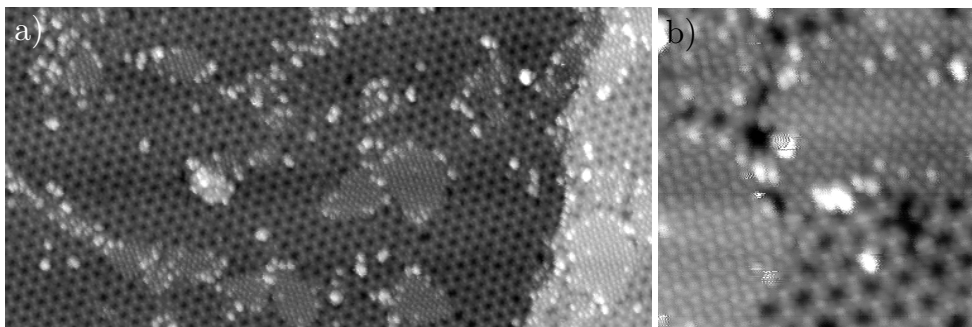


Figure 6.5: Single atom Sm superlattices grown on Cu+DCA/Cu(111) network yielding porous and compact phases. a) Overview of single Sm atom superlattice grown on both phases. On the porous one, a honeycomb superstructure is formed while on the compact phase, the Sm superstructure has a higher density. b) Detail of the Sm superlattice porous and compact phases. STM parameters: a)  $100 \times 50 \text{ nm}^2$ ,  $I_t = 200 \text{ pA}/V_B = -500 \text{ mV}$ ; b)  $20 \times 20 \text{ nm}^2$ ,  $I_t = 200 \text{ pA}/V_B = 500 \text{ mV}$ .

the formation of smaller molecular domains compared to when only molecules are present on the surface (compare Fig 6.4a with Fig 6.5a). Indeed, Sm atoms induce modifications in the underlying metal-organic structure, distorting the network and changing the size of the phase domains.

Other lanthanide 2D superlattices have been grown, mostly on Gr/Ir(111) [185–187] or metallic surfaces [188, 189]. However, our system presents two main advantages: (i) It is generated by simple RT evaporation and, more importantly, Sm atoms are immobilized (even at RT) on the metal-organic network, as observed in the RT-STM images presented in Figure 6.10 in the Supplementary material section. Among the lanthanide superlattices, just Cs/Gr/Ir(111) is generated at RT [187]. (ii) The superlattice structure is tunable to some degree by the molecular coverage, which controls the underlying molecular phase and their relative densities. This is practically impossible when the underlying substrate is a metallic pristine surface or graphene. Indeed, further experiments could be performed with 2D-MOFs as templates with the aim of modifying different lanthanide superlattice interparticle distance, structure, etc.

### X-ray absorption of Sm superlattices

The Sm superlattices are highly interesting from the electronic perspective, so we studied them by X-ray absorption techniques to find the atomic valence in this coordination. Specifically, we measured XAS at the  $M_{4,5}$  edges ( $3d \rightarrow 4f$

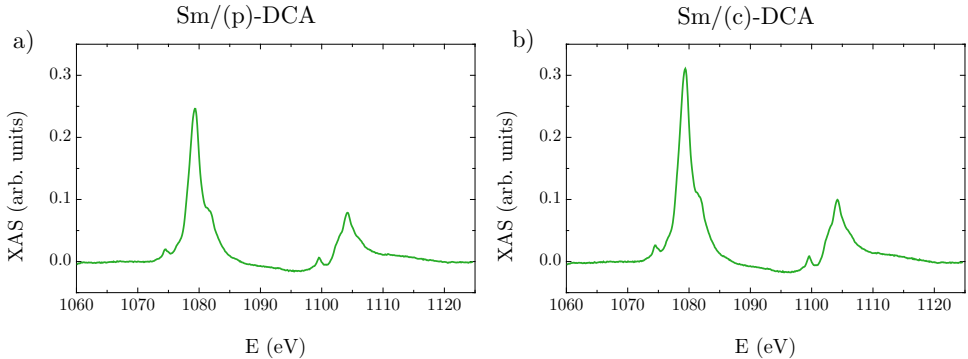


Figure 6.6: XAS at the  $M_{4,5}$  edges of Sm at a)  $Sm/(p)$ -DCA and b)  $Sm/(c)$ -DCA superlattices at normal incidence. Both line shapes correspond to a  $Sm^{3+}$  state.

transitions) of Sm. To do so, a complete monolayer of porous or compact molecular phases were grown, and then a proportional quantity of Sm was evaporated onto it to grow close to a monolayer of  $Sm/(p)$ -DCA or  $Sm/(c)$ -DCA. The evaporation of Sm was carefully calibrated by previous STM topographic measurements to avoid cluster formation and obtain only the signal from single Sm atoms, as shown in Figure 6.10 in the Supplementary material section. These measurements were performed at ID32 in ESRF, Grenoble. The presented spectra were acquired at  $T \sim 7$  K and  $H = 9$  T. Figure 6.6 presents the XAS spectra of both superlattice phases. Both networks present a line shape with a similar multiplet structure, corresponding to  $Sm^{3+}$  [190]. Multiplet calculations of  $Sm^{3+}$  performed with CRISPY software is shown in Figure 6.11 in the Supplementary material section, presenting the same spectral features found experimentally in Figure 6.6. The total intensity is higher in  $Sm/(c)$ -DCA since it contains more absorbing Sm atoms than  $Sm/(p)$ -DCA. Further differences are not expected, since the local chemical environment is practically identical and the Sm atoms are too far away to interact with their nearest in kind. Moreover, in rare earths the inner  $4f$  shell is not involved in the formation of chemical bonds. XAS was measured with circularly polarized light with the intention of obtaining XMCD datasets that would provide information on the magnetic properties of  $Sm/(p)$ -DCA and  $Sm/(c)$ -DCA. However, we find our results controversial so further experiments are necessary to unravel them.

## 6.2 Creating Fe nanoclusters from 2D-MOFs

We further use the templating character of Cu+DCA network to nanostructure Fe intending to either fill the pores or to generate isolated Fe atoms on top of the coordination Cu. Once the molecular layer is completely covering the surface, we evaporate the Fe atoms at a slow rate ( $\sim 0.06$  ML per minute) controlling the temperature of the substrate to finely tune the kinetics of the system. The presence of the network strongly alters the mobility of the Fe atoms on the surface and, instead of the triangular Fe/Cu(111) bilayer islands [191], small nanodots or clusters are observed. Figure 6.7a shows the result of depositing 0.9 ML of Fe onto a clean Cu(111) substrate at RT that covers roughly half of the surface due to double height island formation. Contrarily, depositing the same amount of Fe on a Cu(111) surface completely covers the porous Cu+DCA network, as shown in Figure 6.7b. Interestingly, a defined periodicity is not found for these Fe clusters, which hints at the possibility that the network underneath could be partly destroyed upon Fe deposition. From a close inspection of STM images at much lower Fe coverages (cf. Fig. 6.12), we find that these atoms start nucleating on top of network sites, but avoid clustering within the nanopores. In consequence, the molecular array is structurally affected at the expense of the formation of these clusters. The variation of the substrate temperature upon Fe deposition can additionally alter the kinetics of the system and change the nanoparticle growth. When evaporating identical Fe amounts on a cooled down surface (down to 80 – 120 K) and subsequently letting it warm up to RT, the resulting nanodots turn out to be smaller and more regular in size (see Fig. 6.7c).

The STM images of Figure 6.7 were prepared evaporating the same amount of Fe on the surface (0.9 ML), so the resulting structures can be directly compared. A precise determination of the Fe nanocluster dimensions requires performing particle size and height systematic evaluation. To this end, we apply the grain analysis tools of Gwyddion software [192] to several  $100 \times 100$  nm<sup>2</sup> images of the three studied cases, which yields the particles height and projected area of each. In the following we label the three sets of samples as *Fe/Cu* (upon absence of the network), and *Fe/DCA-(RT)* or *Fe/DCA-(LT)* as indication of the temperature dependent deposition upon the porous phase of the network.

In the particle height analysis, we observe that the nanoclusters grown onto the DCA network preferentially form one atomic height and initiate the formation of the second one only for coverages higher than  $\sim 0.5$  ML, independently of the deposition temperature. This differs from the *Fe/Cu* case, where the

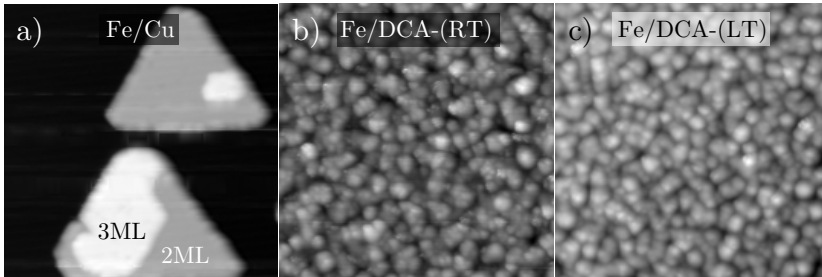


Figure 6.7: Representative STM topographies of different Fe arrangements on the Cu substrate or on the DCA network. a) Triangular Fe islands grown on Cu(111) consisting mostly of two atomic heights. b) Fe nanodots grown on Cu+DCA network at RT. c) Fe nanodots grown on DCA network at  $\sim 100$  K. All the samples have been prepared with 0.9 ML Fe coverage. All image STM parameters:  $35 \times 35$  nm<sup>2</sup>;  $I_t = 50$  pA/ $V_B = 1.5$  V.

islands spontaneously grow in two atomic heights from the very beginning. However, the projected area analysis yields complex results that demand some closer attention. Figure 6.8a shows in different line colours the areal distribution (normalized to one) for the three types of samples shown in Figure 6.7. As already inferred from the topography images, *Fe/Cu* islands (in black) have a very broad area distribution when compared to the nanostructured *Fe/DCA-(RT)* and *Fe/DCA-(LT)* samples. This is visualized as a large spreadout of island sizes exhibiting very low count rates, which implies an undefined average size in comparison to the other two cases. Oppositely, the lines from *Fe/DCA-(RT)* and *Fe/DCA-(LT)* reach the maximum at the smallest areas and rapidly fall to zero indicating a much narrower and smaller size distribution. The drop of the *Fe/DCA-(LT)* (blue line) is much steeper than *Fe/DCA-(RT)* (red line) implying an even smaller size-defined nanostructures. Indeed, Figure 6.8b, c clearly shows this when the histogram resolution is improved and the scale is limited to 20 nm<sup>2</sup> for the *Fe/DCA-(RT)* and *Fe/DCA-(LT)* plots. Their direct comparison reveals a narrower distribution for *Fe/DCA-(LT)*, reflecting that more regular and smaller nanoclusters are generated when cooling the substrate during Fe deposition.

All these experiments and analysis were also performed for lower Fe coverages. Indeed, when depositing half the amount of Fe (0.45 ML), our analysis yields for both LT and RT evaporation smaller particles compared to the previous case (see Table 6.1). A systematic analysis for different Fe coverages clearly shows this effect in the histograms contained in Fig. 6.13 in the Supplementary material section. These results demonstrates that the average particle

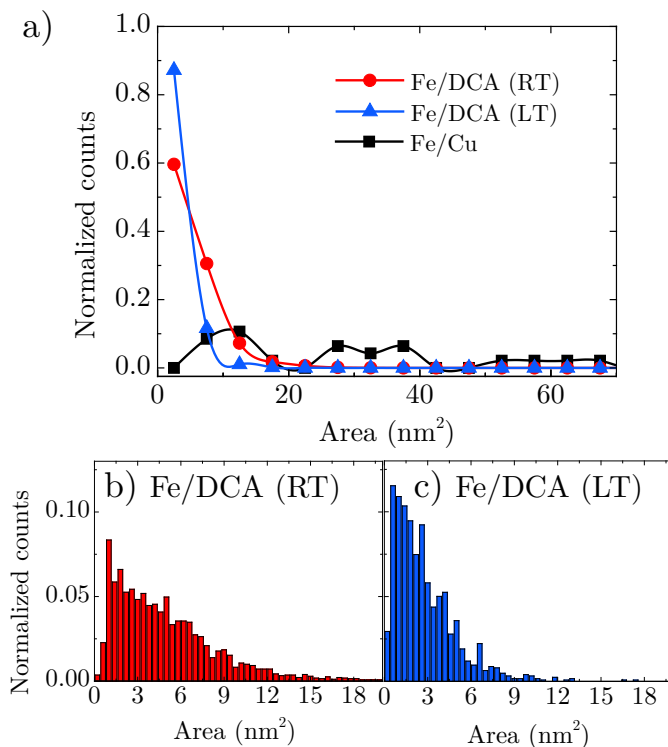


Figure 6.8: Fe nanodots area analysis obtained from 0.9 ML STM images (see Fig. 6.7). a) Compared area distribution for *Fe/Cu* islands (black squares) and *Fe/DCA* nanodots grown both at *RT* (red circles) and *LT* (blue triangles). The intensities are normalized to unity for direct comparison of the three cases. Blow-up and improved resolution for the area histograms of *Fe/DCA*-(*RT*) (b) and *Fe/DCA*-(*LT*) (c), which show that the nanoparticles display a narrower distribution when Fe is deposited at *LT*.



## 6.2. Creating Fe nanoclusters from 2D-MOFs

---

Table 6.1: Average area of Fe nanodots as a function of the substrate deposition temperature and Fe coverage when the network covers completely the surface. These values were obtained by fitting histograms like the ones shown in Figure 6.13 with a Lognormal distribution.

Fe coverage (ML)	Dot area (nm <sup>2</sup> )	
	Fe/DCA-(RT)	Fe/DCA-(LT)
0.45	3.40 ± 0.95	1.78 ± 0.85
0.90	6.23 ± 1.14	2.59 ± 0.98

size can be controlled through the variation of the Fe coverage and substrate temperature.

The presence of the Cu+DCA network layer has a clear nanostructuring effect in the Fe growth. It hinders the diffusion of Fe atoms and prevents large island nucleation, as it happens when the deposition occurs on the pristine Cu(111) surface. The substrate temperature during deposition and the overall coverage allows a certain control over the final nanoparticle size. Indeed, for a particular amount of Fe, the nanodot size can be approximately halved when the deposition is done at LT (see Table 6.1). Notably, once the dots have nucleated we find them to be stable at RT, since their thermal energy turns out to be insufficient to alter their size (See Figure 6.13).

### Magnetic properties of Fe nanodots

The exceptional regularity of the Fe nanodots formed throughout the surface allows us to study their magnetic response using spatial averaging techniques. We have performed XAS and XMCD measurements on the four *Fe/DCA* samples indicated in Table 6.1 and on equivalent preparations without the network presence (*Fe/Cu* islands). From the recorded spectra we find that all these samples (with and without the DCA network) exhibit out-of-plane easy magnetization axis, in agreement with previous work on Fe/Cu(111) [193]. Furthermore, using the magneto-optical sum rules [82, 83], we can extract the third component of orbital and effective spin magnetic moments per atom projected on the quantization axis, i.e.  $\mu_L(\gamma)$  and  $\mu_S^{\text{eff}}(\gamma)$ , where  $\gamma$  is defined as the angle between the surface normal and the incident beam (that coincides with the external magnetization direction). In our analysis we can neglect the in-plane anisotropy. Contrary to Fe stripes on Cu(111), the 2D metal-organic network structures can be considered as isotropic due to their three-fold symmetry, as is also the case for the Fe/DCA islands.

Nanodot average area (nm <sup>2</sup> )	$\mu_L$ ( $\mu_B/atom$ )	$\mu_S^{\text{eff}}$ ( $\mu_B/atom$ )
1.78	$0.159 \pm 0.002$	$1.380 \pm 0.023$
2.59	$0.143 \pm 0.007$	$1.448 \pm 0.008$
3.40	$0.128 \pm 0.001$	$1.387 \pm 0.014$
6.23	$0.128 \pm 0.003$	$1.463 \pm 0.017$

Table 6.2: Magnetic orbital and effective spin moments at normal incidence for different particle sizes, obtained from the XMCD sum rules.

The fits of the magneto-optical sum rules to our data are performed by applying Equations 5.1 and 5.2, analogously to the analysis presented in Chapter 5. These fittings clearly show that (i) the orbital magnetic moments increase significantly and (ii) the anisotropy of both resulting moments become larger whenever the network is present during Fe deposition (for the Fe/DCA cases) compared to the Fe/Cu samples. These datasets can be found in the Supplemental material file, which shows in Figure 6.14 in the Supplementary material section the  $\mu_L(\gamma)$  and  $\mu_S^{\text{eff}}(\gamma)$  plots and corresponding fits for all the measured samples and lists in Table 6.3 the extracted values of the relevant magnetic moments ( $\mu_L^z$ ,  $\mu_L^{xy}$ ,  $\mu_S$ , and  $\mu_T^z$ ).

Notably, we find a clear correlation between the particle size and the orbital magnetic moment (see Table 6.2 for a direct comparison between the values of the magnetic moments obtained at normal incidence with the nanodot average area). This is in good agreement with the expected trend of enhanced orbital moment whenever the particle size diminishes. Such trend relates to the up-scaling of the surface to volume ratio that reduces the average number of neighbors per atom and therefore inhibits the quenching of the orbital magnetic moment [155, 193, 194].

In addition to these measurements, we acquired magnetization loops for normal ( $\varphi = 0^\circ$ ) and grazing ( $\varphi = 70^\circ$ ) beam incidence at otherwise identical sample conditions (see Fig. 6.9). For direct comparison, the experimental magnetization loops are scaled to the magnetic moment per Fe atom using the total magnetic moment obtained from the sum rules at 6 T. The plot of the magnetization curves in Fig. 6.9a for the different systems grown at 0.9 ML evidences that the enclosed area in a cycle increases with decreasing particle size. Moreover, while Fe/Cu systems are practically saturated at normal incidence, the saturation in Fe/DCA samples is not reached at 6 T. We also note that both the orbital magnetic moment and the coercive field are progressively

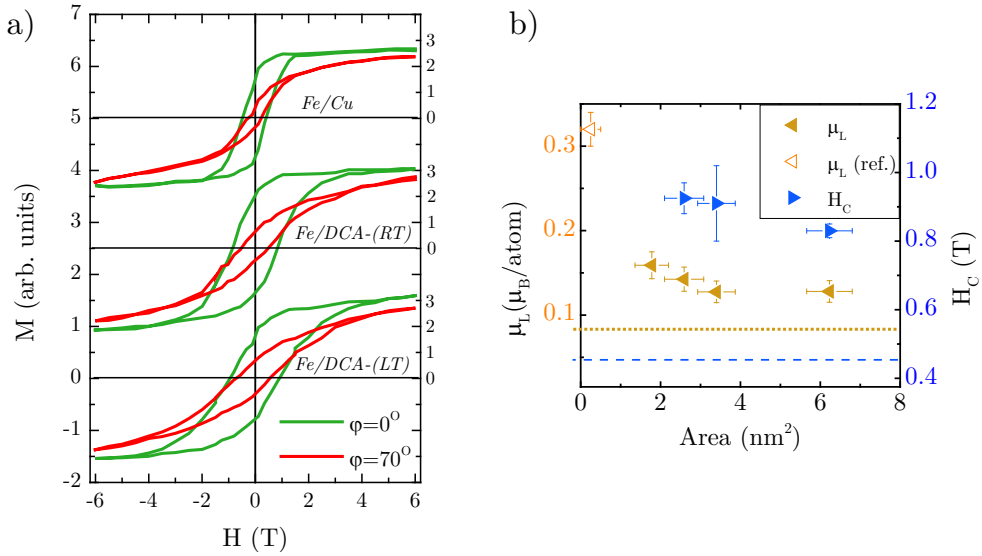


Figure 6.9: Fe nanodots magnetic properties. a) XMCD magnetization loops for the three sample types with 0.9 ML Fe coverage. Constant vertical offsets have been applied for proper data visualization and their corresponding axis partially indicated on the right. b) The magnetic orbital moment ( $\mu_L$ ) and coercive fields ( $H_C$ ) are displayed as a function of the nanodot average area. The dotted and dashed horizontal lines correspond to the  $\mu_L$  and  $H_C$  values obtained from 0.9 ML Fe/Cu(111) islands. The empty triangle at the top left of the graph is a  $\mu_L$  reference corresponding to a  $\sim 3$  Fe atom cluster that was extracted from Ref. [157].

reduced as the particle area increases, approaching slowly towards their bulk values (see Fig. 6.9b).

Such nanostructuring largely affects the magnetic properties of the system since the number of average broken bonds per Fe atom increases [195, 196]. We find that the magnetic orbital moment is enhanced as the average cluster size is reduced, indicating a close relation to the larger surface-to-volume ratio and accordingly the lower chemical saturation [193, 194]. The obtained  $\mu_L$  values are enclosed between the triple atom clusters (the empty triangle in Fig. 6.9) and the Fe/Cu islands (dotted line in Fig. 6.9). Contrarily to this, the spin effective magnetic moment ( $\mu_S^{\text{eff}}$ ) does not appear to be sensitive to the nanodot size changes (see Table 6.2 and Fig. 6.14).

Our Fe nanoparticles display a distinct magnetic anisotropy energy with out-of-plane easy axis, which is estimated not only from the angle dependent magnetic moments, but also from the width defined by the magnetization curves (see Fig. 6.9a). Furthermore, we find higher coercive fields for our nanoparticles compared to the Fe/Cu islands (see Fig. 6.9). This is an expected condition of nanoclusters since surface atoms are known to present higher  $H_C$  than bulk atoms [197–200]. In essence, we find that both  $\mu_L$  and  $H_C$  follow the same tendency with the Fe nanodot average area, i.e. with the relative amount of edge vs bulk atoms.

## 6.3 Conclusions

In conclusion, the spontaneously formed Cu+DCA/Cu(111) network has shown its use to nanostructure Sm and Fe metals. Sm evaporation onto the porous phase generates a superlattice of independent Sm atoms, while Fe evaporation drives to the formation of small nanoclusters ( $1 - 6 \text{ nm}^2$ ) at the expense of distorting the periodicity or destroying the underlying networks. Moreover, the modification of some preparation parameters allows us a certain control over their geometry. The symmetry of Sm superlattices depends directly on the underlying molecular phase, while in the case of Fe, clusters of reduced size are formed whenever evaporated onto the network kept at  $80 - 120 \text{ K}$ . Importantly, all these nanostructures are found to be stable at RT. We demonstrated that Fe clusters present enhanced orbital moment and coercive fields as particle size is decreased. The templating effect of this network could be investigated in depth by varying further preparation parameters or using different metals. This could be specially interesting in the case of rare earths.

## 6.4 Supplementary material for Chapter 6

In this section some supplementary figures mentioned along the main text are shown.

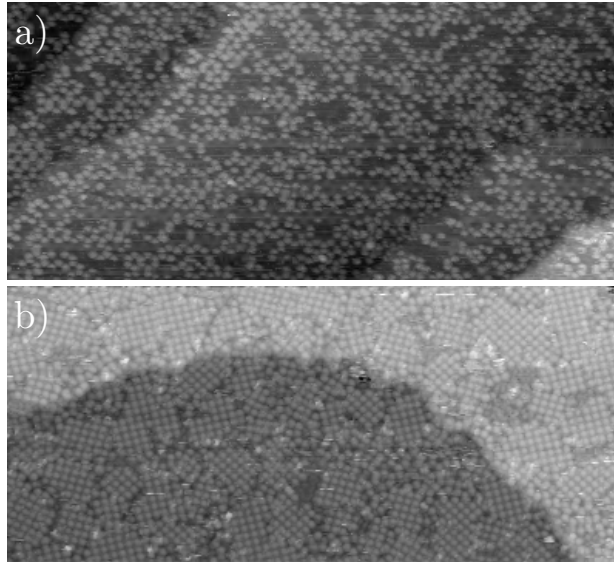


Figure 6.10: RT-STM images acquired *in-situ* just before XAS and XMCD measurements. a) Porous molecular phase with a partial coverage of the honeycomb Sm superlattice [ $Sm/(p)$ -DCA]. b) Compact molecular phase with a multidomain squared Sm superlattice [ $Sm/(c)$ -DCA]. STM parameters:  $100 \times 45 \text{ nm}^2$ , a)  $I_t = 100 \text{ pA/V}_B = 1 \text{ V}$ ; b)  $I_t = 110 \text{ pA/V}_B = -1 \text{ V}$ .

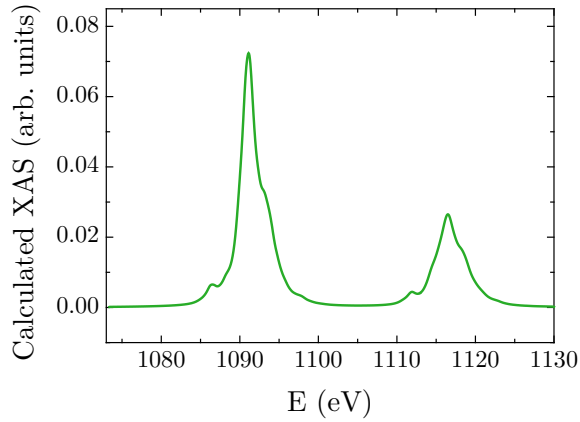


Figure 6.11: Simulated XAS obtained by multiplet calculations performed at the  $M_{4,5}$  edges of Sm at a  $\text{Sm}^{3+}$  ion with CRISPY software. Crystal field parameters:  $B_{40}(4f)=0.01$ ,  $B_{60}(4f)=0.2$ .

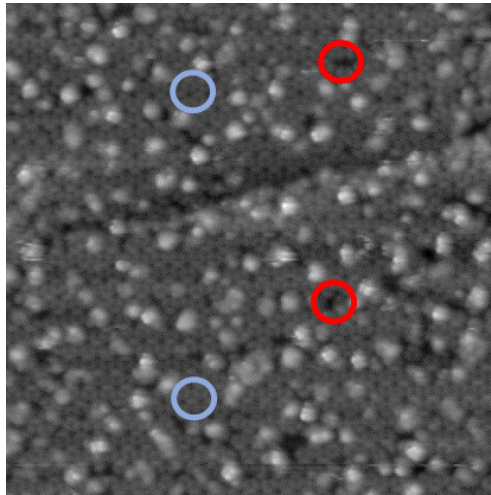


Figure 6.12: RT-STM image of Fe nanodots prepared at RT and in low coverage (0.3 ML). We identify undestroyed (marked in blue) and ruined (marked in red) parts of the network after Fe deposition. Consequently, the Fe nanodots destroy the underlying structure. STM parameters:  $50 \times 50 \text{ nm}^2$ ,  $I_t = 50 \text{ pA/V}_B = 1.5 \text{ V}$ .

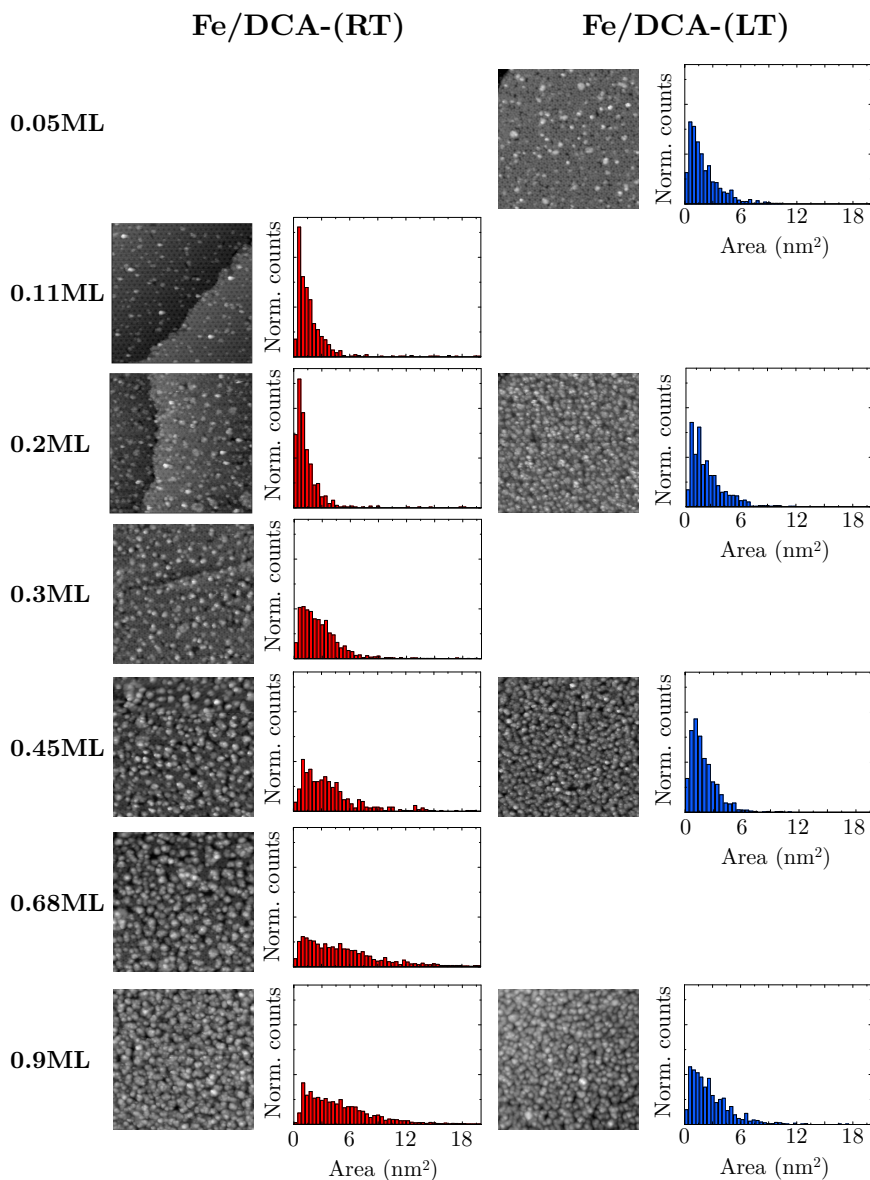


Figure 6.13: Nanodots assemblies as a function of preparation parameters: coverage (each row represents a different coverage) and substrate temperature during deposition (RT on the left column and LT on the second). For each case, a STM image and the dots areas distribution of that sample are presented. We observe that for all the coverages, the effect of depositing Fe at LT makes the nanodots distribution to be narrower and centered in a much smaller area value. All images STM parameters are:  $50 \times 50 \text{ nm}^2$ ,  $I_t = 50 \text{ pA}/V_B = 1.5 \text{ V}$ .



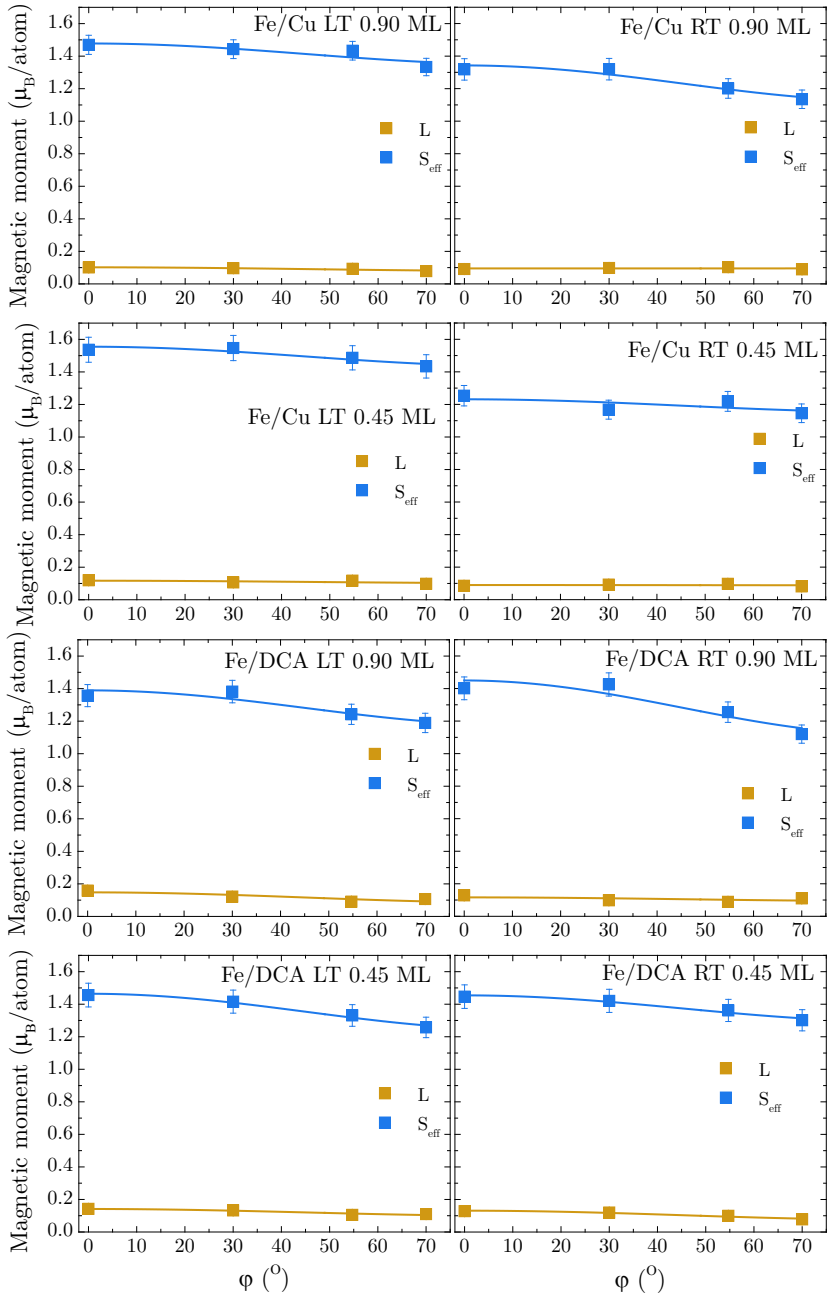


Figure 6.14: Fit of the magnetic moments obtained from application of the sum rules to the experimental XMCD data: orbital magnetic moments (orange) and effective spin (blue). The lines are fits to Eqs. 5.1 and 5.2.

	$\mu_L^{xy} (\mu_B)$	$\mu_L^z (\mu_B)$	$\mu_S (\mu_B)$	$\mu_T^z (\mu_B)$
Fe/Cu-(RT) 0.90 ML	$0.089 \pm 0.001$	$0.094 \pm 0.001$	$1.19 \pm 0.03$	$-0.021 \pm 0.008$
Fe/Cu-(RT) 0.45 ML	$0.081 \pm 0.009$	$0.089 \pm 0.007$	$1.18 \pm 0.04$	$-0.007 \pm 0.010$
Fe/Cu-(LT) 0.90 ML	$0.079 \pm 0.003$	$0.103 \pm 0.003$	$1.39 \pm 0.02$	$-0.012 \pm 0.005$
Fe/Cu-(LT) 0.45 ML	$0.102 \pm 0.009$	$0.117 \pm 0.008$	$1.48 \pm 0.01$	$-0.011 \pm 0.003$
Fe/DCA- (RT) 0.90 ML	$0.105 \pm 0.015$	$0.142 \pm 0.009$	$1.22 \pm 0.04$	$-0.033 \pm 0.010$
Fe/DCA- (RT) 0.45 ML	$0.073 \pm 0.008$	$0.132 \pm 0.010$	$1.35 \pm 0.05$	$-0.015 \pm 0.011$
Fe/DCA- (LT) 0.90 ML	$0.085 \pm 0.010$	$0.142 \pm 0.012$	$1.24 \pm 0.04$	$-0.021 \pm 0.009$
Fe/DCA- (LT) 0.45 ML	$0.099 \pm 0.010$	$0.141 \pm 0.011$	$1.32 \pm 0.08$	$-0.021 \pm 0.018$

Table 6.3: Magnetic moments of Fe/DCA and Fe/Cu systems obtained from the fits shown in Figure 6.14.

## Chapter 7

# Conclusions and Outlook

This thesis focuses on the growth of 2D-MOFs and their electronic and magnetic characterization. 2D-MOFs are composed of organic molecules and coordination atoms, that interact with each other forming strong, but reversible bonds. Such reversibility allows the resulting structures to have a low quantity of defects and long-range order. Different network morphologies can be achieved by an adequate selection of the building components. The coordination atoms can provide the networks with interesting properties for applications, whenever these feature strong SOC or magnetic moments. The network topography and the components interaction do not only between themselves, but also with the underlying substrate, can define extraordinary physical properties of these 2D-MOFs.

Here, 2D-MOFs with 9,10-dicyanoanthracene (DCA) as the only molecular precursor have been grown and characterized. Such molecules have been combined with different coordination atoms (Fe, Co, Cu) and substrates [Cu(111), Ag(111), Au(111), Bi<sub>2</sub>Te<sub>3</sub>] to form different networks with identical morphology. The tailoring of electronic and magnetic properties of such networks by an appropriate choice of the substrate and coordination atoms is shown along this thesis. The main conclusions are summarized in the following lines.

Chapter 3 is centered on Cu+DCA/Cu(111) network, which has a specific theoretical prediction to be an OTI. It is grown forming a long-range ordered, monodomain and almost defect-free network. In spite of this and of detecting the network band, topologically protected edge states were not observed. High-resolution STM images showed slight network distortions, which break mirror and inversion symmetry. Such lack of symmetry produces the closing of the network band gaps and prevents the formation of topologically protected edge

states.

In Chapter 4, seven networks analogous to the one studied in the previous chapter were reported. They are grown by combining different substrates [Au(111), Ag(111), Bi<sub>2</sub>Te<sub>3</sub>] and coordination atoms (Fe, Co, Cu). The electronic properties have been studied with respect to the substrate and coordination atom and their mutual influence. They result to be mainly conditioned by the coupling intensity between the network and the underlying substrate. Networks grown on Ag(111) are slightly more decoupled than on Cu(111), but on Au(111) and Bi<sub>2</sub>Te<sub>3</sub> they are highly decoupled. In all of them, the network band (*multi-band state*), where the edge state could be hosted, has been identified. However, these 1D states are absent in all cases, even when the networks are highly decoupled from their substrates.

Chapter 5 studies the magnetic properties of the networks coordinated with Fe and Co on noble metal surfaces [Au(111) and Ag(111)]. Fe+DCA/Au(111) network results to be a ferromagnet with Curie temperature  $T_C \sim 35$  K and a strong out-of-plane anisotropy. Importantly, this is the first reported case of 2D metal-organic ferromagnets, and also a good experimental approach to the Ising model. Contrarily, the same network formed on Ag(111) presents almost undetectable magnetic moments at  $H=6$  T, probably due to charge transfer and  $3d$  charge redistribution effects. Furthermore, Co+DCA networks present quite isotropic magnetic moments and absence of magnetic collectivity although beam damage could be masking these results.

Finally, in Chapter 6, Cu+DCA/Cu(111) network is used as template for nanostructuring metal adsorbates. The evaporation of diluted quantities of Sm onto it at RT drives to the formation of single Sm atoms superlattices. By previously forming denser molecular phases, denser Sm superlattices are obtained. However, these structures grow in expense of the underlying network integrity, that presents defects and periodicity alterations. The same network was used to nanostructure Fe. In this case, small clusters of  $1 - 6$  nm<sup>2</sup> of projected area are obtained. These sizes can be tuned by two different preparation parameters: substrate temperature and quantity of deposited Fe. This affects their orbital magnetic moment and coercive field, that increase as clusters size decreases. Noteworthy, the nanostructuring of Sm isolated atoms and Fe nanoclusters are stable at RT, so applications could be envisioned.

---

As outlook from this work we can identify several interesting problems that is worth investigating in the future:

- Experimental generation of OTIs. 2D-MHK lattices should be formed with large SOC coordination adatoms (such as Pb or Bi). In these MHK lattices, the minigaps of the *multi-band state* would be large enough to prevent their closure even in the presence of small morphological distortions. If that is achieved, case edge states would emerge.
- Generation of extended 2D-MHK lattices on topological insulators or transition metal dichalcogenides as substrates. These networks have not yet been achieved on these layered materials since molecules tend to easily desorb from these substrates. The expected electronic decoupling that would exist and the intrinsic electronic properties of the substrate could lead to exciting quantum properties.
- Combination of other rare earth atoms on Fe+DCA/Au(111) to generate  $4f$  -  $3d$  orbital superlattices. The combination of these elements could be very interesting in terms of their magnetic response. To date no such systems have been experimentally formed. May be higher Curie temperatures ( $T_C$ ) could be reached upon these atomic mixtures.
- Exploration of MHK-networks on ferromagnetic substrates. Generating these lattices on ferromagnetic substrates such as Ni(111) may lead to interesting magnetic properties on the coordination adatoms.



# Appendix A

## Resumen y conclusiones

Esta tesis está centrada en el crecimiento de redes metal-orgánicas bidimensionales (2D-MOFs) y la caracterización de sus propiedades electrónicas y magnéticas. Las redes metal-orgánicas están formadas por moléculas orgánicas y átomos de coordinación, que interactúan entre sí de manera fuerte pero reversible. Esta reversibilidad permite que las estructuras generadas tengan orden a largo alcance con una cantidad muy pequeña de defectos. A través de una adecuada elección de los componentes se pueden crecer estructuras con distintas morfologías. Una particularidad de las redes metal-orgánicas es que los átomos de coordinación pueden dotarlas de algunas propiedades como, por ejemplo, un alto acople espín-órbita o momentos magnéticos, que son interesantes para aplicaciones. Las diferentes morfologías, la interacción entre los componentes de la red o entre los mismos y el sustrato que los soporta, entre otros, determinan las propiedades físicas (electrónicas, magnéticas y topológicas) de dichos sistemas. El correcto crecimiento y caracterización de las redes metal-orgánicas sin contaminación requiere desarrollar todo el trabajo en condiciones de ultra-alto vacío.

A lo largo de esta tesis se han crecido y caracterizado redes que contienen la molécula 9,10-dicianoantraceno (DCA) como único precursor orgánico. Esta molécula está formada por un antraceno, que facilita su adsorción en la superficie, y dos grupos ciano a los lados, que proporcionan los enlaces con los metales de coordinación. Dichas moléculas se han combinado con distintos metales de coordinación (Fe, Co y Cu) y sustratos [Cu(111), Ag(111), Au(111) y Bi<sub>2</sub>Te<sub>3</sub>] para formar diferentes redes con igual morfología. A lo largo de la tesis se demuestra cómo la red puede variar sus propiedades electrónicas y magnéticas a través de una correcta elección de su átomo de coordinación y sustrato. En

total, la tesis está dividida en 7 capítulos distribuidos como se detalla en los siguientes párrafos.

El Capítulo 1 comienza con una pequeña introducción histórica sobre el microscopio de efecto túnel (STM), principal herramienta de trabajo para esta tesis, así como de los distintos métodos de fabricación utilizados para el crecimiento de nanoestructuras bidimensionales. Además, se presenta el estado del arte de las redes metal-orgánicas bidimensionales centrado en la variedad de morfologías y funcionalidades que se han publicado.

El Capítulo 2 introduce las técnicas experimentales utilizadas a lo largo de esta tesis. En primer lugar se describen los procedimientos de preparación de muestras en condiciones de ultra-alto vacío. A continuación, se presentan las distintas técnicas de caracterización empleadas: difracción de electrones de baja energía (LEED), difracción circular magnético de rayos X (XMCD), espectroscopía de fotoemisión resuelta en ángulo (ARPES) y microscopía de efecto túnel. De esta última se detallan los principios de funcionamiento, así como de otras técnicas relacionadas, como la espectroscopía de efecto túnel (STS) o la obtención de imágenes de alta resolución a través de la funcionalización de puntas con moléculas de CO.

Algunos estudios teóricos predicen que las redes bidimensionales que contienen sub-redes de kagome y de panal de abeja podrían alojar estados de borde topológicamente protegidos. En el Capítulo 3 crecemos la red de Cu+DCA, que cuenta con una predicción teórica específica, sobre un sustrato de Cu(111) y estudiamos sus propiedades electrónicas a través de técnicas mesoscópicas (ARPES) y de sonda local (STS). A pesar de generar una red prácticamente sin defectos con un único dominio, y de detectar la banda de superficie de la red, no se observaron estados de borde. Funcionalizando la punta del STM con una molécula de CO se obtuvieron imágenes de muy alta resolución que permitieron detectar roturas de simetría en la red, que están detrás de la ausencia de dichos estados de borde.

En el Capítulo 4, se presentan siete redes análogas a la estudiada en el anterior capítulo combinando distintos sustratos [Au(111), Ag(111) y Bi<sub>2</sub>Te<sub>3</sub>] y átomos de coordinación (Fe, Co, Cu). Se han estudiado las propiedades electrónicas de la red y la influencia que tiene en ella tanto el átomo de coordinación como la superficie que la soporta. La estructura electrónica de las redes resulta estar condicionada principalmente por la intensidad de la interacción entre la red y el sustrato sobre el que se prepara. Las redes crecidas en Ag(111) están ligeramente más desacopladas que en Cu(111), pero es en Au(111) y Bi<sub>2</sub>Te<sub>3</sub> donde se observa un mayor desacople. En todas ellas se ha



---

identificado la banda de la red en la que deberían alojarse los estados de borde topológicamente protegidos. Sin embargo, no se ha detectado un estado de borde en ningún caso, a pesar de tener algunas de las redes una interacción mínima con el sustrato.

El Capítulo 5 aborda el estudio de las propiedades magnéticas de las redes coordinadas con Fe y Co en sustratos de Ag(111) y Au(111). Una particularidad de estas redes es su similitud con distintos modelos teóricos del magnetismo que han sido muy estudiados, como el modelo de Ising o de Heisenberg. A través de medidas de dicroísmo circular magnético de rayos X se obtiene información de las propiedades magnéticas de un determinado elemento. La red de Fe+DCA formada sobre un sustrato de Au(111) es un ferromagneto con una temperatura crítica  $T_C \sim 35$  K y una fuerte anisotropía con eje fácil fuera del plano, siendo éste el primer caso de ferromagnetismo detectado en muestras metal-orgánicas puramente bidimensionales. Curiosamente, la misma red generada sobre un sustrato de Ag(111) presenta momentos magnéticos casi indetectables a  $H=6$  T, seguramente debido a un efecto de transferencia de carga y redistribución en los orbitales  $3d$  de la misma. Por otro lado, las redes de Co+DCA presentan una menor anisotropía y ausencia de colectividad, aunque los daños por radiación podrían contaminar estos últimos resultados.

Para completar la caracterización, en el Capítulo 6, utilizamos la red de Cu+DCA sobre una superficie de Cu(111) como plantilla para el crecimiento de distintos metales nanoestructurados. Evaporando cantidades muy diluidas de Sm sobre ella a temperatura ambiente se obtiene una superred de átomos sueltos que se posicionan aproximadamente encima de los átomos de coordinación. Hemos observado que generando fases moleculares más densas se obtienen a su vez superredes más densas de átomos sueltos de Sm. Sin embargo, estas superredes crecen a expensas de la integridad de la red subyacente, que presenta defectos y una menor simetría cuando es usada como plantilla. Por otro lado, la misma red se ha utilizado para nanoestructurar Fe. En este caso, se generan pequeños clústers de  $1-6$  nm<sup>2</sup> de área proyectada, cuyo tamaño se puede ajustar modificando dos parámetros de preparación: la temperatura del sustrato y la cantidad de Fe depositada. Esto influye en el momento magnético orbital y en el campo coercitivo de las muestras, que crecen con tamaños decrecientes de los clústers. Es importante destacar que tanto la nanoestructuración del Sm como átomos aislados, así como los clústeres de Fe son estables a temperatura ambiente, lo cual permitiría aplicarlos en dispositivos reales.

La tesis se cierra con el Capítulo 7, donde se exponen las principales conclusiones extraídas durante el desarrollo de este trabajo.



# Bibliography

- [1] G. Binnig et al. “Surface studies by scanning tunneling microscopy”. In: *Physical review letters* 49.1 (1982), p. 57.
- [2] G. Binnig and H. Rohrer. “Scanning tunneling microscopy—from birth to adolescence”. In: *Reviews of modern physics* 59.3 (1987), p. 615.
- [3] G. Binnig et al. “ $7 \times 7$  reconstruction on Si (111) resolved in real space”. In: *Physical review letters* 50.2 (1983), p. 120.
- [4] J. K. Gimzewski, E. Stoll, and R. R. Schlittler. “Scanning tunneling microscopy of individual molecules of copper phthalocyanine adsorbed on polycrystalline silver surfaces”. In: *Surface Science* 181.1-2 (1987), pp. 267–277.
- [5] P. H. Lippel et al. “High-resolution imaging of copper-phthalocyanine by scanning-tunneling microscopy”. In: *Physical review letters* 62.2 (1989), p. 171.
- [6] D. M. Eigler and E. K. Schweizer. “Positioning single atoms with a scanning tunnelling microscope”. In: *Nature* 344.6266 (1990), pp. 524–526.
- [7] M. F. Crommie, C. P. Lutz, and D. M. Eigler. “Confinement of electrons to quantum corrals on a metal surface”. In: *Science* 262.5131 (1993), pp. 218–220.
- [8] G. Binnig, C.F. Quate, and C. Gerber. “Atomic force microscope”. In: *Physical review letters* 56.9 (1986), p. 930.
- [9] Y. Martin and H.K. Wickramasinghe. “Magnetic imaging by “force microscopy” with 1000 Å resolution”. In: *Applied Physics Letters* 50.20 (1987), pp. 1455–1457.
- [10] V. Balzani. “Nanoscience and nanotechnology: The bottom-up construction of molecular devices and machines”. In: *Pure and Applied chemistry* 80.8 (2008), pp. 1631–1650.

- [11] L. Grill et al. “Nano-architectures by covalent assembly of molecular building blocks”. In: *Nature nanotechnology* 2.11 (2007), pp. 687–691.
- [12] Z. Hao et al. “On-surface synthesis of one-type pore single-crystal porous covalent organic frameworks”. In: *Chemical Communications* 55.72 (2019), pp. 10800–10803.
- [13] J. Cai et al. “Atomically precise bottom-up fabrication of graphene nanoribbons”. In: *Nature* 466.7305 (2010), pp. 470–473.
- [14] C. Moreno et al. “Bottom-up synthesis of multifunctional nanoporous graphene”. In: *Science* 360.6385 (2018), pp. 199–203.
- [15] T. Yokoyama et al. “Conformation selective assembly of carboxyphenyl substituted porphyrins on Au (111)”. In: *The Journal of chemical physics* 121.23 (2004), pp. 11993–11997.
- [16] M. Abel et al. “Designing a new two-dimensional molecular layout by hydrogen bonding”. In: *ChemPhysChem* 7.1 (2006), pp. 82–85.
- [17] G. Pawin et al. “A homomolecular porous network at a Cu (111) surface”. In: *Science* 313.5789 (2006), pp. 961–962.
- [18] J. V. Barth, G. Costantini, and K. Kern. “Engineering atomic and molecular nanostructures at surfaces”. In: *Nature* 437.7059 (2005), pp. 671–679.
- [19] J. V. Barth. “Molecular architectonic on metal surfaces”. In: *Annu. Rev. Phys. Chem.* 58 (2007), pp. 375–407.
- [20] L. Dong, Z. A. Gao, and N. Lin. “Self-assembly of metal–organic coordination structures on surfaces”. In: *Progress in Surface Science* 91.3 (2016), pp. 101–135.
- [21] T. Classen et al. “Templated growth of metal–organic coordination chains at surfaces”. In: *Angewandte Chemie International Edition* 44.38 (2005), pp. 6142–6145.
- [22] J. Rodríguez-Fernández et al. “Metal-Coordination Network vs Charge Transfer Complex: The Importance of the Surface”. In: *Journal of Physical Chemistry C* 124.14 (2020), pp. 7922–7929.
- [23] M. A. Lingenfelder et al. “Towards surface-supported supramolecular architectures: tailored coordination assembly of 1, 4-benzenedicarboxylate and Fe on Cu (100)”. In: *Chemistry—A European Journal* 10.8 (2004), pp. 1913–1919.

- [24] D. Ėcija et al. “Five-vertex Archimedean surface tessellation by lanthanide-directed molecular self-assembly”. In: *Proceedings of the National Academy of Sciences* 110.17 (2013), pp. 6678–6681.
- [25] S. O. Parreiras et al. “Tuning the Magnetic Anisotropy of Lanthanides on a Metal Substrate by Metal–Organic Coordination”. In: *Small* (2021), p. 2102753.
- [26] J. I. Urgel et al. “Five-vertex lanthanide coordination on surfaces: a route to sophisticated nanoarchitectures and tessellations”. In: *The Journal of Physical Chemistry C* 118.24 (2014), pp. 12908–12915.
- [27] Y. Song et al. “Self-Assembly and Local Manipulation of Au-Pyridyl Coordination Networks on Metal Surfaces”. In: *ChemPhysChem* 18.15 (2017), pp. 2088–2093.
- [28] J. Li et al. “1,3,5-Benzenetribenzoic Acid on Cu(111) and Graphene/Cu(111): A Comparative STM Study”. In: *Journal of Physical Chemistry C* 120.32 (2016), pp. 18093–18098.
- [29] K. Müller et al. “Cyano-Functionalized Triarylaminines on Coinage Metal Surfaces: Interplay of Intermolecular and Molecule-Substrate Interactions”. In: *Chemistry - A European Journal* 22.2 (2016), pp. 581–589.
- [30] J. Li et al. “Low-Dimensional Metal-Organic Coordination Structures on Graphene”. In: *Journal of Physical Chemistry C* 123.20 (2019), pp. 12730–12735.
- [31] H. Kong et al. “Constitutional Dynamics of Metal–Organic Motifs on a Au(111) Surface”. In: *Angewandte Chemie - International Edition* 55.25 (2016), pp. 7157–7160.
- [32] U. Schlickum et al. “Metal-organic honeycomb nanomeshes with tunable cavity size”. In: *Nano letters* 7.12 (2007), pp. 3813–3817.
- [33] A. Langner et al. “Self-recognition and self-selection in multicomponent supramolecular coordination networks on surfaces”. In: *Proceedings of the National Academy of Sciences* 104.46 (2007), pp. 17927–17930.
- [34] M. Matena et al. “On-surface synthesis of a two-dimensional porous coordination network: Unraveling adsorbate interactions”. In: *Physical Review B - Condensed Matter and Materials Physics* 90.12 (2014), pp. 1–8.
- [35] A. P. Seitsonen et al. “Density functional theory analysis of carboxylate-bridged diiron units in two-dimensional metal-organic grids”. In: *Journal of the American Chemical Society* 128.17 (2006), pp. 5634–5635.

- 
- [36] P. Gambardella et al. “Supramolecular control of the magnetic anisotropy in two-dimensional high-spin Fe arrays at a metal interface”. In: *Nature Materials* 8.3 (2009), pp. 189–193.
- [37] M. Blanco-Rey et al. “Magnetic properties of metal–organic coordination networks based on 3d transition metal atoms”. In: *Molecules* 23.4 (2018), pp. 1–18.
- [38] M. N. Faraggi et al. “Modeling ferro- and antiferromagnetic interactions in metal-organic coordination networks”. In: *Journal of Physical Chemistry C* 119.1 (2015), pp. 547–555.
- [39] L. Giovanelli et al. “Magnetic coupling and single-ion anisotropy in surface-supported mn-based metal-organic networks”. In: *Journal of Physical Chemistry C* 118.22 (2014), pp. 11738–11744.
- [40] D. Wegner et al. “Tuning molecule-mediated spin coupling in bottom-up-fabricated vanadium-tetracyanoethylene nanostructures”. In: *Physical Review Letters* 103.8 (2009), pp. 1–4.
- [41] N. Abdurakhmanova et al. “Superexchange-mediated ferromagnetic coupling in two-dimensional Ni-TCNQ networks on metal surfaces”. In: *Physical Review Letters* 110.2 (2013), pp. 1–5.
- [42] S. Stepanow et al. “Steering molecular organization and host–guest interactions using two-dimensional nanoporous coordination systems”. In: *Nature materials* 3.4 (2004), pp. 229–233.
- [43] D. Kühne et al. “Rotational and constitutional dynamics of caged supramolecules”. In: *Proceedings of the National Academy of Sciences* 107.50 (2010), pp. 21332–21336.
- [44] Q. Zhang et al. “Switching molecular Kondo effect via supramolecular interaction”. In: *ACS nano* 9.12 (2015), pp. 12521–12528.
- [45] G. E. Pacchioni et al. “Two-orbital Kondo screening in a self-assembled metal–organic complex”. In: *ACS nano* 11.3 (2017), pp. 2675–2681.
- [46] R. Decker et al. “Using metal-organic templates to steer the growth of Fe and Co nanoclusters”. In: *Applied Physics Letters* 93.24 (2008), p. 243102.
- [47] R. Zhang et al. “Two-dimensional superlattices of Bi nanoclusters formed on a Au (111) surface using porous supramolecular templates”. In: *ACS nano* 9.8 (2015), pp. 8547–8553.
- [48] M. Pivetta et al. “Formation of Fe cluster superlattice in a metal-organic quantum-box network”. In: *Physical review letters* 110.8 (2013), p. 086102.

- [49] W. Wang et al. “Manipulating localized molecular orbitals by single-atom contacts”. In: *Physical review letters* 105.12 (2010), p. 126801.
- [50] G. V. Nazin, X.H. Qiu, and W. Ho. “Visualization and spectroscopy of a metal-molecule-metal bridge”. In: *Science* 302.5642 (2003), pp. 77–81.
- [51] J. Repp et al. “Imaging bond formation between a gold atom and pentacene on an insulating surface”. In: *Science* 312.5777 (2006), pp. 1196–1199.
- [52] W. Wang et al. “Cooperative modulation of electronic structures of aromatic molecules coupled to multiple metal contacts”. In: *Physical Review Letters* 110.4 (2013), pp. 1–5.
- [53] Z. F. Wang, Z. Liu, and F. Liu. “Organic topological insulators in organometallic lattices”. In: *Nature Communications* 4 (2013), pp. 1–5. URL: <http://dx.doi.org/10.1038/ncomms2451>.
- [54] Z. F. Wang, Ninghai Su, and Feng Liu. “Prediction of a two-dimensional organic topological insulator”. In: *Nano Letters* 13.6 (2013), pp. 2842–2845.
- [55] L. Z. Zhang et al. “Intrinsic Two-Dimensional Organic Topological Insulators in Metal-Dicyanoanthracene Lattices”. In: *Nano Letters* 16.3 (2016), pp. 2072–2075.
- [56] W. Jiang and F. Liu. “Organic Topological Insulators”. In: (2018), pp. 201–224.
- [57] J. Zhang et al. “Prediction of intrinsic two-dimensional non-Dirac topological insulators in triangular metal-organic frameworks”. In: *Applied Physics Letters* 114.4 (2019).
- [58] C. L. Kane and E. J. Mele. “Quantum Spin hall effect in graphene”. In: *Physical Review Letters* 95.22 (2005), pp. 1–4.
- [59] C. L. Kane and E. J. Mele. “Z<sub>2</sub> topological order and the quantum spin hall effect”. In: *Physical Review Letters* 95.14 (2005), pp. 3–6.
- [60] B. A. Bernevig, T. L. Hughes, and S.-C. Zhang. “Quantum Spin Hall Effect and Topological Phase Transition in HgTe Quantum Wells”. In: *Science* 314.5806 (2006), pp. 1757–1761.
- [61] D Hsieh D. Q. et al. “A topological Dirac insulator in a quantum spin Hall phase”. In: *Nature* 452.7190 (2008), pp. 970–974.
- [62] M. Z. Hasan and C. L. Kane. “Colloquium: Topological insulators”. In: *Reviews of Modern Physics* 82.4 (2010), pp. 3045–3067.

- 
- [63] C. Felser and X.-L. Qi. “Topological insulators”. In: *MRS Bulletin* 39.10 (2014), pp. 843–846.
- [64] M. He, H. Sun, and Q.L. He. “Topological insulator: Spintronics and quantum computations”. In: *Frontiers of Physics* 14.4 (2019), p. 43401.
- [65] A. Kumar et al. “Two-Dimensional Band Structure in Honeycomb Metal-Organic Frameworks”. In: *Nano Letters* 18.9 (2018), pp. 5596–5602.
- [66] L. Yan et al. “On-Surface Assembly of Au-Dicyanoanthracene Coordination Structures on Au(111)”. In: *ChemPhysChem* 111 (2019).
- [67] H. Sun et al. “Deconstruction of the Electronic Properties of a Topological Insulator with a Two-Dimensional Noble Metal-Organic Honeycomb-Kagome Band Structure”. In: *Journal of Physical Chemistry C* 122.32 (2018), pp. 18659–18668.
- [68] Z. Gao et al. “Synthesis and characterization of a single-layer conjugated metal-organic structure featuring a non-trivial topological gap”. In: *Nanoscale* 11.3 (2019), pp. 878–881.
- [69] D. Kumar et al. “Manifestation of Strongly Correlated Electrons in a 2D Kagome Metal–Organic Framework”. In: *Advanced Functional Materials* n/a.n/a (), p. 2106474.
- [70] H. M. Guo and M. Franz. “Topological insulator on the kagome lattice”. In: *Physical Review B - Condensed Matter and Materials Physics* 80.11 (2009), pp. 20–23.
- [71] Z. Li et al. “Realization of flat band with possible nontrivial topology in electronic Kagome lattice”. In: *Science Advances* 4.11 (2018), pp. 1–8.
- [72] F. Jona, J. A. Strozier, and W. S. Yang. “Low-energy electron diffraction for surface structure analysis”. In: *Reports on Progress in Physics* 45.5 (1982), p. 527.
- [73] J. Bardeen. “Tunneling from a many-particle point of view”. In: *Physical Review* 131.3 (1963), pp. 1083–1086.
- [74] J. Tersoff and D.R. Hamann. “Theory and application for the scanning tunneling microscope”. In: *Physical review letters* 50.25 (1983), p. 1998.
- [75] J. Tersoff and D.R. Hamann. “Theory of the scanning tunneling microscope”. In: *Physical Review B* 31.2 (1985), p. 805.
- [76] C. J. Chen. *Introduction to scanning tunneling microscopy*. Vol. 4. Oxford University Press on Demand, 1993.



- [77] S. K. Hämäläinen et al. “Intermolecular Contrast in Atomic Force Microscopy Images without Intermolecular Bonds”. In: *Phys. Rev. Lett.* 113 (2014), p. 186102.
- [78] P. Hapala et al. “Origin of high-resolution IETS-STM images of organic molecules with functionalized tips”. In: *Physical Review Letters* 113.22 (2014), pp. 1–5.
- [79] J. Stöhr. *NEXAFS spectroscopy*. Vol. 25. Springer Science & Business Media, 2013.
- [80] G. van der Laan and A. I. Figueroa. In: *Coordination Chemistry Reviews* 277 (2014), pp. 95–129.
- [81] A. Rogalev, K. Ollefs, and F. Wilhelm. “X-ray magnetic circular dichroism”. In: *X-Ray Absorption and X-Ray Emission Spectroscopy: Theory and Applications* (2016), pp. 671–694.
- [82] P. Carra et al. “X-ray circular dichroism and local magnetic fields”. In: *Physical Review Letters* 70.5 (1993), pp. 694–697.
- [83] B. T. Thole et al. “X-ray circular dichroism as a probe of orbital magnetization.” In: *Physical review letters* 68.12 (1992), pp. 1943–1946.
- [84] A. Damascelli. “Probing the electronic structure of complex systems by ARPES”. In: *Physica Scripta T* T109 (2004), pp. 61–74.
- [85] R. Gutzler. “Band-structure engineering in conjugated 2D polymers”. In: *Physical Chemistry Chemical Physics* 18.42 (2016), pp. 29092–29100.
- [86] G. Galeotti et al. “Synthesis of mesoscale ordered two-dimensional  $\pi$ -conjugated polymers with semiconducting properties”. In: *Nature Materials* 19.8 (2020), pp. 874–880.
- [87] M. Ebrahimi and F. Rosei. “Organic analogues of graphene”. In: *Nature* 542.7642 (2017), pp. 423–424.
- [88] R. Gutzler and D. F. Perepichka. “ $\pi$ -Electron conjugation in two dimensions”. In: *Journal of the American Chemical Society* 135.44 (2013), pp. 16585–16594.
- [89] Q. Fan, J. M. Gottfried, and J. Zhu. “Surface-catalyzed C–C covalent coupling strategies toward the synthesis of low-dimensional carbon-based nanostructures”. In: *Accounts of chemical research* 48.8 (2015), pp. 2484–2494.
- [90] W. Liu et al. “A two-dimensional conjugated aromatic polymer via C–C coupling reaction”. In: *Nature chemistry* 9.6 (2017), p. 563.

- 
- [91] M. Ammon, T. Sander, and S. Maier. “On-surface synthesis of porous carbon nanoribbons from polymer chains”. In: *Journal of the American Chemical Society* 139.37 (2017), pp. 12976–12984.
- [92] C. Steiner et al. “Hierarchical on-surface synthesis and electronic structure of carbonyl-functionalized one- and two-dimensional covalent nanoarchitectures”. In: *Nature communications* 8.1 (2017), pp. 1–11.
- [93] S. Clair and D. G. de Oteyza. “Controlling a chemical coupling reaction on a surface: tools and strategies for on-surface synthesis”. In: *Chemical reviews* 119.7 (2019), pp. 4717–4776.
- [94] M. A. Springer et al. “Topological two-dimensional polymers”. In: *Chemical Society Reviews* 49.7 (2020), pp. 2007–2019.
- [95] L. Hernández-López et al. “Searching for kagome multi-bands and edge states in a predicted organic topological insulator”. In: *Nanoscale* 13.10 (2021), pp. 5216–5223.
- [96] G. Pawin et al. “A surface coordination network based on substrate-derived metal adatoms with local charge excess”. In: *Angewandte Chemie - International Edition* 47.44 (2008), pp. 8442–8445.
- [97] J. Zhang et al. “Probing the spatial and momentum distribution of confined surface states in a metal coordination network”. In: *Chemical Communications* 50.82 (2014), pp. 12289–12292.
- [98] J. Lobo-Checa et al. “Band Formation from Coupled Quantum Dots Formed by a Nanoporous Network on a Copper Surface”. In: *Science* 325.5938 (2009), pp. 300–303.
- [99] I. Piquero-Zulaica et al. “Precise engineering of quantum dot array coupling through their barrier widths”. In: *Nat. Commun.* 8 (2017), p. 787.
- [100] I. Piquero-Zulaica et al. “Electron Transmission through Coordinating Atoms Embedded in Metal-Organic Nanoporous Networks”. In: *Phys. Rev. Lett.* 123 (2019), p. 266805.
- [101] I. Piquero-Zulaica et al. “Surface state tunable energy and mass renormalization from homothetic quantum dot arrays”. In: *Nanoscale* 11.48 (2019), pp. 23132–23138.
- [102] M. Wießner et al. “Substrate-mediated band-dispersion of adsorbate molecular states”. In: *Nature communications* 4.1 (2013), pp. 1–6.
- [103] N. Haag et al. “Signatures of an atomic crystal in the band structure of a C<sub>60</sub> thin film”. In: *Physical Review B* 101.16 (2020), p. 165422.

- [104] P. Liljeroth et al. “Single-molecule synthesis and characterization of metal-ligand complexes by low-temperature STM”. In: *Nano Letters* 10.7 (2010), pp. 2475–2479.
- [105] C. Liu et al. “Interaction between adatom-induced localized states and a quasi-two-dimensional electron gas”. In: *Physical Review Letters* 96.3 (2006), pp. 1–4.
- [106] V. Madhavan et al. “Local spectroscopy of a Kondo impurity: Co on Au(111)”. In: *Physical Review B - Condensed Matter and Materials Physics* 64.16 (2001), pp. 1–11.
- [107] F. E. Olsson et al. “Localization of the Cu(111) surface state by single Cu adatoms”. In: *Physical Review Letters* 93.20 (2004), pp. 1–4.
- [108] L. Limot et al. “Surface-state localization at adatoms”. In: *Physical Review Letters* 94.3 (2005), pp. 1–4.
- [109] P. Hapala et al. “Mechanism of high-resolution STM/AFM imaging with functionalized tips”. In: *Phys. Rev. B* 90 (8 2014), p. 085421.
- [110] I. Piquero-Zulaica et al. “Electronic Structure Tunability by Periodic meta-Ligand Spacing in One-Dimensional Organic Semiconductors”. In: *ACS Nano* 12.10 (2018), pp. 10537–10544.
- [111] W. Jiang et al. “Topological band evolution between Lieb and kagome lattices”. In: *Physical Review B* 99.12 (2019), p. 125131.
- [112] H. Hu, Z. Wang, and F. Liu. “Half metal in two-dimensional hexagonal organometallic framework”. In: *Nanoscale Research Letters* 9.1 (2014), pp. 1–5.
- [113] V. Derakhshan and S. A. Ketabi. “Sizable band gap in organometallic topological insulator”. In: *Physica E: Low-Dimensional Systems and Nanostructures* 85 (2017), pp. 253–258.
- [114] F. Crasto De Lima, Gerson J. Ferreira, and R. H. Miwa. “Topological flat band, Dirac fermions and quantum spin Hall phase in 2D Archimedean lattices”. In: *Physical Chemistry Chemical Physics* 21.40 (2019), pp. 22344–22350.
- [115] S. Zhang et al. “Kagome bands disguised in a coloring-triangle lattice”. In: *Physical Review B* 99.10 (2019), p. 100404.
- [116] Y.-Q. Zhang et al. “Synthesizing Highly Regular Single-Layer Alkynyl–Silver Networks at the Micrometer Scale via Gas-Mediated Surface Reaction”. In: *Journal of the American Chemical Society* 141.13 (2019), pp. 5087–5091.

- 
- [117] M. Angeli, E. Tosatti, and M. Fabrizio. “Valley jahn-teller effect in twisted bilayer graphene”. In: *Physical Review X* 9.4 (2019), p. 041010.
- [118] D. Jose and A. Datta. “Structures and Chemical Properties of Silicene: Unlike Graphene”. In: *Accounts of Chemical Research* 47.2 (2013), pp. 593–602.
- [119] A. Rüegg and G. A. Fiete. “Topological insulators from complex orbital order in transition-metal oxides heterostructures”. In: *Phys. Rev. B* 84 (20 2011), p. 201103.
- [120] W. E. Pickett, K.-W. Lee, and R. Pentcheva. “Design of Chern insulating phases in honeycomb lattices”. In: *Physica C: Superconductivity and its Applications* 549 (2018), pp. 99–101.
- [121] M.-Y. Liu et al. “Topological phase transition and tunable electronic properties of hydrogenated bismuthene: from single-layer to double-layer”. In: *Journal of Physics: Condensed Matter* 32.3 (Oct. 2019), p. 035501.
- [122] Y. J. Song et al. “Mapping atomic contact between pentacene and a Au surface using scanning tunneling spectroscopy”. In: *Nano letters* 10.3 (2010), pp. 996–999.
- [123] F. Queck et al. “Bonding Motifs in Metal-Organic Compounds on Surfaces”. In: *Journal of the American Chemical Society* 140.40 (2018), pp. 12884–12889.
- [124] F. Albrecht et al. “Formation and characterization of a molecule-metal-molecule bridge in real space”. In: *Journal of the American Chemical Society* 135.24 (2013), pp. 9200–9203.
- [125] D. Kumar et al. “Electric field control of molecular charge state in a single-component 2d organic nanoarray”. In: *ACS Nano* 13.10 (2019), pp. 11882–11890.
- [126] A. Sabitova, R. Temirov, and F. S. Tautz. “Lateral scattering potential of the PTCDA/Ag (111) interface state”. In: *Physical Review B* 98.20 (2018), p. 205429.
- [127] I. Fernández-Torrente et al. “Gating the charge state of single molecules by local electric fields”. In: *Physical review letters* 108.3 (2012), p. 036801.
- [128] S. Heidorn et al. “Influence of Substrate Surface-Induced Defects on the Interface State between NaCl (100) and Ag (111)”. In: *The Journal of Physical Chemistry C* 117.31 (2013), pp. 16095–16103.

- [129] P. Pervan et al. “Li adsorption versus graphene intercalation on Ir (111): From quenching to restoration of the Ir surface state”. In: *Physical Review B* 92.24 (2015), p. 245415.
- [130] Y. Pennec et al. “Supramolecular gratings for tuneable confinement of electrons on metal surfaces”. In: *Nature nanotechnology* 2.2 (2007), pp. 99–103.
- [131] F. Klappenberger et al. “Tunable quantum dot arrays formed from self-assembled metal-organic networks”. In: *Physical review letters* 106.2 (2011), p. 026802.
- [132] M. Caputo et al. “Manipulating the Topological Interface by Molecular Adsorbates: Adsorption of Co-Phthalocyanine on Bi<sub>2</sub>Se<sub>3</sub>”. In: *Nano Letters* 16.6 (2016), pp. 3409–3414.
- [133] M. G. Cuxart et al. “Molecular Approach for Engineering Interfacial Interactions in Magnetic/Topological Insulator Heterostructures”. In: *ACS Nano* 14 (2020).
- [134] T. Bathon et al. “Systematics of Molecular Self-Assembled Networks at Topological Insulators Surfaces”. In: *Nano Letters* 15.4 (2015), pp. 2442–2447.
- [135] A. D. Pia et al. “TCNQ Physisorption on the Topological Insulator Bi<sub>2</sub>Se<sub>3</sub>”. In: *ChemPhysChem* 19.18 (2018), pp. 2405–2410.
- [136] P. Sessi et al. “Probing the electronic properties of individual MnPc molecules coupled to topological states”. In: *Nano letters* 14.9 (2014), pp. 5092–5096.
- [137] F. Petraki et al. “Electronic structure of FePc and interface properties on Ag (111) and Au (100)”. In: *The Journal of Physical Chemistry C* 116.20 (2012), pp. 11110–11116.
- [138] L. Massimi et al. “Metal-phthalocyanine ordered layers on Au (110): Metal-dependent adsorption energy”. In: *The Journal of chemical physics* 140.24 (2014), p. 244704.
- [139] A. Mugarza et al. “Electronic and magnetic properties of molecule-metal interfaces: Transition-metal phthalocyanines adsorbed on Ag (100)”. In: *Physical Review B* 85.15 (2012), p. 155437.
- [140] P. Gargiani et al. “Spin and orbital configuration of metal phthalocyanine chains assembled on the Au (110) surface”. In: *Physical Review B* 87.16 (2013), p. 165407.

- [141] M. Scardamaglia et al. “Energetics and hierarchical interactions of metal-phthalocyanines adsorbed on graphene/Ir (111)”. In: *Langmuir* 29.33 (2013), pp. 10440–10447.
- [142] S. L. Tait et al. “One-dimensional self-assembled molecular chains on Cu (100): Interplay between surface-assisted coordination chemistry and substrate commensurability”. In: *The Journal of Physical Chemistry C* 111.29 (2007), pp. 10982–10987.
- [143] A. Shchyrba et al. “Controlling the dimensionality of on-surface coordination polymers via endo-or exoligation”. In: *Journal of the American Chemical Society* 136.26 (2014), pp. 9355–9363.
- [144] J. Björk et al. “STM fingerprint of molecule–adatom interactions in a self-assembled metal–organic surface coordination network on Cu (111)”. In: *Physical Chemistry Chemical Physics* 12.31 (2010), pp. 8815–8821.
- [145] F. Bischoff et al. “Tailoring large pores of porphyrin networks on Ag (111) by metal-organic coordination”. In: *Chemistry-A European Journal* 22.43 (2016), pp. 15298–15306.
- [146] M. Matena et al. “Aggregation and Contingent Metal/Surface Reactivity of 1, 3, 8, 10-Tetraazaperopyrene (TAPP) on Cu (111)”. In: *Chemistry-A European Journal* 16.7 (2010), pp. 2079–2091.
- [147] H. Kong et al. “Ni-induced supramolecular structural transformation of cytosine on Au (111): from one-dimensional chains to zero-dimensional clusters”. In: *Chemical Communications* 50.24 (2014), pp. 3242–3244.
- [148] E. Ising. “Beitrag zur theorie des ferromagnetismus”. In: *Zeitschrift für Physik* 31.1 (1925), pp. 253–258.
- [149] S. G. Brush. “History of the Lenz-Ising model”. In: *Reviews of modern physics* 39.4 (1967), p. 883.
- [150] L. Onsager. “Crystal statistics. I. A two-dimensional model with an order-disorder transition”. In: *Physical Review* 65.3-4 (1944), p. 117.
- [151] N. D. Mermin and H. Wagner. “Absence of ferromagnetism or antiferromagnetism in one-or two-dimensional isotropic Heisenberg models”. In: *Physical Review Letters* 17.22 (1966), p. 1133.
- [152] V. L. Berezinskii. “Destruction of long-range order in one-dimensional and two-dimensional systems having a continuous symmetry group I. Classical systems”. In: *Sov. Phys. JETP* 32.3 (1971), pp. 493–500.
- [153] John Michael Kosterlitz and David James Thouless. “Ordering, metastability and phase transitions in two-dimensional systems”. In: *Journal of Physics C: Solid State Physics* 6.7 (1973), p. 1181.

- [154] A. Delga et al. “Electronic properties of Fe clusters on a Au (111) surface”. In: *Physical Review B* 84.3 (2011), p. 035416.
- [155] P. Ohresser et al. “Magnetism of small Fe clusters on Au (111) studied by x-ray magnetic circular dichroism”. In: *Physical Review B* 64.10 (2001), p. 104429.
- [156] C. Boeglin et al. “In-plane magnetocrystalline anisotropy observed on Fe/Cu(111) nanostructures grown on stepped surfaces”. In: *Physical Review B - Condensed Matter and Materials Physics* 66.1 (2002), pp. 144391–144396.
- [157] G. E. Pacchioni et al. “Multiplet features and magnetic properties of Fe on Cu(111): From single atoms to small clusters”. In: *Physical Review B - Condensed Matter and Materials Physics* 91.23 (2015), pp. 1–8.
- [158] P. Gambardella et al. “Localized magnetic states of Fe, Co, and Ni impurities on alkali metal films”. In: *Physical review letters* 88.4 (2002), p. 047202.
- [159] T. R. Umbach et al. “Ferromagnetic coupling of mononuclear Fe centers in a self-assembled metal-organic network on Au(111)”. In: *Physical Review Letters* 109.26 (2012), pp. 1–5.
- [160] J. Bartolomé et al. “Highly unquenched orbital moment in textured Fe-phthalocyanine thin films”. In: *Physical Review B* 81.19 (2010), p. 195405.
- [161] M. Sassi et al. “First-principles Fe L2, 3-edge and O K-edge XANES and XMCD spectra for iron oxides”. In: *The Journal of Physical Chemistry A* 121.40 (2017), pp. 7613–7618.
- [162] M. Retegan. *Crispy: v0.7.3*. 2019.
- [163] M. W. Haverkort, M Zwierzycki, and OK Andersen. “Multiplet ligand-field theory using Wannier orbitals”. In: *Physical Review B* 85.16 (2012), p. 165113.
- [164] D. Weller et al. “Microscopic origin of magnetic anisotropy in Au/Co/Au probed with x-ray magnetic circular dichroism”. In: *Physical Review Letters* 75.20 (1995), p. 3752.
- [165] J. Stöhr and H. König. “Determination of spin-and orbital-moment anisotropies in transition metals by angle-dependent X-ray magnetic circular dichroism”. In: *Physical review letters* 75.20 (1995), p. 3748.
- [166] S.-D. Jiang et al. “An organometallic single-ion magnet”. In: *Journal of the American Chemical Society* 133.13 (2011), pp. 4730–4733.

- [167] Y.-Y. Zhu et al. “An enantiopure Fe III 4 single-molecule magnet”. In: *Chemical Communications* 47.28 (2011), pp. 8049–8051.
- [168] A. Arrott. “Criterion for ferromagnetism from observations of magnetic isotherms”. In: *Physical Review* 108.6 (1957), pp. 1394–1396.
- [169] P. Wahl et al. “Exchange interaction between single magnetic adatoms”. In: *Physical review letters* 98.5 (2007), p. 056601.
- [170] F. Meier et al. “Revealing magnetic interactions from single-atom magnetization curves”. In: *Science* 320.5872 (2008), pp. 82–86.
- [171] L. Zhou et al. “Strength and directionality of surface Ruderman–Kittel–Kasuya–Yosida interaction mapped on the atomic scale”. In: *Nature Physics* 6.3 (2010), pp. 187–191.
- [172] J. Girovsky et al. “Long-range ferrimagnetic order in a two-dimensional supramolecular Kondo lattice”. In: *Nature Communications* 8.May (2017).
- [173] V. Bellini et al. “Propagation of spin information at the supramolecular scale through heteroaromatic linkers”. In: *Physical review letters* 106.22 (2011), p. 227205.
- [174] I. Yamada. “Magnetic Properties of K<sub>2</sub>CuF<sub>4</sub>—A Transparent Two-Dimensional Ferromagnet—”. In: *Journal of the Physical Society of Japan* 33.4 (1972), pp. 979–988.
- [175] A. R. Miedema et al. “Heisenberg Ferromagnetism in Two Dimensions: An Experimental Study”. In: *AIP Conference Proceedings* 18.1 (1974), pp. 806–818.
- [176] C. Gong et al. “Discovery of intrinsic ferromagnetism in two-dimensional van der Waals crystals”. In: *Nature* 546.7657 (2017), pp. 265–269.
- [177] R. Chen et al. “Tunable room-temperature ferromagnetism in Co-doped two-dimensional van der Waals ZnO”. In: *Nature communications* 12.1 (2021), pp. 1–8.
- [178] B. Huang et al. “Layer-dependent ferromagnetism in a van der Waals crystal down to the monolayer limit”. In: *Nature* 546.7657 (2017), pp. 270–273.
- [179] A. F. May et al. “Ferromagnetism near room temperature in the cleavable van der Waals crystal Fe<sub>5</sub>GeTe<sub>2</sub>”. In: *ACS nano* 13.4 (2019), pp. 4436–4442.
- [180] Y. Deng et al. “Gate-tunable room-temperature ferromagnetism in two-dimensional Fe<sub>3</sub>GeTe<sub>2</sub>”. In: *Nature* 563.7729 (2018), pp. 94–99.



- [181] S. Liu et al. “Wafer-scale two-dimensional ferromagnetic Fe<sub>3</sub>GeTe<sub>2</sub> thin films grown by molecular beam epitaxy”. In: *npj 2D Materials and Applications* 1.1 (2017), pp. 1–7.
- [182] S. Stepanow et al. “Mixed-valence behavior and strong correlation effects of metal phthalocyanines adsorbed on metals”. In: *Physical Review B* 83.22 (2011), p. 220401.
- [183] L. M. Arruda et al. “Surface-orientation- And ligand-dependent quenching of the spin magnetic moment of Co porphyrins adsorbed on Cu substrates”. In: *Physical Chemistry Chemical Physics* 22.22 (2020), pp. 12688–12696.
- [184] E. Bartolome et al. “Enhanced Magnetism through Oxygenation of FePc/Ag (110) Monolayer Phases”. In: *The Journal of Physical Chemistry C* 124.25 (2020), pp. 13993–14006.
- [185] M. Pivetta, S. Rusponi, and H. Brune. “Direct capture and electrostatic repulsion in the self-assembly of rare-earth atom superlattices on graphene”. In: *Physical Review B* 98.11 (2018), pp. 1–8.
- [186] R. Baltic et al. “Superlattice of single atom magnets on graphene”. In: *Nano letters* 16.12 (2016), pp. 7610–7615.
- [187] M. Petrović et al. “Moiré-regulated self-assembly of cesium adatoms on epitaxial graphene”. In: *Physical Review B* 96.8 (2017), p. 085428.
- [188] N. N. Negulyaev et al. “Effect of strain relaxations on heteroepitaxial metal-on-metal island nucleation and superlattice formation: Fe on Cu(111)”. In: *Physical Review B - Condensed Matter and Materials Physics* 79.19 (2009), pp. 1–10.
- [189] A. Singha et al. “Magnetic hysteresis in Er trimers on Cu (111)”. In: *Nano letters* 16.6 (2016), pp. 3475–3481.
- [190] B. T. Thole et al. “3d x-ray-absorption lines and the 3d<sup>9</sup> 4f<sup>n</sup>+1 multiplets of the lanthanides”. In: *Physical Review B* 32.8 (1985), p. 5107.
- [191] A. Biedermann et al. “Coexistence of fcc-and bcc-like crystal structures in ultrathin Fe films grown on Cu (111)”. In: *Physical Review B* 73.16 (2006), p. 165418.
- [192] D. Nečas and P. Klapetek. “Gwyddion: An open-source software for SPM data analysis”. In: *Central European Journal of Physics* 10.1 (2012), pp. 181–188.
- [193] P. Ohresser et al. “Magnetism of nanostructures studied by x-ray magnetic circular dichroism: Fe on cu(111)”. In: *Physical Review B - Condensed Matter and Materials Physics* 62.9 (2000), pp. 5803–5809.

- [194] P. Gambardella et al. “Giant magnetic anisotropy of single cobalt atoms and nanoparticles”. In: *Science* 300.5622 (2003), pp. 1130–1133.
- [195] M. M. Bezerra-Neto et al. “Complex magnetic structure of clusters and chains of Ni and Fe on Pt (111)”. In: *Scientific reports* 3.1 (2013), pp. 1–8.
- [196] H. Brune and P. Gambardella. “Magnetism of individual atoms adsorbed on surfaces”. In: *Surface Science* 603.10-12 (2009), pp. 1812–1830.
- [197] X. Batlle and A. Labarta. “Finite-size effects in fine particles: Magnetic and transport properties”. In: *Journal of Physics D: Applied Physics* 35.6 (2002).
- [198] D. A. Dimitrov and G. M. Wysin. “Surface Anisotropy”. In: *Physical Review B* 50.5 (1994), pp. 3077–3084.
- [199] D. A. Dimitrov and G. M. Wysin. “Magnetic properties of spherical fcc clusters with radial surface anisotropy”. In: *Physical Review B* 51.17 (1995), pp. 11947–11950.
- [200] J. Honolka et al. “Magnetism of FePt surface alloys”. In: *Physical review letters* 102.6 (2009), p. 067207.

